LATVIAN JOURNAL of PHYSICS and TECHNICAL SCIENCES

ISSN 0868 - 8257

(Vol. 60)

2023

CONTENTS

LATVIAN JOURNAL of PHYSICS and TECHNICAL SCIENCES

LATVIJAS FIZIKAS un TEHNISKO ZINĀTŅU ŽURNĀLS

ЛАТВИЙСКИЙ ФИЗИКО-ТЕХНИЧЕСКИЙ ЖУРНАЛ

Published six times a year since February 1964
Iznāk sešas reizes gadā kopš 1964. gada februāra
Выходит шесть раз в год с февраля 1964 года

2 (Vol. 60) • 2023

RĪGA

Language Editor: O. Ivanova
Computer Designer: I. Begicevs

INDEXED (PUBLISHED) IN

www.scopus.com
www.sciendo.com
EBSCO (Academic Search Complete, www.epnet.com), INSPEC (www.iee.org.com).
VINITI (www.viniti.ru), Begell House Inc/ (EDC, www.edata-center.com).

Issuers: Institute of Physical Energetics,
Institute of Solid State Physics, University of Latvia
Registration Certificate Number: 000700221

Editorial Contacts:
14 Dzerbenes Street, Riga, LV-1006
LATVIA
tel: +371 26245896
M: +371 29363105
leo@lza.lv

IN MEMORIAM

Skaidrīte Ezerniece

(1931. gada 5.aprīlis -
2023. gada 18.februāris)

Skaidrīte Ezerniece un viņas dvīņu māsa Gaida piedzima 1931.gada 5.aprīlī. Ģimenē jau bija 9 gadus vecākais pusbrālis Alberts un 1932.gada novembrī piedzima jaunākais brālis – Gunārs. Vispirms ģimenes mājvieta bija Maskasvas forštate, pēc tam Pārdaugava un tur arī abas māsiņas devās uz bērnudārzu, bet vasaras pavadīja Jaunmoku pilī. Skaidrīte bija noslēgta un atturīga, reti izrādīja emocijas, abas ar māsu bērnībā pašmācības ceļā bija apguvušas klavierspēli, tāpēc labprāt viesībās sēdās pie klavierēm. Jaunībā abas ar māsu spēlēja volejbolu, peldēja, ziemā slēpoja un vienmēr rūpējās par fizisko formu. Skaidrīte regulāri piedalījās Latvijas skriešanas sporta centra rīkotajās sacensībās, 2018. gadā pat vēl 87 gadu vecumā viņa piedalījās Latvijas Sporta Veterānu Savienības 55. sporta spēlēs, kurās konkurentu viņas vecuma grupā 85+ faktiski nebija.

Skaidrīte mācījās Rīgas 4. vidusskolā un tur arī parādījās viņas interese par eksaktajiem mācību priekšmetiem. 1950. gadā viņa iestājās un sekmīgi pabeidza Latvijas Valsts pedagoģiskā institūta Fizikas un matemātikas fakultāti. Viena no pirmajām Skaidrītes darba vietām bija Slokas vidusskola, kurā viņa strādāja par fizikas skolotāju. Pedagoga darbs turpinājās arī citās skolās.

Tomēr visilgāk Skaidrīte nostrādāja Fizikālās enerģētikas institūtā (no 1963. līdz 2019. gadam). Viņa pildīja institūta izdotā Latvijas fizikas un tehnisko zinātņu žurnāla ("Latvian Journal of Physics and Technical Sciences") atbildīgās sekretāres amatu līdz pat 2019. gada nogalei. Jāpiezīmē, ka šis žurnāls iznāk sešas reizes gadā sākot no 1964. gada februāra. Darbā viņu pieņēma institūta direktors akadēmiķis Kārlis Plaude, vēlāk viņa strādāja žurnāla Galveno redaktoru akadēmiķa Alfona Kroģera un pēc tam akadēmiķa Jura Ekmaņa vadībā. Pa šiem 56 gadiem žurnāls Skaidrītes ikdienas vadībā ir izaudzis un kļuvis par starptautisku zinātnisku žurnālu. Šai laikā divas zinātnieku paaudzes ir strādājušas žurnālā un Skaidrīte Ezerniece ir kļuvusi par leģendu sagatavojot un publicējot šo daudzu pasaules līmeņa pētījumu rezultātus. Paldies viņai par to! Kā leģenda viņa paliks mūsu cieņā pret viņu un atmiņā…

VZI APP Fizikālās enerģētikas institūta kolektīvs

"Latvian Journal of Physics and Technical Sciences" Redakcijas padome

sciendo

LATVIAN JOURNAL OF PHYSICS
AND TECHNICAL SCIENCES
2023, N 2

DOI: 10.2478/lpts-2023-0007

COMPRESSION OF HYDROGEN GAS FOR ENERGY STORAGE: A REVIEW

S. Orlova*, N. Mezeckis, V. P. K. Vasudev

Institute of Physical Energetics,
14 Dzerbenes Str., Riga, LV-1006, LATVIA
*e-mail:sorlova@edi.lv

Hydrogen has gained significant attention in recent years as a clean and sustainable energy source, with the potential to revolutionize the energy industry. However, one of the challenges associated with hydrogen as an energy source is its storage and transportation. Hydrogen is a highly compressible gas, making it difficult to store and transport in its natural state. The study presents different varieties of hydrogen tanks that are used for the storage and transportation of hydrogen gas. The methods for compressing hydrogen are described, with a focus on their advantages and disadvantages. The study concludes by comparing different methods for compressing hydrogen and discussing the factors that influence the choice of method for a specific application. The importance of continued research and development in this area is emphasised, as the efficient compression of hydrogen is crucial for the widespread adoption of hydrogen as a clean and renewable energy source. Life cycle cost analysis can evaluate the economic feasibility of using different hydrogen compressor technologies by estimating the total cost of owning and operating the compressors over their entire lifespan.

Keywords: *Energy storage, high-pressure storage tanks, hydrogen compressors, life cycle cost analysis, refuelling stations.*

1. INTRODUCTION

In recent years, hydrogen has gained significant attention as a potential clean energy source. It can be used as a fuel in fuel cell vehicles and as a source of heat and power in various industrial processes. The production of hydrogen, however, is currently mainly based on fossil fuels, but efforts are being made to develop more sustainable methods, such as using renewable energy sources to produce hydrogen through electrolysis.

According to the International Energy Agency (IEA) [1], the global hydrogen production in 2021 was estimated to be around 70 million metric tons. This is an increase from previous years, reflecting a growing

interest in hydrogen as a clean energy source and the increasing investment in the hydrogen industry. According to various sources, the annual production of green hydrogen in 2021 was estimated to be between 2 to 3 million metric tons. This represents a significant increase from previous years, reflecting the growing interest in green hydrogen as a clean energy source and the increasing investment in the hydrogen industry.

The European Green Deal [2] is a plan by the European Commission to make the EU's economy sustainable by transforming the way Europe produces and consumes energy, reducing its dependence on fossil fuels and combating climate change. The plan includes a commitment to hydrogen as a key enabler of the energy transition and a key part of the EU's effort to decarbonize its economy.

The Green Deal aims at creating a competitive and sustainable hydrogen market in Europe, with a target of at least 40 GW of renewable hydrogen electrolyzers to be installed by 2030. The plan also includes measures to support the development and deployment of hydrogen technologies, such as fuel cells and hydrogen storage, and to remove barriers to the widespread use of hydrogen as a fuel.

Hydrogen compression is used in refuelling stations to provide high-pressure hydrogen for fuel cell vehicles. The compressed hydrogen is stored in high-pressure tanks and dispensed to vehicles through a hydrogen dispenser, similar to a traditional gasoline or diesel pump.

2. HYDROGEN STORAGE

High-pressure hydrogen storage tanks, typically in the range of 350–700 bar, enable a larger amount of hydrogen to be stored in a smaller volume, making it more practical for use in refuelling stations and for vehicle-range requirements. There are many research works [3]–[9] that summarise a series of computational fluid dynamics (CFD) models on the flow field and temperature field during the process of hydrogen charging the high-pressure gaseous hydrogen storage method is widely employed. With high-pressure characteristics of hydrogen storage, rigorous safety precautions are required, such as filling of compressed gas in a hydrogen tank to achieve reliable operational solutions.

Kim et al. [3] analyzed hydrogen filling for a 175-liter tank used in large-sized hydrogen vehicles. Xue et al. [4] used numerical simulation and optimization to study the rapid filling of high-pressure hydrogen storage cylinders. Zhao et al. [5] conducted experimental and numerical research on the temperature evolution during the fast-filling process of a Type III hydrogen tank. Heitsch et al. [6] simulated the fast filling of hydrogen tanks, while Li et al. [7] conducted a review of research on the fast refueling of hydrogen storage systems in fuel cell vehicles. Melideo et al. [8] used CFD simulations to study the filling and emptying of hydrogen tanks, and Gonin et al. [9] conducted a CFD study of the filling of a gaseous hydrogen tank under two contrasted scenarios. High-pressure hydrogen tanks are containers designed to store hydrogen gas at high pressures. There are several types (Fig. 1) of high-pressure hydrogen tanks [10], [11] including:

- Type I: These tanks are made of steel and have a maximum pressure rating of 350 bar. They are commonly used for stationary hydrogen storage.
- Type II: These tanks have a metal liner with a composite overwrap and a

maximum pressure rating of 700 bar. They are lightweight and commonly used for fuel cell vehicles.

- Type III: These tanks have a polymer liner with a composite overwrap and a maximum pressure rating of 700 bar. They are lightweight and commonly used for fuel cell vehicles.
- Type IV: These tanks have a polymer liner with a composite overwrap and a maximum pressure rating of 875 bar. They are the lightest and most expensive type of high-pressure hydrogen tank, and are commonly used for fuel cell vehicles.

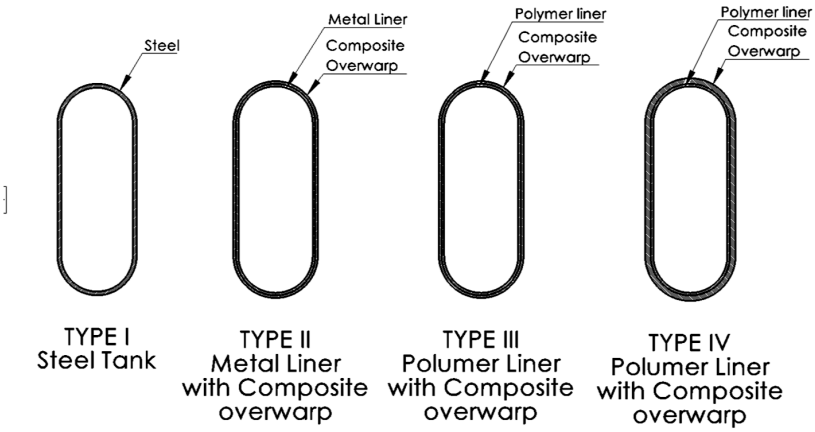

Fig. 1. Types of hydrogen high-pressure tank.

The design and construction of high-pressure hydrogen tanks are critical to ensure safe and reliable hydrogen storage. The tanks must be able to withstand high pressures and mechanical stresses, as well as resist damage from impact, puncture, and corrosion. They must also meet stringent safety standards [12] and undergo rigorous testing and certification before being approved for use. The high-pressure hydrogen tank must ensure safe and reliable operation, which is regulated by government agencies.

There are two main ways to increase the amount of hydrogen (Fig. 2) that can be stored within a given volume: material-based methods and physical methods [13]. Material-based methods involve using other compounds to interact with hydrogen molecules, such as metal hydrides, (e.g., metal hydrides, metal organic frameworks (MOFs)), and nanostructured carbons, hyper-crosslinked polymers (HCPs). Physical methods involve reducing the volume occupied by hydrogen molecules through modifications to temperature and pressure, such as compression of hydrogen gas or cooling the gas to lower temperatures.

Fig. 2. Hydrogen storage approaches.

3. COMPRESSION METHODS

Compression is necessary to store hydrogen in a high-pressure state, as hydrogen has a low energy density and is difficult to store in large quantities without taking up significant space. Hydrogen compression technology is essential for the storage, transportation, and delivery of hydrogen fuel. The purpose of hydrogen compression is to increase the pressure of the hydrogen gas to a level that makes it practical for storage and transportation. There are several international standards that apply to hydrogen compression systems [12], [14], [15].

In terms of hydrogen storage, two compression modes (mechanical and non-mechanical compressors) are generally used to increase volume density. There are several types of mechanical compression methods, including: reciprocating piston compressors, diaphragm compressors, screw compressors, centrifugal compressors (Fig. 3). Mechanical compressors account for more than 50% of the CAPEX (capital expenditure) in a hydrogen refueling station [10]. Non-mechanical compressors are a type of compressor that do not have any moving parts and rely on alternative methods to compress gases. There are several types of non-mechanical compressors (Fig. 3) that can be used specifically for compressing hydrogen gas, including: metal hydride compressors, electromechanical compressors, adsorption compressors and cryogenic compressors.

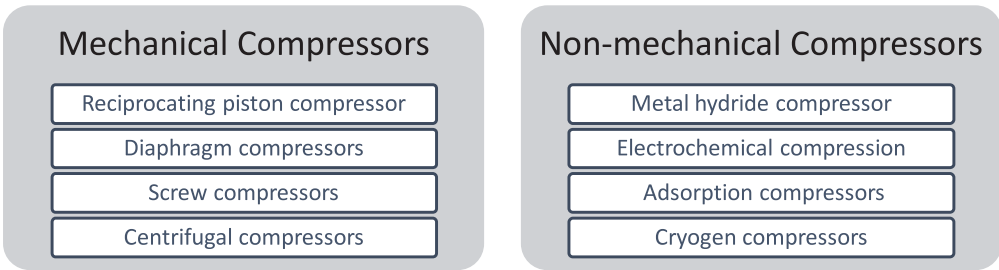

Fig. 3. Hydrogen compression methods.

There are several types of mechanical compression methods, including: reciprocating piston compressors, diaphragm compressors, screw compressors, centrifugal compressors.

Reciprocating piston compressors use a piston to compress hydrogen gas. It is widely used, but can be relatively expensive and less energy-efficient. These compressors work by alternately drawing in and compressing hydrogen gas in a chamber, and then expelling the compressed gas to a storage tank. The process is repeated continuously to increase the pressure of hydrogen gas for storage. A reciprocating piston compressor is presented in different works [16]–[18].

Reciprocating piston compressors consist of several key components, including a cylinder, a piston, a connecting rod, a crankshaft, a drive mechanism, and a control system. The cylinder is the main chamber where hydrogen gas is compressed and stored. The piston moves back and forth in the cylinder to compress and decompress hydrogen gas. The connecting rod connects the piston to the crankshaft, which rotates to provide the back-and-forth motion of the

piston. The drive mechanism, such as an electric motor, provides the power to the crankshaft to compress hydrogen gas. The control system, such as a pressure switch or a timer, regulates the operation of the compressor and ensures that it operates within safe and efficient limits. There are a lot of companies that produce such compressor systems: Siemens Energy, Howden, Neuman & Esser group, Pure Energy Centre.

A hydrogen diaphragm compressor is a type of mechanical compressor designed specifically for compressing hydrogen gas. This type of compressor works by using a flexible diaphragm to separate two chambers, with one chamber holding hydrogen and the other chamber compressing hydrogen. The diaphragm is typically made of a material that is resistant to hydrogen corrosion and permeation, such as stainless steel or PTFE. The diaphragm compressor is popular for compressing hydrogen due to its gas purity and safety features, but it is also prone to frequent diaphragm fractures. Despite the mature leak-detection system, diaphragm failure remains a challenge and must be addressed for reliable operation in hydrogen refuelling stations [19], [20]. This study [21] proposes a non-destructive method for fault diagnosis of diaphragm compressors using acoustic emission signals.

The working process of a diaphragm compressor can be summarised as follows. The compressor draws in hydrogen gas from a storage tank or other source. The flexible diaphragm is moved by a driving mechanism, such as an electric motor, a gas engine, or a hydraulic pump. This motion compresses hydrogen gas on one side of the diaphragm, increasing its pressure. The compressed hydrogen gas is then discharged from the compressor and transported to a storage tank or other location for use. The diaphragm then relaxes and returns to its original position, creating a vacuum that draws in more hydrogen gas for the next compression cycle. This cycle is repeated continuously as long as the compressor is in operation. The number of compression cycles per minute, also known as the compressor frequency, is determined by the speed of the driving mechanism. The amount of hydrogen gas compressed during each cycle depends on the size of the diaphragm and the amount of pressure applied. These companies offer a wide range of compressor systems: Hofer Hochdrucktechnik, PDC machines, Arizona Public Service, Howden, Neuman & Esser group, Hiperbaric, Pure Energy Centre.

Screw compressors are a type of positive displacement compressor that uses two interlocking rotors to compress the gas. The rotors are designed with helical screw threads, which move the gas from the inlet to the outlet of the compressor as they rotate.

The process of compressing hydrogen using a screw compressor is typically as follows: Hydrogen gas is drawn into the inlet of the compressor, where it is mixed with any residual gas from the previous compression cycle. The two interlocking rotors of the compressor, which are designed with helical screw threads, rotate to compress hydrogen gas. As the rotors rotate, hydrogen is moved from the inlet to the outlet of the compressor, where its pressure and density increase. The compressed hydrogen gas is then discharged from the outlet of the compressor and passed through a discharge valve, where any residual gas is separated and released. The compressed hydrogen gas is then cooled, typically using an air-cooled or water-cooled heat exchanger, to remove any heat generated during the compression process. The compressed hydrogen gas is then stored in a high-pressure storage vessel, where it can be used as a fuel or as a feedstock for chemical processes [22]. There are several companies that produce

hydrogen compressor systems for various industrial and automotive applications: Howden, Adicomp, Aerzen.

Centrifugal compressors are a type of dynamic compressor that use the kinetic energy of a rapidly rotating impeller to compress gas. They work by drawing gas into the centre of the impeller, where it is accelerated by the spinning blades. The gas is then discharged radially from the impeller into a diffuser, where its velocity is converted into pressure. Hydrogen gas is drawn into the inlet of the compressor, where it enters the impeller. The impeller, which is designed with spinning blades, rapidly rotates to accelerate the hydrogen gas. The gas is then discharged radially from the impeller into a diffuser, where its velocity is converted into pressure. This process results in an increase in the pressure and density of hydrogen gas.

The compressed hydrogen gas is then discharged from the diffuser and passed through a discharge valve, where any residual gas is separated and released. The compressed hydrogen gas is then cooled, typically using an air-cooled or water-cooled heat exchanger, to remove any heat generated during the compression process. The compressed hydrogen gas is then stored in a high-pressure storage vessel, where it can be used as a fuel or as a feedstock for chemical processes [23], [24]. Siemens Energy, Howden, Baker Hughes are companies that produce such compressor systems. The performance data are presented in Table 1.

Table 1. Comparison of Performance Data of Mechanical Compressors

Key factors	**Performance**
Efficiency	Centrifugal compressors are typically the most efficient type of compressor, followed by screw compressors, diaphragm compressors, and reciprocating compressors.
Flow rate	Screw compressors and centrifugal compressors are typically capable of delivering higher flow rates than diaphragm compressors and reciprocating compressors. This makes them better suited for applications that require large volumes of compressed gas.
Pressure capability	Reciprocating compressors are capable of delivering high pressure levels, making them well-suited for applications that require high pressure gas. Screw compressors and centrifugal compressors are also capable of delivering high pressure levels, although they may be less capable than reciprocating compressors. Diaphragm compressors are typically limited to lower pressure levels.
Maintenance	Reciprocating compressors typically require regular maintenance to ensure proper operation, including regular oil changes, regular cleaning of the filter elements, and periodic inspection of the pistons and other components. Screw compressors and centrifugal compressors may require less maintenance, although they may still require regular checks to ensure proper operation and to detect potential problems. Diaphragm compressors typically require less maintenance than other types of compressors, as they are relatively simple in design and typically have few moving parts.
Cost	The cost of each type of compressor can vary significantly, depending on factors such as the size and complexity of the design, as well as the materials and components used. Reciprocating compressors and diaphragm compressors are typically the least expensive, while screw compressors and centrifugal compressors can be more expensive.

It should be noted that these are generalisations, and the performance of individual compressors can vary widely based on the specific design and operating conditions. Before selecting a compressor, it is important to consider the specific requirements of the application and to compare the performance data of several different compressors to determine the best fit.

Metal hydride compressor uses a method of compressing hydrogen through a chemical reaction with a metal hydride material. This

method works by absorbing hydrogen gas into the metal hydride, causing the material to change its structure and store hydrogen in a solid state. When hydrogen is needed, it can be released from the metal hydride by heating the material, causing it to return to its gaseous form. This process allows hydrogen to be stored and transported at high pressures, making it more practical and efficient.

Metal hydrides are often made of intermetallic compounds or complex metal alloys that have the ability to absorb hydrogen gas. The choice of metal hydride material is important as it affects the hydrogen storage capacity, release kinetics, and overall efficiency of the system [18], [25]–[28].

The performance of a hydrogen compressor based on metal hydride technology is being investigated through experimental methods by changing the operational factors, such as the temperature of the heat source and the pressure of the hydrogen supply in those works [29], [30]. In some research works hydrogen storage power supply system was proposed and examined from economic, environmental and social perspectives [27]. Metal hydride compressor producers are CYRUS, Hystorsys, Ergenics Corp.

Adsorption compressors use the process of compressing hydrogen gas by adsorbing it onto the surface of a solid material. This process can be used to increase the pressure of hydrogen, making it easier to store and transport.

There are several types of solid materials that can be used for hydrogen adsorption compression, including porous materials, such as activated carbon and zeolites, and solid-state metal hydrides. These materials can adsorb large amounts of hydrogen gas, allowing for high-pressure storage in a relatively small volume.

The working of hydrogen adsorption compression can be described as follows: Hydrogen gas is fed into the adsorption compression system, which is typically composed of a high-pressure vessel containing the solid adsorbent material. The hydrogen gas molecules are adsorbed onto the surface of the solid adsorbent material, which causes the pressure of the gas to increase. Hydrogen gas can be stored at high pressures within the adsorbent material, which allows for efficient storage and transport of the gas. When hydrogen is needed, it can be released from the adsorbent material by reducing the pressure or changing the temperature of the system. This causes hydrogen molecules to desorb from the surface of the adsorbent material and return to their gaseous form [11], [18]. Aerojet Rocketdyne, formerly known as GenCorp, is a company that has produced hydrogen compressors for use in various space and defence applications.

A hydrogen cryogenic compressor is a device used to compress hydrogen gas by cooling it to extremely low temperatures, typically below -150 °C; at this point it becomes a liquid and can be stored at high pressures. This process allows for efficient storage and transport of hydrogen gas, which would otherwise be difficult to store and transport in its gaseous form [18], [31].

The working principle of a hydrogen cryogenic compressor is based on the liquefaction of hydrogen gas. Hydrogen gas is drawn into the compressor and cooled by a refrigeration unit, which reduces its temperature to below -150 °C. The liquid hydrogen is then stored in a high-pressure storage vessel, where it can be stored at high pressures. When the compressed hydrogen is needed, it is drawn out of the storage vessel and heated to return it to its gaseous form. This increase in temperature causes the gas to expand, which reduces its pressure. The compressed hydrogen is then ready to be used for fuelling hydrogen-powered vehicles or for other applications that require high-pressure hydrogen. Some of the companies

that produce cryogenic compressor systems include: Linde Group, Cryomotive, Baker Hughes Company.

Electrochemical compressors use an electrochemical process to compress gases, such as hydrogen. This process involves the transfer of electrons from one electrode to another in a cell, which is typically a proton exchange membrane (PEM) cell. The transfer of electrons results in the compression of hydrogen gas, which can then be stored in a high-pressure storage vessel [30].

The hydrogen gas to be compressed is drawn into the compressor. Hydrogen gas is then fed into the PEM cell, where it is electrolyzed into hydrogen ions and electrons. The hydrogen ions are drawn through the membrane, and the electrons are transferred from one electrode to another, resulting in the compression of hydrogen gas. The compressed hydrogen is then stored in a high-pressure storage vessel, where it can be used when needed. When the compressed hydrogen is needed, it is drawn out of the storage vessel and expanded, reducing its pressure. The compressed hydrogen is then ready to be used. There are several companies that are currently developing and producing electrochemical compression systems for various applications. Here are some of the companies that are involved in this field:

These studies [32], [33] present a detailed model of electrochemical hydrogen compressors and experimental investigation also is performed [34].

Electrochemical compressors are a relatively new technology, and there are currently only a few companies that produce them. Here are some of the companies that are involved in this field: HyET Hydrogen, Nuvera H2Pump, Giner Inc. The performance data are presented in Table 2.

Table 2. Comparison of Performance Data of Non-mechanical Compressors

Key factors	**Performance**
Efficiency	Electrochemical compressors are known for their high efficiency, while hydrogen cryogenic compressors are also known for high compression ratios. Adsorption compressors have a relatively high efficiency, but with a lower compression ratio compared to cryogenic compressors. Metal hydride compressors also have a high compression ratio, but the efficiency may be impacted by heat dissipation.
Flow rate	Electrochemical compressors typically have low flow rates, making them suitable for small-scale applications where a low flow rate is sufficient. Adsorption compressors, metal hydride compressors, cryogenic compressors can have relatively high flow rates.
Pressure capability	Electrochemical compressors have lower pressure capabilities compared to other types of compressors. Adsorption compressors, metal hydride compressors, cryogenic compressors have high pressure capabilities.
Maintenance	Electrochemical compressors require relatively little maintenance, as they have few moving parts and are relatively simple in design. Adsorption compressors are relatively simple in design and require minimal maintenance. However, regular cleaning and monitoring are still necessary. Cryogenic compressors require regular maintenance, as they have complex systems that need to be monitored and maintained. This includes cooling systems, refrigeration systems, and other components that may require cleaning or repair. Metal hydride compressors require regular maintenance, as they have complex systems that need to be monitored and maintained.
Cost	Electrochemical compressors are generally more expensive compared to other compression methods. Hydrogen cryogenic compressors and metal hydride compressors can also be expensive, due to their complex systems and cooling requirements. Adsorption compressors, on the other hand, are relatively simple and compact, which makes them more cost-effective.

The studies [33], [34] consider the use of high-pressure hydrogen at refuelling stations for electric cars and analyse the technical properties of modern hydraulic compressors used for hydrogen accumulation. The studies propose an enhanced design of a hydraulic compressor that uses fluid flow meters in a control system for continuous monitoring of the hydrogen compression process, increasing the reliability of the control system operation. The proposed device is a hydraulic hydrogen compressor that consists of a tank for low-pressure hydrogen storage, three operating cylinders of the first and second compression stages, a buffer cylinder for high-pressure hydrogen storage, and a hydraulic compression system with a tank for working fluid and a high-pressure liquid transfer pump. The system is controlled by servo-controlled valves and fluid flow meters that regulate the flow of hydrogen and working fluid.

The proposed hydraulic hydrogen compressor has advantages such as increased reliability due to the use of fluid flow meters, high compression ratios and efficient hydrogen storage. However, it also has drawbacks such as the requirement for replenishing and disposing of working fluid. The hydraulic compression system required for a hydraulic hydrogen compressor can be more complex and expensive than other compression systems.

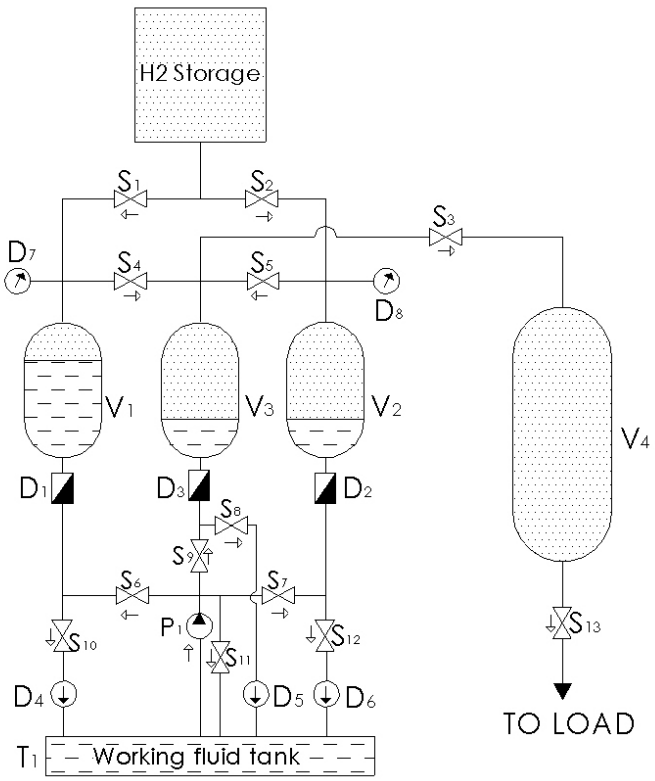

Fig. 4. Scheme of hydraulic compression system (D_1, D_2, D_3, D_4, D_5, D_6, D_7, D_8 – fluid flow meter, V_1, V_2, V_3 – operating cylinders, V_4 – cylinder for high-pressure hydrogen storage, P_1 – pump, S_1 to S_{13} – servo-controlled valves).

4. LIFE CYCLE COST OF HYDROGEN COMPRESORS

Life cycle cost analysis (LCC) is a valuable tool used to evaluate different options by considering all the costs associated with a system or product over its entire life cycle, including purchase, installation, operation, maintenance, and disposal costs. By accounting for all these costs, LCC provides a more accurate picture of the total cost of ownership of a system or product than just considering the initial purchase price. In many scientific works related to hydrogen technologies, life cycle cost analysis is used to assess the economic viability of hydrogen production, storage, and utilization over the entire life cycle of the system or process.

For example, the life cycle cost analysis has been used to investigate the techno-economic feasibility of green hydrogen production. The studies [37]–[39] include the entire supply chain, from the production of hydrogen with renewable energy sources to its final use as a fuel for mobility.

In the case of compressor systems, LCC can be used to compare different compressor options based on their total cost of ownership over their lifetime. This can help companies make informed decisions on which compressor system to invest in, as it considers all the costs associated with each option. While LCC has some limitations, it is a valuable tool for establishing a baseline for making a well-informed decision, and it can be combined with other analysis tools to help account for unexpected costs or business growth. The Life Cycle Cost (LCC) equation for a hydrogen compressor system takes into account the total cost of ownership over the entire life cycle of the system. The general LCC equation for a hydrogen compressor system can be expressed as:

$$LCC = IC + MC + RC + OC,$$

where

IC = Initial capital cost of the compressor system, including purchase and installation;

MC = Maintenance and repair costs over the useful life of the system;

RC = Replacement and disposal costs at the end of the system useful life;

OC = Operating costs, including energy consumption, fuel costs, and other related expenses over the useful life of the system.

To calculate the LCC for a specific hydrogen compressor system, the costs and variables for each of these factors must be estimated and calculated based on the expected life of the compressor system, the expected maintenance requirements, the expected energy and fuel costs, and other relevant factors.

It is important to note that the LCC equation for a hydrogen compressor system is a simplified model and may not account for all possible costs and variables. It is necessary to perform a detailed analysis that considers all relevant costs and factors for a given application in order to accurately assess the total cost of a hydrogen compressor system.

5. CONCLUSIONS

The compression of hydrogen gas is an important aspect of hydrogen energy storage, as it enables the storage of large quantities of hydrogen in a relatively small space.

The study has described two different types of hydrogen compressors: non-mechanical and mechanical. To compare the performance data of different hydrogen compressors, key metrics has been described, such as efficiency, flow rate, pressure capability, maintenance and cost.

The choice of hydrogen compressor depends on the specific application and requirements. However, advancements in technology and increased production volumes help reduce the costs of hydrogen compression, making it a more viable option for energy storage and other applications. Further research and development in this field is expected to lead to even more efficient and cost-effective hydrogen compression systems in the future.

ACKNOWLEDGEMENT

The study has been financed by ERDF project "Experimental Studies and Development of Technology on Hydraulic Compression of Hydrogen" No 1.1.1.1/20/A/185.

REFERENCES

1. International Energy Agency (n.d.). Available at https://www.iea.org/.
2. European Commission. (n.d.). A European Green Deal Available at https://commission.europa.eu/strategy-and-policy/priorities-2019-2024/european-green-deal_en/.
3. Kim, M. S., Jeon, H. K., Lee, K. W., Ryu, J. H., & Choi, S. W. (2022). Analysis of Hydrogen Filling of 175 Liter Tank for Large-Sized Hydrogen Vehicle. *Appl. Sci., 12* (10), 4856. doi: 10.3390/app12104856.
4. Xue, L., Deng, J., Wang, X., Wang, Z., & Liu, B. (2022). Numerical Simulation and Optimization of Rapid Filling of High-Pressure Hydrogen Storage Cylinder. *Energies, 15* (14), 2022. doi: 10.3390/en15145189.
5. Zhao, B., Wei, H., Peng, X., Feng, J., & Jia, X. (2022). Experimental and Numerical Research on Temperature Evolution during the Fast-Filling Process of a Type III Hydrogen Tank. *Energies, 15* (10). doi: 10.3390/en15103811.
6. Heitsch, M., Baraldi, D., Moretto, P., & Heitschec, M. E. (2009). Simulation of the Fast Filling of Hydrogen Tanks. *Proc. 3rd Int. Conf. Hydrog. Saf. (ICHS 3)*, 1–12, [Online]. Available at https://h2tools.org/sites/default/files/2019-08/Simulation of the Fast Filling of Hydrogen Tanks.pdf.
7. Li, M., Bai, Y., Zhang, C., & Song, Y. (2019). Review on the Research of Hydrogen Storage System Fast Refueling in Fuel Cell Vehicle. *Int. J. Hydrogen Energy*, *44* (21), 10677–10693. doi: 10.1016/j.ijhydene.2019.02.208.
8. Melideo, D., Baraldi, D., Acosta-Iborra, B., Ortiz Cebolla, R., & Moretto, P. (2017). CFD Simulations of Filling and Emptying of Hydrogen Tanks. *Int. J. Hydrogen Energy*, *42* (11), 7304–7313. doi: 10.1016/j.ijhydene.2016.05.262.
9. Gonin, R., Horgue, P., Guibert, R., Fabre, D., Bourguet, R., Ammouri, F., & Vyazmina E. (2022). A Computational Fluid Dynamic Study of the Filling of a Gaseous Hydrogen Tank under Two Contrasted Scenarios. *Int. J. Hydrogen Energy, 47* (55), 23278–23292. doi: 10.1016/j.ijhydene.2022.03.260.
10. Sdanghi, G., Maranzana, G., Celzard, A., & Fierro V. (2020). Towards Non-Mechanical Hybrid Hydrogen Compression for Decentralized Hydrogen Facilities. *Energies*, *13* (12). doi: 10.3390/en13123145.
11. Biaek, A., Bielawski, P., & Lotos, G. S. A. (2018). Failure Analysis of Refinery Hydrogen Reciprocating Compressors. *Diagnostyka, 19* (1), 83–92. doi: 10.29354/diag/82961.

12. Navarro, E., Granryd, E., Urchueguía, J. F., & Corberán, J. M. (2007). A Phenomenological Model for Analyzing Reciprocating Compressors. *Int. J. Refrig., 30* (7), 1254–1265. doi: 10.1016/j.ijrefrig.2007.02.006.
13. ISO. *ISO 15869. This Standard Specifies Requirements for High-Pressure Hydrogen Storage Vessels, Including Design, Manufacture, Inspection, Testing, and Certification*. Available at https://www.iso.org/standard/52871.html.
14. Energy. (n.d.). *Hydrogen Storage*. Available at https://www.energy.gov/eere/fuelcells/hydrogen-storage.
15. ISO. (2019). *ISO 14687:2019. Hydrogen Fuel Quality — Product Specification*. Available at https://www.iso.org/standard/69539.html.
16. ISO. (2015). *ISO/TR 15916:2015. Basic Considerations for the Safety of Hydrogen Systems*. Available at https://www.iso.org/standard/56546.html.
17. Sdanghi, G., Maranzana, G., Celzard, A., & Fierro, V. (2018). Review of the Current Technologies and Performances of Hydrogen Compression for Stationary and Automotive Applications. *Renew. Sustain. Energy Rev.*, *102*, 150–170. doi: 10.1016/j.rser.2018.11.028.
18. Wang, T., Jia, X., Li, X., Ren, S., & Peng, X. (2020). Thermal-Structural Coupled Analysis and Improvement of the Diaphragm Compressor Cylinder Head for a Hydrogen Refueling Station. *Int. J. Hydrogen Energy, 45* (1), 809–821. doi: 10.1016/j.ijhydene.2019.10.199.
19. Jia, X., Chen, J., Wu, H., & Peng, X. (2016). Study on the Diaphragm Fracture in a Diaphragm Compressor for a Hydrogen Refueling Station. *Int. J. Hydrogen Energy*, *41* (15), 6412–6421. doi: 10.1016/j.ijhydene.2016.02.106.
20. Li, X., Chen, J., Wang, Z., Jia, X., & Peng, X. (2019). A Non-Destructive Fault Diagnosis Method for a Diaphragm Compressor in the Hydrogen Refueling Station. *Int. J. Hydrogen Energy, 44* (44), 24301–24311. doi: 10.1016/j.ijhydene.2019.07.147.
21. Wennemar J. (2009). *Dry Screw Compressor Performance and Application Range*. 156 Proc. of Thirty-Eighth Turbomach. Symp. (pp. 149–156).
22. Di Bella, F. A. (2015). *Development of a Centrifugal Hydrogen Pipeline Gas Compressor.* Available: https://www.osti.gov/biblio/1227195-development-centrifugal-hydrogen-pipeline-gas-compressor.
23. Wang, H., Yang, D., Zhu, Z., Zhang, H., & Zhang, Q. (2023). Effect of Interstage Pipeline on the Performance of Two-Stage Centrifugal Compressors for Automotive Hydrogen Fuel Cells. *Appl. Sci., 13* (1). doi: 10.3390/app13010503.
24. Lototskyy, M.V., Yartys, V.A., Pollet, B.G., & Bowman, R.C. (2014). Metal Hydride Hydrogen Compressors: A Review. *Int. J. Hydrogen Energy, 39* (11), 5818–5851. doi: 10.1016/j.ijhydene.2014.01.158.
25. Peng, Z., Li., Q., Ouyang, L., Jiang, W., Chen, K., Wang, H., … & Zhu, M. (2022). Overview of Hydrogen Compression Materials Based on a Three-Stage Metal Hydride Hydrogen Compressor. J. *Alloys Compd., 895,* 162465. doi: 10.1016/j.jallcom.2021.162465.
26. Stamatakis, E., Zoulias, E., Tzamalis, G., & Massina, Z. (2018). Metal Hydride Hydrogen Compressors: Current Developments and Early Markets. *Renew. Energy, 127*, 850–862. doi: 10.1016/j.renene.2018.04.073.
27. Muthukumar, P., Maiya, M. P., & Murthy, S. S. (2005) Experiments on a Metal Hydride Based Hydrogen Compressor. *Int. J. Hydrogen Energy, 30* (8), 879–892. doi: 10.1016/j.ijhydene.2004.09.003.
28. Laurencelle, F., Dehouche, Z., Morin, F., & Goyette, J., (2009). Experimental Study on a Metal Hydride Based Hydrogen Compressor. *J. Alloys Compd., 475*, (1–2), 810–816. doi: 10.1016/j.jallcom.2008.08.007.
29. Marciuš, D., Kovač, A., & Firak, M. (2022) Electrochemical Hydrogen Compressor: Recent Progress and Challenges. *Int. J. Hydrogen Energy, 47* (57), 24179–24193. doi: 10.1016/j.ijhydene.2022.04.134.

30. Bampaou, M., Panopoulos, K. D., Papadopoulos, A. I., Seferlis, P., & Voutetakis, S. (2018). An Electrochemical Hydrogen Compression Model. *Chem. Eng. Trans., 70,* 1213–1218. doi: 10.3303/CET1870203.
31. Nordio M., Rizzi, F., Manzolini, G., Mulder, M., Raymaker, L., Van Sint Annaland, M., & Gallucci, F. (2018). Experimental and Modelling Study of an Electrochemical Hydrogen Compressor. *Chem. Eng. J., 369*, 432–442. doi: 10.1016/j.cej.2019.03.106.
32. Stefan, M. (2014). Linde Pioneers Hydrogen Compression Techniques for Fuel Cell Electric Vehicles. *Fuel Cells Bulletin, 2014* (9), 12–15.
33. Ströbel, R., Oszcipok, M., Fasil, M., Rohland, B., Jörissen, L., & Garche, J. (2002). The Compression of Hydrogen in an Electrochemical Cell Based on a PE Fuel Cell Design. *J. Power Sources, 105* (2), 208–215. doi: 10.1016/S0378-7753(01)00941-7.
34. Bezrukovs, V., Bezrukovs, V., Konuhova, M., Bezrukovs, D., & Berzins, A. (2022). Hydrogen Hydraulic Compression System for Refuelling Stations. *Latv. J. Phys. Tech. Sci., 59* (3), 96–105. doi: 10.2478/lpts-2022-0028.
35. Bezrukovs, V., Bezrukovs, Vl., Bezrukovs, D., Orlova, S., Konuhova, M., Berzins. A., … & Pranskus, P. (2021). Hydrogen Hydraulic Compression Device. *PCT/IB2021/058102.*
36. Viktorsson, L., Heinonen, J. T., Skulason, J. B., & Unnthorsson, R. (2017). A Step Towards the Hydrogen Economy - A Life Cycle Cost Analysis of a Hydrogen Refueling Station. *Energies, 10* (6), 1–15. doi: 10.3390/en10060763.
37. Tang, O., Rehme, J., & Cerin, P. (2022). Levelized Cost of Hydrogen for Refueling Stations with Solar PV and Wind in Sweden: On-Grid or Off-Grid?," *Energy, 241,* 122906. doi: 10.1016/j.energy.2021.122906.
38. Correa, G., Volpe, F., Marocco, P., Muñoz, P., Falagüerra, T., & Santarelli, M. (2022). Evaluation of Levelized Cost of Hydrogen Produced by wind Electrolysis: Argentine and Italian Production Scenarios. *J. Energy Storage, 52*. doi: 10.1016/j.est.2022.105014.

sciendo

LATVIAN JOURNAL OF PHYSICS
AND TECHNICAL SCIENCES
2023, N 2

DOI: 10.2478/lpts-2023-0008

RELIABLE DATA PROFILING FOR ENERGY COMMUNITIES – REVIEW OF OPEN-SOURCE APPROACHES

E. Kairisa[1]*, A. Mutule[2]

[1] Institute of Power Engineering, Riga Technical University
[2] Institute of Physical Energetics, Smart Grid Research Centre
*e-mail: Evita.Kairisa@rtu.lv

Meeting the challenges of the energy sector relies on data – in particular sharing it internally and externally with a wide range of partners. Unfortunately, this valuable data often cannot be obtained from real objects due to location specifics or privacy concerns, although accurate, open-source data are a priority to provide researchers and energy experts with the information needed to accelerate the energy transition. In recent years, many studies have focused on the development of energy communities, using different methods to create data for case studies; however, these methods are often too broad and do not correlate with conditions in real locations.

This work aims to identify the challenges associated with creating realistic datasets for energy community studies, as well as highlight the methods of defining input data, considering the factors that make energy community studies a very complex task, and discuss the flaws of commonly used methods.

Keywords: *Energy community, electric load, renewable energy, profiling, modeling, policy, open-source data, open-source tools.*

1. INTRODUCTION

Widespread interest in energy communities is steadily growing in many European countries as citizens realize their potential to drive the energy transition. The term "energy community" has been widely used even before the adoption of the "Citizen energy community" (CEC) in the Electricity Directive and "Renewable energy community" (REC) in the Renewable Energy Directive. In its essence, both CEC and REC are open and voluntary and incorporate non-commercial, environmental and social benefits. Previous studies found that the most important aspects of joining CEC and REC were emission reduction, community building, energy cost reduction and grid stability [1]. The authors of [2], [3] have discussed the difference between CEC and REC in great detail, considering many concepts and overlap definitions. Both terms share several common features and essential differences. Unlike CEC, REC requires proximity to renewable energy projects, focuses only on renewable energy and must be autonomous in its internal decision making. In this paper, we will emphasise CEC rather than REC.

There is still a large scope of unanswered questions for researchers to explore CECs, often motivated by the EU's ambitious climate and energy plans, which aim to reduce 55 % of net greenhouse gas (GHG) emissions by 2030 [4]. Some potential topics include analysing how and where to place energy resources most optimally, assisting with legal and administrative processes [5]–[7], creating new business models [8]–[10], performing choice surveys [11], [12] and feasibility analysis, and developing new smart energy solutions, such as demand response techniques [13], [14] and energy storage, studying new loads, such as electric vehicles [15], [16] or heat pumps [17]. This versatility, together with the rising number of active actors, such as aggregators and EV charging infrastructure providers, creates new requirements for data exchange and analytics. As a result, the European energy sector is moving towards a more inclusive system that embraces digitalization, a wider variety of stakeholders, and new organisational processes. However, to achieve these goals, there is a need for data that often cannot be obtained from real objects and real CECs due to location specifics or privacy concerns. For example, in Austria, the distribution of shared energy is done by the distribution system operator (DSO), not allowing for real-time management based on smart meter data [2]. Therefore, new data acquisition and analytic methods could bring fresh ideas to the stakeholders across the energy value chain, not to mention that data have been defined by European Commissioner for Digital Agenda as the 'new gold' of the digital era.

The main principles of Open Data are to encourage the free use and reuse of information by ensuring that the data or code is both accessible and legally usable. Yet, a legal definition of what constitutes Open Data has not been provided in either statutes or case law. To illustrate, the Open Power System Data project [18] is building an online data platform for free and open data for power system modelling, including data on power plant capacities and locations and renewable production time series from transmission system operators.

The paper attempts to provide answers to the following research questions, which

will be addressed through the literature review and answered in the discussion:

1. How can we make reliable load profiles for CEC if each of existing CEC is unique? For example, they can use different technology, ownership structure, and have different level of local participation.
2. Is it useful to use annual statistics if CEC differs from the rest of households and even differs from each other?
3. How to make reliable load profiles with limited information?
4. How to choose open-source datasets and tools?

With this research, we contribute toward openness in energy research. Open data questions are linked to the following paradox – the creation of innovations often requires openness, but the process of commercialization of innovations necessitates closure [19]. Open should not just mean releasing resources into a digital void; the term should stand for managing the use of resources in a way that maximizes public benefit while avoiding harm, maintaining a balance between openness of resources and preservation of privacy.

2. METHODOLOGY

This section outlines the methodology, assumptions, and objectives applied in this paper. Firstly, the authors conducted a comprehensive analysis of the various factors that shape the characteristics of each CEC, such as location, local constraints, and hindering and facilitating factors, as well as emphasized the importance of open-source data and tools. Then the analysis of commonly used open-source data and tools in recent research papers was performed to find links between research problems and used data generation methods. In the discussion, the authors answer the questions posed in the introduction and provide views on how to address a shortage of data.

2.1. CEC Factors

For the research that contributes to the development of CEC, there is a need for good-quality data for case studies, in particular reliable load profiles. To address this problem, we need a better understanding of the links between energy consumption and supply on the one side and local challenges, benefits, and energy configurations on the other. The rules of the community, the source of energy used, and the relationships between its members will vary from region to region, and even from community to community within the same region. Because of a high number of hindering and facilitating factors, energy systems evolve differently in different countries and regions. EU law, therefore, requires all member states to assess the barriers and potential of communities in their territories. In this study, we classified all identified factors that influence the development of CECs as (a) cultural and behavioral factors (societal norms, culture of local energy activism), (b) legal factors (legal framework and support mechanisms), and (c) technical factors (existing grid capacity and occurrence of grid congestions).

Cultural and behavioral factors would be the first logical condition to consider for a collective energy project as it forms the basis for the whole development of the CEC. Firstly, in countries where the cooperative movement has an old and well-established tradition, people know about

this legal structure and are aware of its benefits [20]. In Germany and Denmark, the strong tradition of community ownership and social enterprises has resulted in a high number of citizen-led energy organisations compared to rest of Europe [21]. On the contrary, in Croatia cooperatives have a negative connotation given the past political system [2]. Secondly, by understanding the social characteristics of communities, the best variations of technologies can be chosen that comply with conditions in a selected location. The general intent should be to choose the energy sources by taking advantage of the resources locally available for stimulating the local economy. Also, the attention paid to local needs would increase the social acceptability of RES-based plants [22]. Yet, in some regions, backlash tends to be focused on wind energy. For example, in Ireland, onshore wind energy was accepted as a solution to support decarbonization [23], considering that the capacity factor for solar PV is 10 % compared to 30 % for wind [24]; however, the public generally preferred solar generation.

Local policies and regulations form the environment in which the market operates, thus significantly influencing the local engagement and the type of projects that succeed. Low acceptability, low economic viability, and perceived limited potential often result from unsupportive institutional conditions [23], such as complex and long-lasting legal processes and frameworks that favour larger companies. The EU framework that supports energy transition is implemented into national policies, strategies, and action plans, leaving many details of the transposition process to the national level. The degree of detail in the respective legislative documents strongly differs among the Member States, ranging between basic definitions and elaborated frameworks. For instance, in Greece, the policy is highly fragmented, scattered, and even conflicting [2], which has a major impact as the lack of clear legal definitions is considered one of the main barriers for the further development of CEC.

Difficulty accessing financial capital and lack of support mechanisms are other political obstacles for CEC, but experienced energy consultant companies can strive as an enabling factor. A feed-in tariff (FiT) has become the most widespread policy instrument for CEC, offering a clear financial planning horizon but also creating dependence on this support framework as changes to the FiT can lead to critical financial consequences. Taking Germany as an example, the recent drop in new projects shows how vulnerable community projects are if a FiT is changed or substituted with other payment systems. Low disposable income is another barrier for a person to join a CEC. Cooperation banks, low-interest loans, and crowdfunding are solutions to enable the emergence of new energy communities. For example, in France, crowdfunding has experienced strong growth, and it has been found that the main facilitating factor of the investment decision is the transparency of the investment offers [25]. Indeed, when support schemes have been straightforward and consistent, community energy projects flourish. A clear example of benefits from funding programs for local renewable energy projects is the development on the Danish island of Samsø [26], where the island's energy system was largely transformed in period of 10 years.

Umbrella organisations and energy consultant companies are also important enabling factors. As mentioned above, close relations with an experienced energy consultant company can facilitate the necessary techno-economic analyses and ease the application process for national funding. Likewise, these intermediaries give a plat-

form for sharing best practices and learning between CECs. For example, in the United Kingdom, the Netherlands, and Germany, CECs are mostly part of larger cooperative organisations. The United Kingdom has, for example, Community Energy England, but the Netherlands has the umbrella organisation Energi Samen [27].

The third factor to consider before making representative load profiles is technical factors, for example, inadequate grid access. In some areas, access to the grid is a challenge, for example, due to the high costs of the connection or inconvenient technical requirements that were designed for big utilities [28]. For this reason, processing time can be particularly long and difficult because for-profit grid operators do not see it in their interest to connect CEC projects. For instance, in the Republic of Ireland, accessing a grid connection for a community energy project is almost impossible [29] as applications for a grid connection can take years, during which time projects cannot progress. Other elements of local context, for example, the available potential of renewable sources, dependency on fossil fuel import, and arbitrary technical limitations, considerably alter citizen engagement and the optimal resource mix.

A high dependency on fossil fuel imports is considered an enabler for CECs to emerge. For example, in Denmark, which was entirely dependent on fossil fuels until the 1970s oil crises, severe concerns about the security of the energy supply resulted in turning to renewable energy [30]. Arbitrary limitations, such as geographic scope, exported generation limits, and other restrictions, act as hindering factors. For example, in Spain, there is a geographic limitation of 500 m, but in Greece, energy cooperatives can produce, distribute, and supply renewable energy from installations up to 3 MW. Also, in Austria, with many small DSOs, larger plants may face restrictions in being connected to the LV grid [31].

CECs are energy innovations, and residents are unwilling to participate without benefits. The above-mentioned list of benefiting and hindering factors is unique in each country and makes energy community modelling very challenging as CEC motives are heterogeneous and complex. Such diversity makes standard data modelling approaches inapplicable, although collecting real data is not often possible because of legal reasons.

2.2. Importance of Open Data and Tools in Energy Communities

In the previous section, we highlighted commonalities and diversity for different European regions, providing insight into the variations in CEC options and stakeholder preferences. After a detailed analysis of a specific area, suitable open-source datasets and tools can be explored to create representative load profiles. A large amount of input data is required to be able to model an energy system as close as possible to the real world, not only with hour-by-hour load and generation data but, depending on modelling purpose, also with information on existing power plants, fuel cost, electricity prices, and other time series, tabular or geospatial data.

The authors of [32] reveal that the legality of current data acquisition practices in energy modelling is doubtful, as electricity system modelers quite regularly use freely-available data without being aware of license conditions and legal framework. A straightforward solution is the rise of open data, which facilitates more effective and higher-quality science and greater productivity through less duplicated effort. In contrast to closed models, “open” models must come with an open data license and imply

that anyone can freely access, use, modify, and share both model code and data for any purpose. In more detail, the researchers should be legally able to make a local copy, machine-process, and amend that data, pass on such amended data to other users, or publish amended data for scientific reproducibility. Therefore, "public" data are not identical to "open", as publicly available data might be freely accessible to others, but their reuse is restricted by copyright and related rights. The Open data handbook [33] provides information on how to make datasets open, as making a database available online does not imply that it can be used freely. The term "open" brings high standards to data in terms of quality, privacy, and anonymity. In reality, open data are heterogeneous and widely varying in terms of quality, formats, frequency of updates, support, etc.

The authors of [34] identified few reasons why data and tools should be open for researchers and the general public. The first is improved quality of science, which occurs from broader access to information, greater transparency, reproducibility, and traceability. The second one is a more effective collaboration which also leads to increased productivity through collaborative sharing. The last reason is provoking societal debates, leading to more citizen participation and engagement. The same authors also identified four reasons why most models and data were not open: 1) ethical and security concerns, 2) unwanted exposure, 3) additional workload, and 4) complex and uncoordinated institutional setups. Yet one of the main challenges remains the lengthy process spent transforming these datasets from their original raw form rather than developing and improving the learning model itself.

Data used in energy community studies can be historically measured or synthetic data. The use of historical data in CEC modelling is quite rare as most sites have not executed similar projects before. One example of using historical data from the real energy community is [35], which used historical data from Chalmers University's local Energy Community in Sweden to make Energy Management System that performs PV generation and load forecasting and then optimizes the scheduling problem. However, in most cases, the lack of on-site data from real entities means that stakeholders often work in the dark while planning and operating their CECs.

A common practice is a synthesis of the load profiles, for example, using standard load profiles, the probability-based approaches (consisting of a set of rules and their probability), or using national survey datasets on energy use. As an example, the authors of [36] simulated retrofit scenarios with different technology mixes and investigated the impact of each scenario on the energy community located in North-West of Italy. Scenarios were created with the methodology established by [37], which used both a probability-based approach and exploited the results of the Italian national survey and other statistical information on the population. On the contrary, [38] used standard load profiles for annual electricity demand time-series to estimate the effect of high penetration of energy communities in the residential sector, but [39] developed an agent-based simulation model that models every occupant of the household as an independent, desire-driven software agent. Another common approach is using historical data from open-source datasets. It can be observed that the Pecan Street dataset is one of the most favoured open-source datasets in the energy community research papers, such as [40] where it was used with a genetic algorithm to investigate the optimal allocation of the prosumers in the communities.

In most cases, papers that collected actual historical on-site data for research purposes will not release that data as open-source. However, in some cases, authors provide case study data through GitHub, for example [41]. Similarly, modelling tools created for making synthetic load profiles can be both open and closed models. If scenario development is just the first step in a research effort, open-source datasets and tools can be critical to improving scientific efficiency. To be specific, researchers can focus on their main research subject instead of creating separate models for data acquisition. The importance of sharing data, experiences, and knowledge between energy communities and users from various backgrounds is highlighted in [42], presenting the architecture, design, prototyping, and testing of the digital support platform ECCO OSS. The primary goal of this digital platform is to assist energy communities to develop successful energy projects, engage early-stage groups to progress projects and connect and share experiences with other communities by creating new communication channel with one-stop-shop architecture. This platform can contribute to maximizing the ease and simplicity of participation and experimentation for innovators and early adopters, ensuring strong support for early and late majorities, and providing data to policymakers to develop evidence-based policy interventions.

2.3. Open Energy Datasets for Energy Communities

The development of any industry is hardly possible without the availability of data; therefore, we are willing to highlight the value that data can bring to society, quality of life, and environmental protection. Some papers have already collected and analysed the availability of energy demand and supply data, such as [43] without considering if these data sources are actually used in energy community research papers. In this review, research papers from the last five years were selected to analyse the open-source datasets used in energy community studies. For this review, research papers were selected from the SCOPUS database, using the keywords: "energy community", "citizen energy community", "open data", etc. Other sources of information were review papers listing commonly used open-source datasets, such as [43] – [45]. The results are summarised in the following Github repository: **https://github.com/EvitaKairisa/Review-of-open-source-approaches**, consisting of three pdf files. Results include information about the dataset, publications they are used, and the most frequently used and descriptive keywords.

From "open-data_datasets.pdf" file, it is noticeable that the most popular datasets in energy community research papers in the last five years were the Pecan Street dataset and the OPSD data platform. Both datasets contain power demand and generation data, therefore being useful for modelling energy communities. Another advantage of the Pecan Street dataset for the analysis of energy community is that the Pecan Street dataset contains a large number of residents and buildings over multiple years. It consists of 1000 households and private and public activities located in Austin (Texas): single houses, apartments, small commercial activities, and public schools. However, these data are only partially open-source. Based on common keywords, this kind of data is beneficial for articles about demand-side management, energy management systems, peer-to-peer trading, resource man-

agement, etc. Some papers used only time series from households, for example, [46] used one-year consumption and generation data of all households and computed the deficiency and excess of energy for every household. Other papers used data from a shorter period or smaller number of households, for example, [47] only used data from June 2019, but [48] selected 12 households' data on electricity use and solar production between 1 and 7 June 2016, where nine households had rooftop PV panels. OPSD data platform consists of multiple useful load and power generation datasets of varying nature and thus applicability. Some files provide measurements for individual PV generation and electricity consumption with a resolution for up to a single device, thus suited for demand response research papers. Other files provide national-level historical data, for example, [49] focuses on the addition of wind power to the national grid, which is implemented by scaling historical generation data.

Other datasets from the table appear less often in research papers, probably due to a smaller number of end-users or a shorter data collection period. For example, [50] used the IEEE dataset and generated energy flexibility for each end-user using a normal distribution with a mean of 15 % and a standard deviation of 5 %.

In addition to the time series of demand and supply, other exogenous factors may influence the functioning of a CEC, such as ambient conditions and electricity prices. Local weather conditions are among the most prominent drivers behind energy demand and energy flexibility in a CEC at any given time. Climate-related data are often obtained from Meteonorm time series, OpenWeatherMap, EnergyPlus weather data repository, or various reanalysis datasets. For example, the ERA5 reanalysis dataset provides a number of meteorological data fields through a separate reanalysis product to optimally combine historical data with future forecasts.

2.4. Open-Source Tools for Energy Communities

It is expected that the electricity, heat, and transport sectors could become more tightly connected in the future due to the deployment of heat pumps and electric vehicles. CECs are no exception – the review [51] researched 76 different Energy Communities located in 11 European countries, and results showed that 13.1% of CEC included energy storage, 4.4 % heat pumps and 8.0 % electric vehicles. To create input data for new and more complex coupled models, open-source tools are more fitting than open-source datasets. The authors of [52] identified five essential features of open-source tools: data standardization, interpretability, scalability, adaptability, and reconfigurability. In other words, they should be representative and flexible to be used in different conditions and case studies.

Research papers from the last five years were selected to analyse the open-source tools for energy demand as well. This time, research papers were selected from the SCOPUS database, using the keywords: "energy community", "citizen energy community", "open tools", "synthetic data" etc. The results are summarised in the "open-source_tools.pdf" file in Github repository, including information about the tool, publications they are used, and the most frequently used and descriptive keywords. Compared to the open-source datasets, there is not a high variety of available open-source tools for energy demand simulation in energy community

research papers, thereby each tool is used in several publications. Some researchers prefer using open-source tools rather than open-source datasets, as tools allow for easier customization of input data based on researchers' goals and preferences. Based on common keywords, researchers use synthetic demand data to research energy communities from the smart grid and the electricity market point of view, as well as determine economic performance, operational costs, carbon emissions, etc.

It is noticeable that the most popular tools for demand data in energy community research papers in the last five years were LoadProfileGenerator and EnergyPlus. LoadProfileGenerator creates electricity demand profiles of individual users and varies according to the household category, for example, a family with children, a retiree, etc. This tool does not simulate heat consumption, as it assumes that households are connected to the public heating network. The varying factors for CEC development are, for example, the number of occupants in each household, the work schedule of the occupants, the types of household appliances, and the age group of the occupants.

EnergyPlus is a multi-purpose tool and is often preferred due to its large possibilities for customization. It can generate consumption and load profiles (including heating, cooling, and ventilation loads) using data from representative buildings and selected renewable technologies, as well as obtain weather data and determine economic and environmental performances. For these reasons, keywords from the papers that used EnergyPlus reveal great diversity.

We also would like to highlight a specific type of demand – electric vehicle charging load – and see if CEC research papers are using open-source tools to create time series of electric vehicle (EV) charging. Analysis revealed that few tools for EV charging demand exist, mainly developed as Python packages (such as emobpy and vencopy), but since these tools are currently in the early stages of development, they are still not used in the CEC research papers. A shortcoming of the literature is that not all researchers include EVs in their CEC case studies, mainly focusing on renewable energy generation and increasing communities' efficiency. Papers that include EVs in their case studies mainly determine their EV consumption based on real-world EV charging profiles collected from various surveys. They also establish some assumptions about EV charging, such as manufacturers' energy consumption values, travelled distances during weekdays and weekends, or the assumption that the EVs are charged at home.

In "open-source_generation.pdf" file, we identified only a few open-source tools used in energy community research papers in the last five years to create renewable energy sources (RES) time series. The most used open-source tools for creating RES time series are PVGIS and renewables.ninja. They are highly intuitive tools, therefore easy to use for research purposes. Renewables.ninja produces the PV and wind energy outputs at any given location and for different technological system parameters, such as peak production, azimuth, and tilt. The keywords from research papers are very diverse, as all energy communities contain some renewable energy load. From Tab. 3, assumption can be made that case studies for CECs are based on PV production, since most papers used PVGIS, rather than renewables.ninja.

To conclude, one of the key aspects of energy demand and generation synthesis is the versatility of the tool (e.g., range of end-users) as energy communities

take advantage of a variety of green technologies, and researchers should address emerging synergies with various members and technologies.

3. DISCUSSION AND CONCLUSION

Each CEC must design its project in a way that reflects its local identity, social practice, and cultural values. Many projects rely on case studies for data specific to their locations. However, the high upfront costs to collect and process data can therefore drain enthusiasm for such initiatives. Especially since the value of data becomes visible once it has been collected and analysed. The best way to study a particular energy community is to collect data from that community, which is not plausible for everyone. For now, the second best way is to find a dataset or tool that is the most similar in terms of location (the same country or region), consumption and generation pattern, annual consumption, energy technology, etc. Researchers choose to use open-source datasets that are available to them (with or without scaling, normal distribution, correlation, merging, or adjusting the data) or make synthetic data with different platforms, models, and tools.

Although there are many different open-source datasets and tools, it can be noticed that some of them are more favoured than others. The main factor in selecting the dataset is the location and the number of end-users, the period of time (preferably at least one year), the resolution, and the quality of data (e.g., missing values). For open-source tools, the key factor is the customization options. The authors have noticed that there is a high number of approaches how to adjust data from real-world datasets. A common approach is scaling data according to the average consumption in the respective country. We argue that this logic is flawed as energy communities use energy in different patterns than average consumers, as CEC members tend to have stronger environmental and social goals than the general public. The next common approach is to include some randomness or correlation index.

Nevertheless, none of these solutions can easily be adaptable to real communities due to the high specificity of regulation, the potential presence of different stakeholders in the community, and other factors. Generic scenarios that do not represent real locations do not provide real benefit to the research community as each assumption not made thoughtfully will bias the results and refer to final conclusions. Besides, it is no longer enough to perform modelling for generic scenarios that are not related to the real location. We need to find a way to create data that are as close to the real-world as possible. Therefore, we need to investigate the location in great detail, considering a large number of factors, and carefully selecting the available datasets and tools.

ACKNOWLEDGMENT

This publication was supported by the Doctoral Grant programme of Riga Technical University

REFERENCES

1. Lode, M. L., Heuninckx, S., te Boveldt, G., Macharis, C. & Coosemans, T. (2022). Designing successful energy communities: A comparison of seven pilots in Europe applying the Multi-Actor Multi-Criteria Analysis., *Energy Res. Soc. Sci.*, 90, 102671, doi: 10.1016/J.ERSS.2022.102671.
2. Frieden, D., Tuerk, A., Antunes, A. R., Athanasios, V., Chronis, A. G., D'herbemont, S., Kirac, M., Marouço, R., Neumann, C., Catalayud, E. P., Primo, N. & Gubina, A. F. (2021). Are We on the Right Track? Collective Self-Consumption and Energy Communities in the European Union., *Sustain. 2021,* 13, 12494, doi: 10.3390/SU132212494.
3. REScoop.eu (2019). Q&A: What are "citizen" and "renewable" energy communities?
4. European Commission. 2030 Climate Target Plan., Skatīts: 2022. gada 28. septembrī. [Tiešsaiste]. Pieejams: https://climate.ec.europa.eu/eu-action/european-green-deal/2030-climate-target-plan_en
5. Hoicka, C. E., Lowitzsch, J., Brisbois, M. C., Kumar, A. & Ramirez Camargo, L. (2021). Implementing a just renewable energy transition: Policy advice for transposing the new European rules for renewable energy communities., *Energy Policy*, 156, 112435, doi: 10.1016/J.ENPOL.2021.112435.
6. Mirzania, P., Ford, A., Andrews, D., Ofori, G. & Maidment, G. (2019). The impact of policy changes: The opportunities of Community Renewable Energy projects in the UK and the barriers they face., *Energy Policy*, 129, 1282–1296, doi: 10.1016/J.ENPOL.2019.02.066.
7. Busch, H., Ruggiero, S., Isakovic, A. & Hansen, T. (2021). Policy challenges to community energy in the EU: A systematic review of the scientific literature., *Renew. Sustain. Energy Rev.*, 151, 111535, doi: 10.1016/J.RSER.2021.111535.
8. Ceglia, F., Esposito, P., Marrasso, E. & Sasso, M. (2020). From smart energy community to smart energy municipalities: Literature review, agendas and pathways., *J. Clean. Prod.*, 254, 120118, doi: 10.1016/J.JCLEPRO.2020.120118.
9. Brown, D., Hall, S. & Davis, M. E. (2019). Prosumers in the post subsidy era: an exploration of new prosumer business models in the UK., *Energy Policy*, 135, 110984, doi: 10.1016/J.ENPOL.2019.110984.
10. Botelho, D. F., Dias, B. H., de Oliveira, L. W., Soares, T. A., Rezende, I. & Sousa, T. (2021). Innovative business models as drivers for prosumers integration - Enablers and barriers., *Renew. Sustain. Energy Rev.*, 144, 111057, doi: 10.1016/J.RSER.2021.111057.
11. Soeiro, S. & Ferreira Dias, M. (2020). Community renewable energy: Benefits and drivers., *Energy Reports*, 6, 134–140, doi: 10.1016/J.EGYR.2020.11.087.
12. Horstink, L., Wittmayer, J. M., Ng, K., Luz, G. P., Marín-González, E., Gährs, S., Campos, I., Holstenkamp, L., Oxenaar, S. & Brown, D. (2020). Collective Renewable Energy Prosumers and the Promises of the Energy Union: Taking Stock., *Energies 2020*, 13, 421, doi: 10.3390/EN13020421.
13. Van Cutsem, O., Ho Dac, D., Boudou, P. & Kayal, M. (2020). Cooperative energy management of a community of smart-buildings: A Blockchain approach., *Int. J. Electr. Power Energy Syst.*, 117, 105643, doi: 10.1016/J.IJEPES.2019.105643.
14. Khanna, S., Becerra, V., Allahham, A., Giaouris, D., Foster, J. M., Roberts, K., Hutchinson, D. & Fawcett, J. (2020). Demand Response Model Development for Smart Households Using Time of Use Tariffs and Optimal Control—The Isle of Wight Energy Autonomous Community Case Study., *Energies 2020,* 13, 541, doi: 10.3390/EN13030541.
15. Barbour, E., Parra, D., Awwad, Z. & González, M. C. (2018). Community energy storage: A smart choice for the smart grid?, *Appl. Energy*, 212, 489–497, doi: 10.1016/J.APENERGY.2017.12.056.

16. Rzepka, P., Szablicki, M., Kwiatkowski, B. & Wronka, A. (2019). Vehicle to grid as an important element of the energy community., *Proc. - Int. Conf. Mod. Electr. Power Syst. MEPS 2019*, doi: 10.1109/MEPS46793.2019.9394986.
17. Ceglia, F., Marrasso, E., Roselli, C. & Sasso, M. (2021). Small Renewable Energy Community: The Role of Energy and Environmental Indicators for Power Grid., doi: 10.3390/su13042137.
18. Data Platform – Open Power System Data., Skatīts: 2022. gada 1. decembrī. [Tiešsaiste]. Pieejams: https://data.open-power-system-data.org/
19. Sovacool, B. K., Jeppesen, J., Bandsholm, J., Asmussen, J., Balachandran, R., Vestergaard, S., Andersen, T. H., Sørensen, T. K. & Bjørn-Thygesen, F. (2017). Navigating the "paradox of openness" in energy and transport innovation: Insights from eight corporate clean technology research and development case studies., *Energy Policy*, 105, 236–245, doi: 10.1016/J.ENPOL.2017.02.033.
20. Brummer, V. (2018). Community energy – benefits and barriers: A comparative literature review of Community Energy in the UK, Germany and the USA, the benefits it provides for society and the barriers it faces., *Renew. Sustain. Energy Rev.*, 94, 187–196, doi: 10.1016/J.RSER.2018.06.013.
21. Caramizaru, A. & Uihlein, A. (2019). Energy communities : an overview of energy and social innovation., doi: 10.2760/180576.
22. Ceglia, F., Marrasso, E., Pallotta, G., Roselli, C. & Sasso, M. (2022). The State of the Art of Smart Energy Communities: A Systematic Review of Strengths and Limits., doi: 10.3390/en15093462.
23. EirGrid (2021). Shaping our electricity future.
24. EirGrid (2019). Transmission Forecast Statement.
25. Bourcet, C. & Bovari, E. (2020). Exploring citizens' decision to crowdfund renewable energy projects: Quantitative evidence from France., *Energy Econ.*, 88, 104754, doi: 10.1016/J.ENECO.2020.104754.
26. Sperling, K. (2017). How does a pioneer community energy project succeed in practice? The case of the Samsø Renewable Energy Island., *Renew. Sustain. Energy Rev.*, 71, 884–897, doi: 10.1016/J.RSER.2016.12.116.
27. Palm, J. (2020). Deliverable 3.3. Energy communities in different national settings-barriers, enablers and best practices., Skatīts: 2022. gada 27. septembrī. [Tiešsaiste]. Pieejams: https://www.newcomersh2020.eu/
28. Wainer, A., Petrovics, D. & van der Grijp, N. (2022). The grid access of energy communities a comparison of power grid governance in France and Germany., *Energy Policy*, 170, 113159, doi: 10.1016/J.ENPOL.2022.113159.
29. Friends of the Earth Europe (2021). BARRIERS AND THREATS TO THE PEOPLE-OWNED ENERGY REVOLUTION.
30. Kooij, H. J., Oteman, M., Veenman, S., Sperling, K., Magnusson, D., Palm, J. & Hvelplund, F. (2018). Between grassroots and treetops: Community power and institutional dependence in the renewable energy sector in Denmark, Sweden and the Netherlands., *Energy Res. Soc. Sci.*, 37, 52–64, doi: 10.1016/J.ERSS.2017.09.019.
31. Tuerk, A., Camilla, N., Mątowska, M., Rakocevic, L., van Dijk, E., Hartmann, P., Karg, L., Assalini, S. & Winkler, C. (2022). D3.2 ENERGY COMMUNITIES AND COLLECTIVE ACTIONS: YEARLY POLICY BRIEF ON REGULATION., Skatīts: 2022. gada 23. novembrī. [Tiešsaiste]. Pieejams: https://www.researchgate.net/publication/361189977_ENERGY_COMMUNITIES_AND_COLLECTIVE_ACTIONS_YEARLY_POLICY_BRIEF_ON_REGULATION
32. Hirth, L. (2020). Open data for electricity modeling: Legal aspects., *Energy Strateg. Rev.*, 27, 100433, doi: 10.1016/J.ESR.2019.100433.
33. OPEN DATA HANDBOOK. How to Open up Data., Skatīts: 2022. gada 28. oktobrī. [Tiešsaiste]. Pieejams: https://opendatahandbook.org/guide/en/how-to-open-up-data/

34. Pfenninger, S., DeCarolis, J., Hirth, L., Quoilin, S. & Staffell, I. (2017). The importance of open data and software: Is energy research lagging behind?., *Energy Policy*, 101, 211–215, doi: 10.1016/J.ENPOL.2016.11.046.

35. Mohiti, M., Mazidi, M., Steen, D. & Tuan, L. A. (2022). A Risk-Averse Energy Management System for Optimal Heat and Power Scheduling in Local Energy Communities., *2022 IEEE Int. Conf. Environ. Electr. Eng.*, doi: 10.1109/EEEIC/ICPSEUROPE54979.2022.9854642.

36. Minuto, F. D., Lazzeroni, P., Borchiellini, R., Olivero, S., Bottaccioli, L. & Lanzini, A. (2021). Modeling technology retrofit scenarios for the conversion of condominium into an energy community: An Italian case study., *J. Clean. Prod.*, 282, 124536, doi: 10.1016/J.JCLEPRO.2020.124536.

37. Bottaccioli, L., Di Cataldo, S., Acquaviva, A. & Patti, E. (2019). Realistic Multi-Scale Modeling of Household Electricity Behaviors., *IEEE Access*, 7, 2467–2489, doi: 10.1109/ACCESS.2018.2886201.

38. Zwickl-Bernhard, S. & Auer, H. (2021). Citizen Participation in Low-Carbon Energy Systems: Energy Communities and Its Impact on the Electricity Demand on Neighborhood and National Level., *Energies 2021*, 14, 305, doi: 10.3390/EN14020305.

39. Schlund, J., Pflugradt, N., Steber, D., Muntwyler, U. & German, R. (2018). Benefits of Virtual Community Energy Storages Compared to Individual Batteries Based on Behaviour Based Synthetic Load Profiles., *Proc. - 2018 IEEE PES Innov. Smart Grid Technol. Conf. Eur. ISGT-Europe 2018*, doi: 10.1109/ISGTEUROPE.2018.8571506.

40. Grasso, F., Lozito, G. M., Fulginei, F. R. & Talluri, G. (2022). Pareto optimization Strategy for Clustering of PV Prosumers in a Renewable Energy Community., *MELECON 2022 - IEEE Mediterr. Electrotech. Conf. Proc.*, 703–708, doi: 10.1109/MELECON53508.2022.9843063.

41. Bruck, A., Díaz Ruano, S. & Auer, H. (2021). A Critical Perspective on Positive Energy Districts in Climatically Favoured Regions: An Open-Source Modelling Approach Disclosing Implications and Possibilities., *Energies 2021*, 14, 4864, doi: 10.3390/EN14164864.

42. Burgio, A., Violi, A., Hill, M. & Duffy, A. (2022). A Digital Support Platform for Community Energy: One-Stop-Shop Architecture, Development and Evaluation., *Energies 2022*, 15, 4763, doi: 10.3390/EN15134763.

43. Kazmi, H., Munné-Collado, Í., Mehmood, F., Syed, T. A. & Driesen, J. (2021). Towards data-driven energy communities: A review of open-source datasets, models and tools., *Renew. Sustain. Energy Rev.*, 148, 111290, doi: 10.1016/J.RSER.2021.111290.

44. Jazizadeh, F., Afzalan, M., Becerik-Gerber, B. & Soibelman, L. (2018). A Dataset for Energy Monitoring through Building Electricity Disaggregation., *ACM Ref. format*, doi: 10.1145/3208903.3208939.

45. Haben, S., Arora, S., Giasemidis, G., Voss, M. & Vukadinović Greetham, D. (2021). Review of low voltage load forecasting: Methods, applications, and recommendations., *Appl. Energy*, 304, 117798, doi: 10.1016/J.APENERGY.2021.117798.

46. Kouvelas, N. & Prasad, R. V. (2021). Efficient Allocation of Harvested Energy at the Edge by Building a Tangible Micro-Grid - The Texas Case., *IEEE Trans. Green Commun. Netw.*, 5, 94–105, doi: 10.1109/TGCN.2020.3047432.

47. Zhang, B., Du, Y., Chen, X., Lim, E. G., Jiang, L. & Yan, K. (2022). Potential Benefits for Residential Building with Photovoltaic Battery System Participation in Peer-to-Peer Energy Trading., *Energies 2022*, 15, 3913, doi: 10.3390/EN15113913.

48. Wang, Y., Wu, X., Li, Y., Yan, R., Tan, Y., Qiao, X. & Cao, Y. (2020). Autonomous energy community based on energy contract., *IET Gener. Transm. Distrib.*, 14, 682–689, doi: 10.1049/IET-GTD.2019.1223.

49. Klement, P., Brandt, T., Schmeling, L., de Bronstein, A. A., Wehkamp, S., Penaherrera Vaca, F. A., Lanezki, M., Schönfeldt, P., Hill, A. & Katic, N. (2022). Local Energy Markets in Action: Smart Integration of National Markets, Distributed Energy Resources and Incentivisation to Promote Citizen Participation., *Energies*, 15, 2749, doi: 10.3390/EN15082749/S1.

50. Pereira, H., Faia, R., Gomes, L., Faria, P. & Vale, Z. (2022). Incentive-based and Price-based Demand Response to Prevent Congestion in Energy Communities., *2022 IEEE Int. Conf. Environ. Electr. Eng.*, doi: 10.1109/EEEIC/ICPSEUROPE54979.2022.9854648.
51. Papadimitriou, C. (2020). Introduction and development of Local Energy Communities in Europe.
52. Manfren, M., Nastasi, B., Groppi, D. & Astiaso Garcia, D. (2020). Open data and energy analytics - An analysis of essential information for energy system planning, design and operation., *Energy*, 213, 118803, doi: 10.1016/J.ENERGY.2020.118803.

sciendo

LATVIAN JOURNAL OF PHYSICS
AND TECHNICAL SCIENCES
2023, N 2

DOI: 10.2478/lpts-2023-0009

EFFICIENT HEAT RECOVERY FROM HYDROGEN AND NATURAL GAS BLEND COMBUSTION PRODUCTS

D. Rusovs[1], L. Jansons[2, 3], N. Zeltins[2], I. Geipele[3]

[1]Riga Technical University, Faculty of Mechanical Engineering,
Transport and Aeronautics, Department of Thermal Power Systems,
6b–546 Kipsalas Str., Riga, LV-1048, LATVIA
[2]Riga Technical University, Faculty of Electrical and
Environmental Engineering, Institute of Power Engineering,
12-1 Azenes Str., Riga, LV-1048, LATVIA
[3]Riga Technical University, Faculty of Engineering Economics and
Management, Institute of the Civil Engineering and Real Estate Economics,
6 Kalnciema Str. 210, Riga, LV-1048, LATVIA
*e-mail: dmitrijs.rusovs@rtu.lv

The introduction of hydrogen and natural gas blends in existing gas transportation and distribution networks would ensure faster and more efficient decarbonization of energy sector, but, at the same time, this process would request solution of many practical and technical problems. This paper explores thermodynamics of hydrogen and natural gas blend combustion products and estimates the amount of condensate and latent energy recovery from flue gas as a function of condensing temperature. The efficient energy recovery depends on network return temperature, and it is possible to overcome this limitation by implementation of heat pump for extraction of low temperature heat from flue gases. The case study considers operation of heat only boiler and flue gas condenser with integrated cascade of heat pumps, which consist of absorption lithium bromide-water chiller (in heat pump mode) and vapour compression unit. Presented results of energy recovery hence are limited by data collected from the natural gas combustion for district heating network energy supply. However, previous thermodynamic consideration allows extending the obtained results for case of hydrogen and natural gas blend combustion. A proof of concept of heat recovery by combination of flue gas condenser supported by a cascade of heat pumps demonstrates the efficiency in case of hydrogen and natural gas blend combustion.

Keywords: *Cascade utilization, condensation recovery, heat pumps, hydrogen, natural gas.*

1. INTRODUCTION

Green hydrogen presents a viable alternative to fossil fuel and ensures sustainable energy transition and decarbonization of many sectors of national economies. This can be achieved in line with improvement of air quality and expansion of energy storage options. Use of hydrogen in the energy sector has a long history, which begun with the first internal combustion engines over two centuries ago. Currently, it forms an integral part of the modern chemical and refining industry [1].

Hydrogen offers many very valuable features as a fuel; it is energy-dense when in its liquefied form, has a wide flammability range, and can be manufactured via a variety of ways. In some applications, it can be substituted in a relatively straightforward way as an alternative fuel, displacing natural gas, gasoline, kerosene and diesel in combustion applications [2]. Hydrogen has potential to fill certain energy supply requirements that may not be easily met using battery electric storage, for example, for gas boilers in the home, as a fuel for heavy-duty vehicles, off-road machinery, trains, back-up capacity for grid electrical supply and as a fuel for global shipping and aviation [3]. The preeminent argument in favour of the use of hydrogen as a fuel is that the major waste product formed from its use is water vapour.

In order to support further spread of hydrogen in different industries, more than thirty countries worldwide already have developed the national framework documents – strategies and roadmaps, for promotion of hydrogen as fuel and energy carrier. As for Europe, the European Hydrogen Backbone project initiates the creation of continent-wide hydrogen transportation and storage infrastructure [4].

The power systems of the Baltic States carry significant expansion potential in renewable energy sources (hereinafter – RES) based generation, and by 2050 they could generate a total of 21.34 tera-watt hour (hereinafter – TWh) of electricity from RES. This corresponds to 72 % of the total regional electricity consumption [5]. The mature technology of water electrolysis would allow for smooth integration of RES into green hydrogen production with a purpose to balance energy generation and consumption.

To replace hydrocarbons in electricity generation, the green hydrogen can be used instead, especially in power plants, which can operate in a cogeneration mode and provide both electricity and heating energy for district heating.

The fuel cell needs only pure hydrogen of high-grade quality for operation, what can be a certain limitation in current circumstances of limited green hydrogen availability. Combustion of hydrogen is less efficient than fuel cell conversion to electricity, but it significantly reduces requirements for quality of fuel and opens a way to extensive use of different gaseous fuel blends like one of the natural gas and hydrogen, biomethane and hydrogen, propane and hydrogen, etc.

The transition to blend of hydrogen and natural gas and/or biomethane would allow continuing exploitation of existing natural gas boilers and burners, not replacing them immediately with new ones. In addition, combustion of such blend would contribute to greenhouse gas (hereinafter – GHG) emission reduction targets by gradual decarbonization of the heat energy sector, which would be achieved just by an increase of hydrogen share in hydrogen and natural gas blend alone. With moder-

ate content of hydrogen (if less than 20 %), it allows for further use of existing natural gas storages, pipelines and other distribution system elements without fundamental investments and technical changes [6]–[8].

However, there are several concerns regarding wider use of hydrogen in low-carbon heating. First, hydrogen has low ignition energy and low density; therefore, it should be stored under high pressure. This can create explosion risks, plus small size of hydrogen molecules can ensure high capability to escape from storage tanks, pipes through all kind of joints. They can also penetrate through many hydrogen-non-resistant materials, causing embrittlement and creating the so-called hydrogen assisted cracking in various metals and their alloys [9].

Second, concerns would derive from potential health risks presented by increased nitrogen oxide (hereinafter – NO_x) emissions during combustion of hydrogen and natural gas blend in comparison with combustion of natural gas or biomethane. Experimental study of hydrogen and natural gas blend combustion demonstrates a minor increase of NO_x (only natural gas f=0) from 45 to 52 ppm for f=30 % [8]. Another research presents the following results: when hydrogen is added to natural gas by 25 %, 50 % and 75 %, the NO_x emission level increases by 92.81 %, 219.72 % and 360 % (485 ppm), respectively [10].

However, both factors of concern can be avoided by means of engineering solutions: correct materials selection and use of low NO_x burner.

Hydrogen combustion does not emit GHG, but origin of hydrogen or way it is produced can be a challenge for low-carbon heating. Steam Methane Reformation (hereinafter – SMR) currently provides the lowest cost of produced hydrogen, but this process releases significant amount of carbon dioxide (hereinafter – CO_2) into atmosphere. Also, due to limited efficiency of SMR, which is about 70 %, it is responsible for bigger CO_2 emission per unit of energy produced than natural gas combustion process. An alternative way to produce hydrogen – by means of water electrolysis and RES, still is more costly. Taking in account a need for RES energy storage and balancing, it might support introduction and wider use of hydrogen and natural gas blend.

Combustion product of hydrogen and natural gas blend will contain more water steam, when hydrogen share in fuel will grow. Efficient heat recovery from flue gases would be possible, if combustion products would be cooled down lower than dew point and water steam would condensate and release latent heat. If we condensate all water steam from flue gases, it would be possible to shift from a low heating value (hereinafter – LHV) to a high heating value (hereinafter – HHV) and save a significant amount of fuel consumed: from 10 % in case of natural gas, and up to 18 % in case of hydrogen (f=1). Return flow temperature in the heating system would be a limitation for efficient moisture condensation from flue gas. Application of heat pump for heat recovery from flue gas would open a way to overcome limitation of this kind. Operation of HOB with FGC and AHP (water steam fired chiller-heater) demonstrates an increase in natural gas combustion output from 70 by 6 megawatt (hereinafter – MW) (sensitive heat of flue gas recovery in FGC) plus 2 MW extracted by AHP (latent heat of moisture from fly gas) [11]. The share of AHP in heat recovery limited by 2/76 = 2.6% of total HOB power in the considered case study.

Nevertheless, there are many theoretical and practical studies on application of heat pumps and heat pump cascades with the purpose to extract more energy from

flue gas [12]–[14]. Issue of temperature lift is very significant for energy recovery potential increase, and the combination of absorption and compression heat pumps becomes relevant for hydrogen and natural gas blend combustion, since water steam condensing will get big share in energy balance. This paper presents a case study of the natural gas boiler, where already installed AHP with FGC with addition of vapour comparison pump is targeted to extract more sensitive heat from condensate of FGC. Available operational data allow performing estimation on heat recovery gain in case of shift from natural gas to hydrogen and natural gas blend.

2. METHODOLOGY

Chemical composition of hydrogen and natural gas blend and design of burner affect combustion product properties. The main parameters for combustion are hydrogen fraction f and amount of excess air λ. Suggested approach will follow [7] and reduce hydrogen and natural gas blend composition to methane-hydrogen blend, with a purpose to reveal how dew point temperature in combustion product depends on input parameters. The aim of this consideration is to establish relation between actual cooling (condensing) temperature and blend LHV.

2.1. Thermodynamic Preliminaries

The methane-hydrogen blend combustion can be represented by following chemical equation with an aim to establish mass and heat balance for reaction on base of kilomole

$$fH_2 + (1\text{-}f)CH_4 + \lambda(2-1.5f)(0_2+3.76N_2) \rightarrow \\ \rightarrow (1-f)CO_2 + (2-f)H_2O + 3{,}76\lambda(2-1.5f)N_2 + (\lambda-1)(2-1.5f)O_2. \quad (1)$$

Partial water pressure and respectively dew point temperature can be evaluated as

$$\frac{P_{H20}}{P} = \frac{2-f}{1-0.5f+9.52\lambda-7.14f\lambda}. \quad (2)$$

For a hydrogen and natural gas blend combustion product (dry) kmol number,

$$\mathrm{N_{mix}} = 0.5\mathrm{f} + 9.53\lambda - 7.14\mathrm{f}\lambda - 1. \quad (3)$$

Mass of dry combustion product in kg for one kmol of hydrogen and natural gas blend

$$m_{dc} = 4f + 274\lambda - 206\,\lambda f - 20. \quad (4)$$

Molecular mass of dry combustion product

$$M_{cp} = \frac{4f + 274\lambda - 206\,\lambda f - 20}{0.5f + 9.53\lambda - 7.14f\lambda - 1}. \quad (5)$$

For a humidity ratio of combustion product (kg of water steam per kg of dry combustion product), one can show that

$$d = \frac{P_{H20}}{(P-P_{H20})}\frac{M_{H20}}{M_{CP}} = \frac{1}{(\frac{P}{P_{H20}} - 1)}\frac{18}{\left(\frac{4f+274\lambda-206\,\lambda f-20}{0.5f+9.53\lambda-7.14f\lambda-1}\right)}. \quad (6)$$

Water steam amount in flue gas after combustion 1 kmol of hydrogen and natural gas blend

$$D = d \cdot m_{dc} = \frac{18(0.5f + 9.53\lambda - 7.14f\lambda - 1)}{\frac{P}{P_{H20}} - 1}. \quad (7)$$

However, amount of water steam in kg already known from chemical reaction

$$D = 18 \cdot (2 - f). \quad (8)$$

If flue gas is treated in condenser (cool down to temperature t, which is lower than dew point) and it becomes possible to calculate amount of condensate per kmol of hydrogen and natural gas blend

$$D_c = 18 \cdot (2 - f) - d \cdot m_{dc} = 18\left(2 - f - \frac{(0.5f + 9.53\lambda - 7.14f\lambda - 1)}{\frac{P}{P_{H20}} - 1}\right). \quad (9)$$

Water steam saturated pressure can be described by number of empirical equations: Antoine, Tetens, Arden Buck, Goff-Gratch equations etc. In the present paper we use Tetens formula as it is simple and accurate (in range of 10 C to 100 C deviation from table value is within 0.5 %):

$$P_{H20} = 0{,}0061078\exp\left(\frac{17.27t}{t + 237.3}\right), bar \quad (10)$$

whereupon Eq. (10) may be used in a reversed way

$$\frac{1}{\frac{P}{P_{H20}} - 1} = \frac{1}{P \cdot 163.72\, exp\left(-\frac{17.27t}{t + 237.3}\right) - 1}. \quad (11)$$

Hydrogen and natural gas blend LHV in kWh/ kmol of fuel (hydrogen LHV = 67.2 kWh/kmol):

$$Q_{HENG} = LHV_{NG}(1 - f) + 67.2f. \quad (12)$$

To express the ratio of released heat Q (combustion + water steam condensation) to LHW of hydrogen and natural gas blend as a function of flue gas cooling temperature t

$$\frac{Q}{Q_{HENG}} = 1 + \frac{18 \cdot L}{LHV_{NG}(1 - f) + 67.2f}\left(2 - f - \frac{0.5f + 9.53\lambda - 7.14f\lambda - 1}{P \cdot 163.72\, exp\left(-\frac{17.27t}{t + 237.3}\right) - 1}\right). \quad (13)$$

Taking into account that natural gas had no permanent composition, the present paper will consider hydrogen and natural gas blend as hydrogen / methane blends. The value of LHV for methane will be 222.8 kWh/kmol and value 0.69 kWh/kg will be used for latent heat L. This simplification will not reduce the value of obtained equation (12), (13), but allow yielding an alternative fitting function:

$$\frac{Q}{Q_{HENG}} = 1 + \frac{12.5}{222.8 - 155.6f}\left(2 - f - \frac{0.5f + 9.53\lambda\ - 7.14f\lambda - 1}{P \cdot 163.72\, exp\left(-\frac{17.27t}{t + 237.3}\right) - 1}\right), \qquad (14)$$

where P is total pressure of gas blend in bar.

2.2. Performance Comparison

The presented thermodynamic consideration is based on gas blend description and involves empirical equation for saturation temperature definition. Obtained equations allow finding an answer how f blend composition and λ amount of excess air influence dew point temperature. Numerical consideration presented in Fig. 1 and Fig. 2 is performed for hydrogen-methane blend. However, derived equation can be used to calculate properties for hydrogen and natural gas blend by implementation of the natural gas composition.

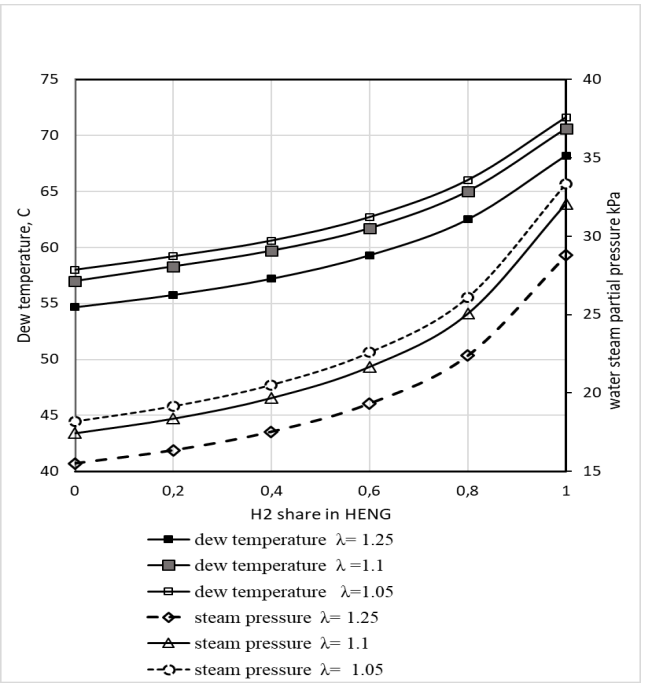

Fig. 1. Dew temperature and water steam saturated pressure vs methane-hydrogen blend composition.

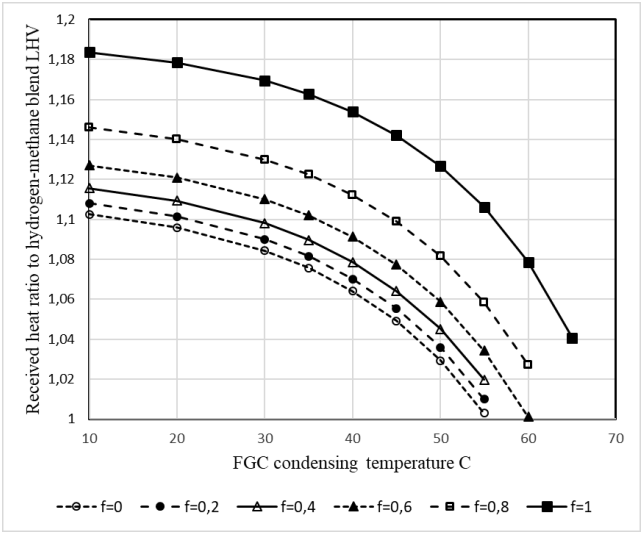

Fig. 2. Received heat ratio to methane-hydrogen blend LHW for different composition f and various condensing temperature t (when λ=1.2).

Figure 1 presents saturation pressure of water steam for various f and λ in range of 1.05 to 1.25 according to Eq. (2), then corresponding value of saturation temperature is obtained from steam-table and is designated as dew point temperature. The dew point temperature increases with f growing, so, when hydrogen and natural gas blend has larger share of hydrogen, dew point can be up to 65 to 72 ^{0}C depending on λ. When λ increases, the value of saturation pressure and dew point decrease. This value can be important for FGC design in case of hydrogen and natural gas blend with a different hydrogen share.

Moisture condensation from flue gas can provide heat recovery and increase energy output, but still HOB efficiency is a function of many design parameters like insulation, air temperature etc. Consideration presented in Eq. (14) was limited by t – cooling temperature, f – composition of blend and λ. Results of calculation presented in Fig. 2 and obtained for λ=1.2 demonstrate that cooling temperature t=55 ^{0}C for pure methane (f=0) will produce no recovery, because the temperature is around dew point and condensation is not possible, but for f=1 (pure hydrogen) energy recovery will be around 10 %.

This can serve as evidence that flue gas condensation from combustion product of hydrogen and natural gas blend with high hydrogen amount will be less sensitive to t2 network return temperature. However, Fig. 2 reveals that, if cooling temperature in FGC is as low as 20 ^{0}C (much less than T2) heat recovery will increase from 9 % (f=0) to 18 % (f=1).

Additionally, it is possible to investigate influence of λ on heat recovery output. The analysis represented in Fig. 2 indicates that flue gas condensation at lower temperature will significantly increase amount of heat recovery. Developed equations (1)–(14) suggested for purpose to estimate the desired level of t temperature of condensation since it would be lower than T2. Decrease of t would require more energy input in the already discussed heat pump with different driving energy (thermal for absorption and electrical for compression type of units).

Application of low temperature lift heat

pumps would enhance heat recovery and definitely decrease fuel consumption, but it is important to look at total energy balance. Therefore, all considerations presented before should be reinforced by real life operation results, viewed from total energy efficiency standpoint. At the moment, hydrogen and natural gas blend is not yet a common fuel, and it is good chance to foresee performance of FGC supported by various combinations of heat pumps.

3. CASE STUDY

The performance of natural gas fired HOB boiler (rated power 100 MW) equipped with flue gas condenser and additional cascade of heat pumps is considered with purpose to estimate moisture condensation from flue gas in real operational condition. The performance data are available only for natural gas combustion, but since previous consideration it will be possible to collect data of heat recovery estimation when it will be hydrogen and natural gas blend combustion.

3.1. Experimental Setup

The considered HOB supply water flowed in heating network at temperature T1, the return flow from network had temperature T2. The value of T1 followed ambient temperature for outside weather (in range of 10 to -15 ^{0}C) direct temperature was around 100 ^{0}C (outside -15 ^{0}C), when outside temperature became around zero, direct temperature decreased toT1= 70 ^{0}C. The network return temperature T2 had corresponding range from 50 ^{0}C to 40 ^{0}C.

Water flow from return line had temperature T2 and this was sufficient to cool down flue gas from boiler TF1 =140 ^{0}C.

However, in fact it is difficult to ensure efficient moisture condensation from flue gas without AHP. Temperature difference between flue gas flow and water in FGC can be at least 10–15 ^{0}C and more; therefore, flue gas is left with temperature above dew point (Fig. 2). The retrofit target of available FGC was to decrease temperature in flue gas: by circulation loop 6 was connected to AHP evaporator E. This ensured deeper heat recovery from flue gas: temperature after E was around 20 ^{0}C and it grew in FGC up to 35 ^{0}C (left FGC and enter to E), thus decreasing flue gas temperature after FGC to 40–45 ^{0}C, which was not possible without application of AHP. The experiment was performed for HOB power output range from 30 to 70 MW (depending from network energy demand). Amount of condensate from FGC was limited to 3–4 m^3/h and did not grow proportionally of HOB power output. It seems that during FGC retrofit additional loop 6 faced limited contact surface with flue gas and this was a shortcoming for efficient moisture condensation from combustion product. AHP (water-fired chiller-heater direct line from HOB at 130 ^{0}C) generator G took about 2.5 MW to lift return temperature of network from T2 =40 ^{0}C up to 54–55 ^{0}C accounted as 4 MW (obtained in absorber A and condenser C).

As a result, the operation of HOB at 40 MW accounted the following: the consumption of G about 2.5 MW (hot water from HOB) was complemented by 2 MW from E by latent heat of fly gas moisture condensation (liquid about 3 m^3/h) obtained in cooling loop 6 (additional condensing part in FGC). Furthermore, the AHP performance reached COP = (2+2.5)/2.5 = 1.8 that was according

to data sheet of AHP. Since the condensate after FGC had temperature TC1 = 45 ^{0}C and was equal to flue gas TF2, it was not possible to recover this energy by warming of return flow from network. Therefore, implementation of vapour compression heat pump allowed performing condensate sensitive heat recovery.

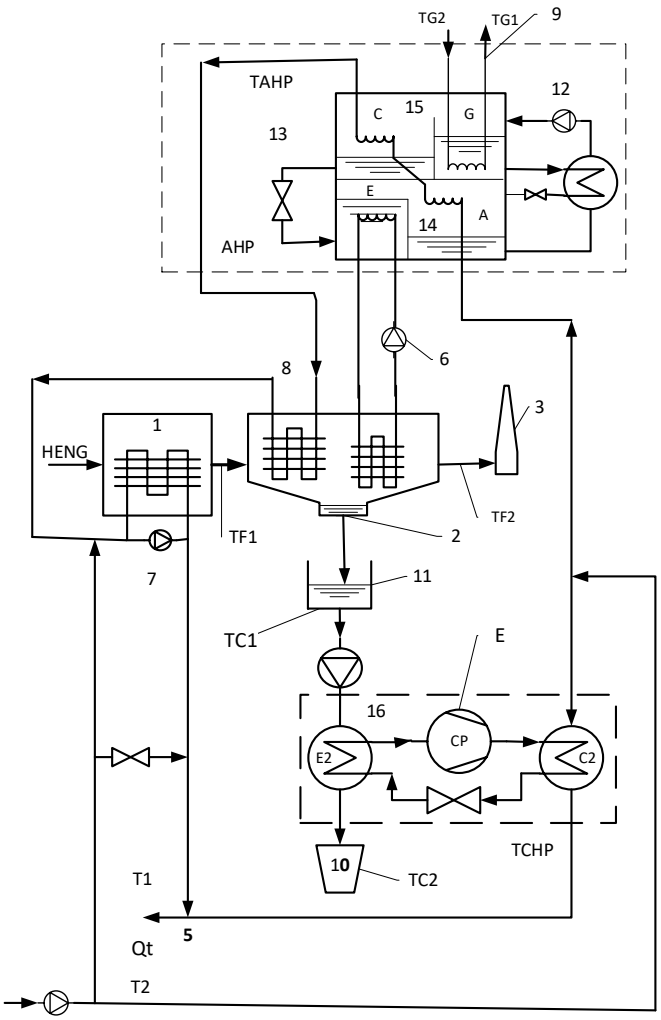

Fig. 3. Absorption and vapour compression heat pumps with flue gas condenser operation for energy recovery: 1 – Heat only boiler (HOB), 2 – flue gas condenser (FGC), 3 – chimney, 4 – network circulation pump, return water from district heating network (DHN), 5 – direct water to DHN, 6 – flue gas energy condensing loop for AHP evaporator (E), 7 – HOB recirculation pump, 8 – flue gas energy loop, 9 – hot water flow for generator of AHP, 10 – drain of flue gas condensate, 11 – condensate tank after FGC, 12 – weak solution circulation pump, 13 – absorption heat pump (AHP) , 14 – evaporator (E) and absorber (A), 15 – condenser (C) and generator (G), 16 – vapour compression heat pump, E2 evaporator (low pressure), CP refrigerant compressor VFD and C2 high pressure condenser, T1 – direct and T2 – return DHN temperature, TG1 and TG2 – generator direct and return, TC1 and TC2 condensate temperature after first and second peat pumps step. TF1 and Tf2 – fly gas temperature after boiler and fly gas condenser. TCHP – temperature after compression heat pump. EL – electrical energy consumption from compression heat pump drive.

The HOB fly gas condensate in amount of 3.5 m^3/h cooling from given TC1 to TC2=15 ^0C (flow through evaporator of CHP) produces recovery of 116 kW. The COP= 3.9 requests El=40 kW electrical power consumption by CHP compressor. In this case, return water obtained about 156 kW (40+116) and left condenser of CHP at 55 ^0C.

Based on these results, it has been shown that the fly gas heat recovery (moisture condensation) can provide about 5 % surplus energy by AHP application and CHP by condensate cooling can return additional 0.28 % to HOB power.

3.2. Experimental Findings and Discussion

This paper deals with investigation of practical way how to get more from fuel LHV by moving toward to HHV, which becomes possible only in case of full moisture condensation. Implementation of condensing gas boiler for domestic heat supply demonstrates high performance due to reason that return heating water temperature in a well-insulated house can be 30 ^0C and even lower. However, there is still in operation a large centralized heat network and issue of its decarbonization becomes acute. The return temperature in such a network is hardly possible to drop to the desired level. The motion toward fuel decarbonization includes hydrogen and natural gas blend introduction and this will increase potential for energy recovery by moisture latent heat return in the network.

The experimental set operation demonstrates that HOB follows network demand and flue gas flow rate will increase when outside temperature drops, but return temperature from network increases. This is counterforce to complete recovery of moisture latent heat. The application of heat pump provides an option to break direct influence of return water temperature on heat recovery.

The result of HOB recovery reveals that only part of all moisture can condensate in FGC. It is important to understand full recovery potential by accounting all water steam in flue gas in kg per kWh of combusted hydrogen and natural gas blend for single kmol of fuel:

$$N_{H20} = \frac{18(2-f)}{222.8-155.6f}, \frac{kg}{kWh}/kmol. \quad (15)$$

The equation gives water condensate 6.46 t/h for combustion of 40 MW (by LHV) natural gas like it was in the experimental test. If we make shift to hydrogen and natural gas blend with f = 0.5 for this power output of moisture becomes 7.5 t/h, but for pure hydrogen f=1 moisture will account to 10.8 t/h.

The whole available moisture in flue gas is possible to use for energy recovery, if temperature gradient between cooling loop and flue gas is abated. Therefore, sizing of cooling loop for FGC design had to be considered for efficient condensation with sufficient output in the whole range of HOB operation.

Finding of brake even point for energy injection in heat pumps to increase recovery extraction is beyond the specified scope of the paper, which is aimed exclusively at hydrogen and natural gas blend properties and FGC parameters in theoretical and practical applications.

4. CONCLUSIONS

Thermodynamic consideration described in the paper leads to two important findings, namely, how:

- hydrogen and natural gas blend composition would influence dew point, and
- to estimate condensate and heat recovery for various hydrogen and natural gas blends by temperature of condensation.

Along with hydrogen share in hydrogen and natural gas blend, air excess rate was involved in theoretical consideration. Therefore, the obtained relationship can be adapted for real combustion/condensation systems description taking into account real fuel composition and available range of air mixing rate.

The experimental setup data prove the concept of recovery enlargement by implementation of temperature lift in heat pump connected to a condensing device. Numerical comparison shows good compatibility of derived equation and actual condensate flow for the obtained heat recovery.

The practical value of the presented study consists in HOB and FGC operation inside outlook that reveals a weak point in the design of FGC. Limited surface of fly gas condenser halved available recovery for HOB operation on 40 % from rated output. Further increase of HOB power was not supported by recovery power grow. Thus, capacity of AHP should be balanced by ability of FGC to ensure condensation at accepted temperature gradient.

ACKNOWLEDGEMENT

This research was funded by the Latvian Science Council's fundamental and applied research programme project "Development of Model for Implementation of Sustainable and Environmentally Friendly Last-Mile Distribution Transportation Services in Latvia" (TRANS4ECO), project No. lzp-2022/1-0306, 01.01.2023.- 31.12.2025.

REFERENCES

1. Jansons, L., Zemite, L., Zeltins, N., Geipele, I., & Backurs, A. (2023). Green and Sustainable Hydrogen in Emerging European Smart Energy Framework. *Latvian Journal of Physics and Technical Sciences*, 60 (1), 24–39. DOI: 10.2478/lpts-2023-0003
2. U.S. Department of Energy. (1994). *Alternatives to Traditional Transportation Fuels: An Overview, DOE/EIA-0585/O*. Energy Information Administration. Available at https://www.eia.gov/renewable/alternativefuels/0585942.pdf.
3. Bloomberg. (2020). *Hydrogen Economy Outlook: Key Messages.* Available at https://data.bloomberglp.com/professional/sites/24/BNEF- Hydrogen-Economy-Outlook-Key-Messages-30-Mar-2020.pdf, 2020.
4. Jansons, L., Zemite, L., Zeltins, N., Bode, I., Geipele, I., & Kiesners, K. (2022). The green hydrogen and the EU gaseous diversification risks. *Latvian Journal of Physics and Technical Sciences*, 59 (4), 53–70. https://doi.org/10.2478/lpts-2022-0033
5. Petrichenko, L., Petrichenko, R., Sauhats, A., Baltputnis, K., & Broka, Z. (2021). Modelling the Future of the Baltic Energy Systems: A Green Scenario. *Latvian Journal of Physics and Technical Sciences*, 58 (3), 47–65. DOI: 10.2478/lpts-2021-0016

6. Deng, Y., Dewil, R., Appels, L., Tulden, F.V., Li, S., Yang, M., & Baeyens J. (2022). Hydrogen-Enriched Natural Gas in a Decarbonization Perspective. *Fuel* 2022, 26.
7. Schiro, F., Stoppato, A., & Benato, A. (2020). Modelling and Analyzing the Impact of Hydrogen Enriched Natural Gas on Domestic Gas Boilers in a Decarbonization Perspective. *Carbon Resources Conversion* 2020, *3*, 122–129. https://doi.org/10.1016/j.crcon.2020.08.001
8. Bing, G., Yongbin, J., Zilai, Z., Shusheng, Z., Yinshen, T., Hai ,Y., … & Dongfang Z. (2019). Experiment Study on the Combustion Performance of Hydrogen-Enriched Natural Gas in a DLE Burner. *International Journal of Hydrogen Energy, 44* (26), 14023–14031. https://doi.org/10.1016/j.ijhydene.2019.03.257.
9. Jansons, L., Zemite, L., Bode, I., & Zeltins, N. (2022). The Potential of the Hydrogen Underground Storages: their Types, Development Chellanges and the Latvian Situation. *Proceeding of 2022 IEEE 63rd International Scientific Conference on Power and Electrical Engineering of Riga Technical University (RTUCON),* DOI: 10.1109/RTUCON56726.2022.9978776
10. Cellek, M.S., & Pınarbaşı, A. (2018). Investigations on Performance and Emission Characteristics of an Industrial Low Swirl Burner while Burning Natural Gas, Methane, Hydrogen-Enriched Natural Gas and Hydrogen as Fuels. *International Journal of Hydrogen Energy*, *43* (2), 1194–1207, https://doi.org/10.1016/j.ijhydene.2017.05.107.
11. Rusovs, D., & Žentiņš, V. (2020). Steam Driven Absorption Heat Pump and Flue Gas Condenser Applied for Heat Recovery in District Heating Network. In: *19th International Scientific Conference on Engineering for Rural Development: Proceedings, 19*, (pp. 1627–1632). ISSN 1691-5976: doi:10.22616/ERDev.2020.19.TF418
12. Zajacs, A., Bogdanovics, R., & Borodinecs, A. (2020). Analysis of low temperature lift heat pump Application in a District Heating System for Flue Gas Condenser Efficiency Improvement. *Sustainable Cities and Society*, *57*, 102130. https://doi.org/10.1016/j.scs.2020.102130
13. Gao, J.T., Xu, Z.Y., & Wang, R.Z. (2021). Enlarged Temperature Lift of Hybrid Compression-Absorption Heat Transformer via Deep Thermal Coupling. *Energy Conversion and Management*, *234*, 113954.
14. Wang, X., Zhang, H., & Dong, Y. (2022). Simulation Study of an Open Compression Absorption Heat Pump in Water and Heat Recovery of Low-Temperature and High-Humidity Flue Gas. *Energy Conversion and Management, 2022*, 269. DOI:10.1016/j.enconman.2022.116180

sciendo

LATVIAN JOURNAL OF PHYSICS
AND TECHNICAL SCIENCES
2023, N 2

DOI: 10.2478/lpts-2023-0010

THE PREDICITION OF SOLAR FLARES USING MILLIMETER RADIO BRIGHTENINGS

J. Kallunki

Aalto University, Metsähovi Radio Observatory, FINLAND
Metropolia University of Applied Science, FINLAND
E-mail: juha.kallunki@metropolia.fi

Solar activity could have significant impacts on various Earth and near-Earth space systems, such as satellite communication and power grid systems. The prediction of solar activity and active solar events plays a major role when preparing for these disturbances. Various satellite-based instruments constantly observe the Sun. However, only a few ground-based solar instruments could provide versatile enough information for the space weather prediction. Metsähovi Radio Observatory of Aalto University (Finland) has a unique collection of millimetre (8 mm) solar radio maps over the past 40 years, and even denser observational solar radio data catalogue since 2011. About 75–80 % days yearly are covered nowadays. This gives opportunity to make statistical estimation of solar flare occurrence based on solar radio maps. In this study, we had 2253 days when both solar radio map and GOES (Geostationary Operational Environmental Satellites) classified solar flare were observed. In this work, we used solar flare classification done by the Space Weather Centre (SWC) of the National Oceanic and Atmospheric Administration (NOAA). The data were observed between 1 January 2011 and 12 September 2022. Our study shows that the maximum intensity of radio brightenings is a good indicator to tell which kind of GOES classified solar flare could be expected to happen. The article presents that intense radio brightening is needed to produce a certain GOES classified solar flare.

Keywords: *Radio brightening, solar flares, solar radio astronomy, space weather, space weather prediction.*

1. INTRODUCTION

The solar flares are classified by their intensity. Solar flares are further classified to five classes using the letters A, B, C, M and X depending on their X-ray peak flux in the wavelength range from 0.1 to 0.8 nm. A class is the weakest, and its flux level starts at 10^{-8} W/m^2. X-class solar flare flux level starts at 10^{-4} W/m^2, respectively. In addition, the strength of an event within a class is noted by a numerical suffix, e.g., M1.0 and M2.0. This means that M2.0 flare is twice the strength of an M1.0 flare. M- and X-class flares are capable to produce strong electromagnetic emissions [1]. It has been reported that M- and X-class flares could cause various disturbances, e.g., to the Global Positioning System (GPS) or Global Navigation Satellite Systems (GNSS) [2], [3]. Some powerful X-class flares are classified as extreme space weather events. CMEs (Coronal Mass Ejection) could also cause significant negative impacts: power grid failures to spacecraft and satellites [4].

The prediction of the solar flare has been continuous research topic in the fields of solar physics and space weather. However, a majority of these prediction and analysis methods use data from a satellite, mainly from SDO (Solar Dynamics Observatory) [5], [6]. Ground-based observing systems could extend and secure prediction capabilities. The main disadvantage on a ground-based system is that they can operate from the sunrise to sunset, and continuous solar monitoring capability cannot be achieved only with a single instrument. Besides, optical solar monitoring cannot be made if atmospheric conditions are not favourable. On the other hand, observations on radio wavelengths (from metre to millimetre wavelengths) are not so critical for the prevailing weather conditions. Several radio telescopes are not purely dedicated to solar observations, e.g., [7] and observational data are then limited. The connection between solar millimetre and X-ray emission has been studied earlier. It has been shown that their peak intensities follow similar trends [8]. In addition, the connection between solar millimetre emission and CME has been studied earlier [9].

The article aims at demonstrating more careful connection between GOES X-ray events and millimetre radio brightenings. Is it possible to use information from radio brightening intensity to predict solar flare occurrence and type (A, B, C M or X)? How strong solar flare could be expected on the basis of radio observations? We will use 8 millimetre solar data from Metsähovi Radio Observatory of Aalto University for the analysis between 1 January 2021 and 12 September 2022. The solar radio data are raster scans maps from the solar disk. The observing period covers a full solar cycle (11 years), which is reasonable time to make a statistical conclusion about the relationship between radio brightenings and GOES classified solar flares, for example, how intense radio brightening is needed for M-class solar flare. We could call our approach a probabilistic forecasting method, referring to earlier study [10]. In addition, we are willing to keep our model simple, using only one parameter (radio brightness intensity).

2. INSTRUMENTATION

The RT-14 at Metsähovi Radio Observatory (MRO) of Aalto University, Finland (Helsinki region; E 24:23.35, N 60:13.04) is a Cassegrain type antenna with a diameter of 13.7 m. The usable wavelength range of the telescope is 13.0 cm–2.0 mm. In this study, we only used wavelength at 8 mm. During solar observations the antenna can be used for solar mapping, partial solar mapping, and tracking of any selected areas on the solar disk. We used only solar raster maps in this study. In Fig. 1, a millimetre raster scan map is shown as an example. The beam size of the telescope is 2.4 arc min at 8 mm. The receivers are Dicke-type radiometers. The noise temperature of the 8 mm receiver is approximately 280 K. It takes approximately 125 seconds to make one solar radio map, or even faster in 65 seconds with a slight low quality. The observational data are recorded in intensities. Because the measurements are always scaled relative to the QSL, the observations are comparable over the years. The brightness temperature of the QSL at 8 mm is 8100 K ± 300 K. The solar emission at 8 mm comes from the chromosphere [11].

The soft X-ray data were received from GOES (Geostationary Operational Environmental Satellites) on two different channels: 0.5–4 Å (XS) and 1–8 Å (XL). For GOES class solar flare classification, only the XL wavelength regime is used. The data were captured at 0.5 Hz sampling. The soft X-ray emission of solar flares comes mainly from the bright coronal loops at the highest temperatures normally achieved in the flare process. Used channels respond to temperatures above 4 MK. The soft X-ray emissions of solar flares come mainly from the coronal loops at the highest temperatures normally achieved in the flare process. GOES satellites have been measuring solar soft X-ray irradiance since 1975 with their X-ray sensor (XRS) [12]. The Space Weather Centre (SWC) of the National Oceanic and Atmospheric Administration (NOAA) provides almost real-time (with 30 minutes delay) list of detected solar flares and other solar activity events, e.g., CME. Solar and Geophysical Event Reports could be found at https://www.swpc.noaa.gov/products/solar-and-geophysical-event-reports. NOAA provides both solar flare class and event peak flux. We used this information in our study.

3. OBSERVATIONS

Our observing period starts on 1 January 2011 and ends on 12 September 2022. This covers totally 4272 days. During this period, we had totally 3122 days (73 % of days) when solar radio maps were observed, and there were 869 days (among 3122 days) when classified GOES solar flares were not detected, so there were 2253 days when we had both solar radio maps and GOES classified solar flares. In Table 1, more specific division of observed GOES solar flares is presented. The strongest GOES solar flare from each day was selected for the analysis. There were days when more than 20 GOES classified solar flares were observed. The most common GOES flare is C-class. Approximately 300 solar radio maps were observed on some days. However, there

were also days when only one or two maps were observed. From each radio map, the maximum intensity value was defined. We defined for each day one representative maximum brightness intensity (temperature), $I_{daily,max}$, using Eq. (1):

$$I_{daily,max} = med\{I_{max,1} \dots I_{max,n}\}, \quad (1)$$

where $I_{i,max}$ is the maximum intensity of a single solar radio map and n is a number of daily observed solar radio maps. Equation (1) removes very high peak intensities; thus, $I_{daily,max}$ gives a stable maximum intensity value for each day, which is removing the fact that number of observed radio maps is varying remarkably. This method also removes bad quality observations.

As an example, on 12 August 2022, 21 GOES classified solar events were reported. 17 of those events were classified as C-class and four of them as B-class, respectively. The strongest event was classified as C6.8 category, which was already an intense C-class flare. 20 of these flares came from the active region (AR) 13079, including the strongest C6.8 flare. The defined daily (average) maximum brightness intensity was 111.3 % (to QSL) on 12 August 2022. On 13 August 2022, eleven solar radio maps were observed. The most intense radio brightening matched with a location of active region 13079. In Fig. 1, this radio brightening (AR13079) is marked with a red arrow. There are also two other weaker radio brightenings, and one of them produced one weak (<C2.0) GOES classified solar flare.

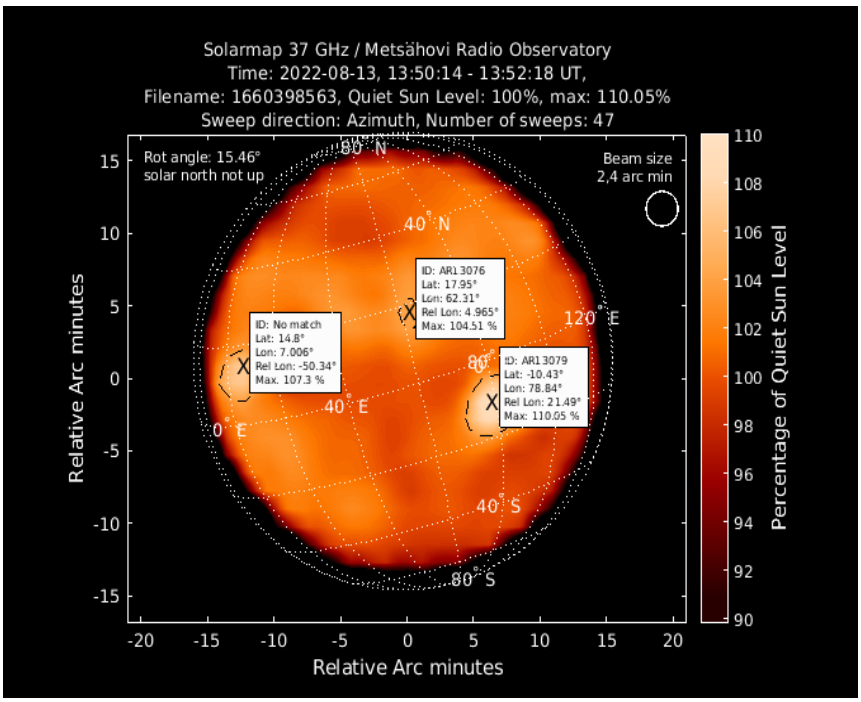

Fig. 1. Millimetre (8 mm) solar radio map observed on 13 August 2022. The radio brightening (in the southern hemisphere, AR13079, which is marked in a red arrow) is an origin of classified C6.8 class GOES flare.

Table 1. The Division of Detected GOES Classified Solar Flares

GOES solar flare class	Number of events
A	64
B	833
C	1033
M	288
X	35
Total	**2253**

Figure 2 shows the correlation between 8 mm radio brightness and X-ray flux (1–8 Å) intensity maxima. This relationship has a similar trend, which was reported in the earlier investigation [9].

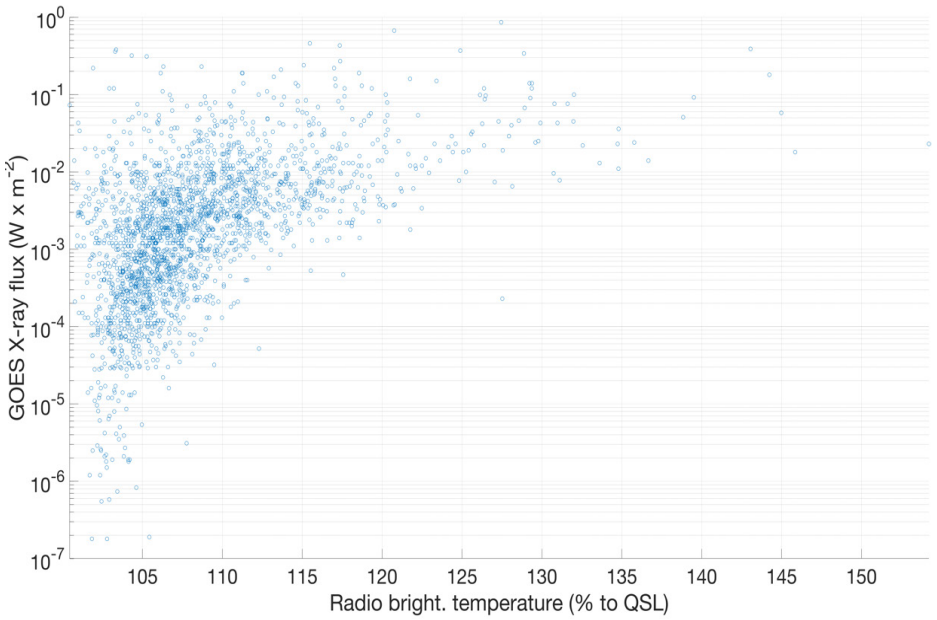

Fig. 2. Correlation between 8 mm radio brightness and X-ray flux (1–8 Å) intensity maxima.

4. RESULTS

We created a histogram plot for each GOES solar class flares. It shows how intense radio brightening is needed to cause certain GOES classified solar flare (A, B, C, M or X). Then we made a distribution (normal distribution) fit for histograms. Figure 3 illustrates histograms with a normal distribution fit in each GOES solar flare class (A, B, C, M and X).

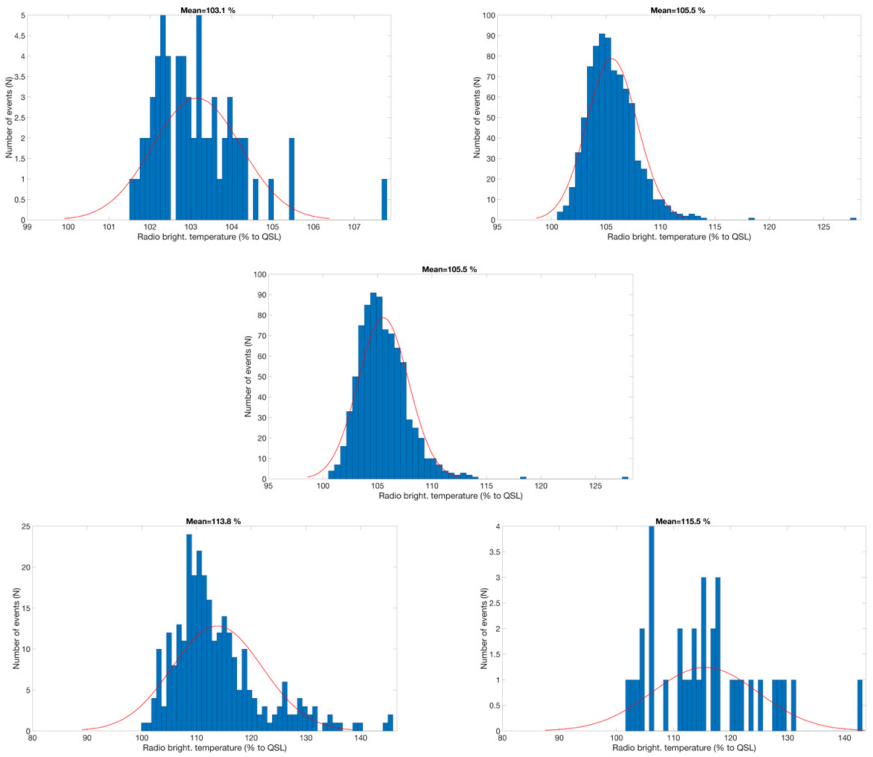

Fig. 3. Histograms with a normal distribution fit. Upper row: A- and B-classes, middle row: C-class and lower row M- and X-classes.

The plots show that weaker (A, B and C) flares are formed from radio brightenings, the intensity of which does not vary significantly. There is a larger variation in radio brightenings, which form M- and X-class flares. We also analysed days when GOES flares were not detected. Figure 4 shows a histogram with a normal distribution fit, which demonstrates that radio brightenings, which are more intense than 105 %, do not generally produce GOES classified solar flares. Only in some cases, a solar flare will not happen. On days (totally 869) when GOES classified solar flares were not classified, there were only 38 days when radio brightening intensity reached 107 %. There were 1160 days when radio brightening intensity reached 107 %. Based on our dataset, we conclude that if the radio brightening intensity reaches 107 %, GOES solar class flare will also occur at the probability of 96.7 %.

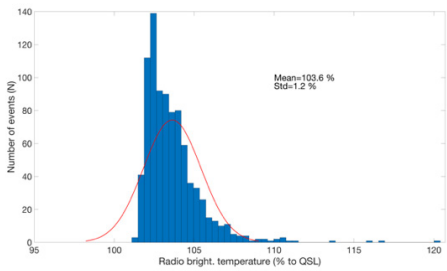

Fig. 4. Histograms with a normal distribution fit are shown from days when GOES flares were not detected.

Figure 5 illustrates a relationship between different GOES classified solar flares and radio brightening. The red dot presents an average value and an error bar (blue line) shows the 50 % probability interval. If the intensity of radio brightening is below 104 %, either we cannot see any GOES classified solar flares or we will see weak A-class flare. The radio brightening with the intensity between 104 % and 107 % means that a majority of events are B-class flares and it is also possible to detect weak C-class flares. There are mainly C-class flares when the maximum intensity of radio brightenings varies between 107 % and 110 %. At the interval between 110 % and 113 %, it is possible to observe either C-, M-, or X-class flares. If the brightness intensity is above 113 %, only M- and X-class flares could be detected. If the intensity is above 120 %, X-flares could be expected. A final conclusion about X-class solar flare relation to radio brightening cannot be made, since we have limited number (35) of X-class flares and, also A-class flares (64). To improve statistics, more of these events are needed. Other parameters, which could be included in the analysis, are information about the solar cycle phase and radio brightening location. However, our dataset covers only one solar cycle, part of Solar Cycles 24 and 25. This is not a long enough period for such an analysis.

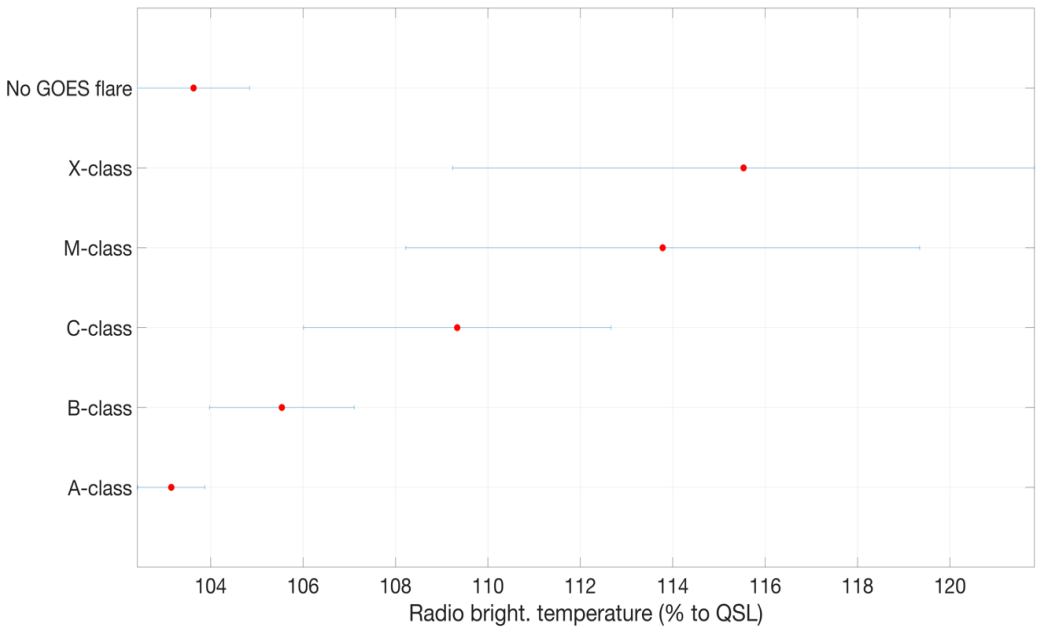

Fig. 5. Summary of GOES solar flare appearances versus daily maximum radio brightness temperature. The error bars describe 50 % probability interval.

Figure 6 presents the variation of radio brightenings on the day before GOES classified flares. It has the same trend as in Fig. 5. The difference is that variation (blue lines in Fig. 6) of radio brightenings is larger. Thus, it is even possible to make preliminary prediction based on the intensity of radio brightening from the day before the GOES flare appears.

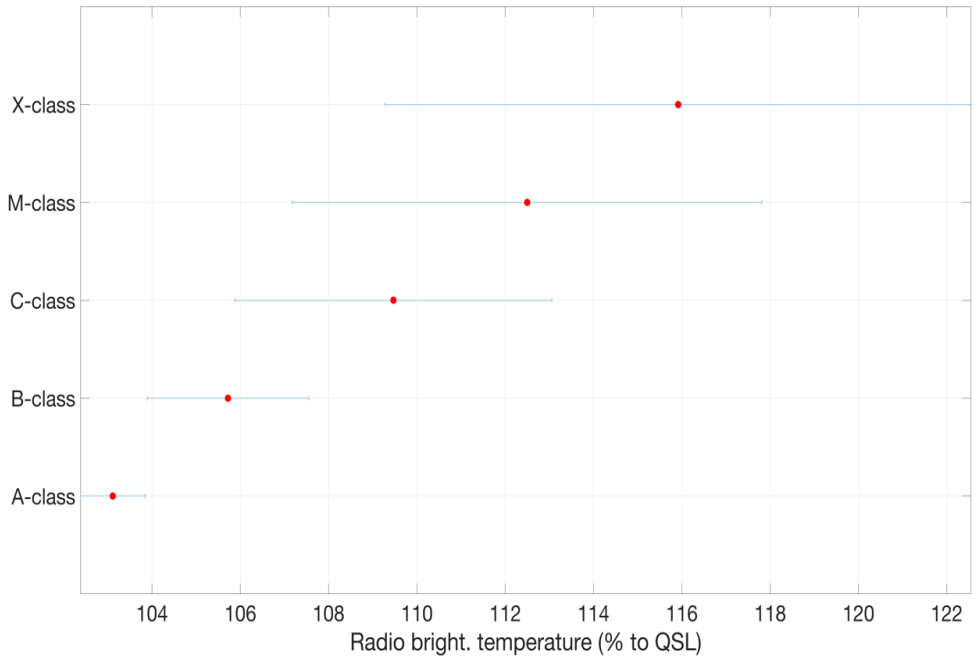

Fig. 6. Summary of GOES solar flare appearances versus daily maximum radio brightness temperature a day before. The error bars describe 50 % probability interval.

We have shown that radio brightenings are a good indicator to tell which kind of solar activity (GOES solar flares) we can expect. Even one or two solar radio maps each day could give a necessary information about expected, upcoming solar activity. This emphasises the importance of daily solar radio observations and the importance of ground-based observations. Only heavy rain and snowing prevent solar observations on millimetre wavelengths. Even more important aspect is that space weather prediction can also be made on the ground-based observations.

The modern society is more reliant on communication systems, which are vulnerable to space weather related phenomena. This is a major contributor for various space weather prediction models. Our analysis extends these prediction capabilities. As far as we know, this is one of the first space weather prediction analyses, which is based on millimetre wavelength observations.

REFERENCES

1. Grodji, O.D.F., Doumbia, V., Amaechi, P.O., Amory-Mazaudier, C., N'guessan, K., Diaby, K.A.A., … & Boka, K. (2022). A Study of Solar Flare Effects on the Geomagnetic Field Components during Solar Cycles 23 and 24. *Atmosphere 2022, 13* (1), 69. 10.3390/atmos13010069. hal-03597264

2. Yasyukevich, Y., Astafyeva, E., Padokhin, A., Ivanova, V., Syrovatskii, S., & Podlesnyi, A. (2018). The 6 September 2017 X-Class Solar Flares and Their Impacts on the Ionosphere, GNSS, and HF Radio Wave Propagation. *Space Weather, 16*, 1013–1027. https://doi.org/10.1029/2018SW001932

3. Liu, J. Y., Lin, C. H., Tsai, H. F., & Liou, Y. A. (2004). Ionospheric Solar Flare Effects Monitored by the Ground-Based GPS Receivers: Theory and Observation. *J. Geophys. Res., 109*, A01307, doi:10.1029/2003JA009931.
4. Deshmukh, V., Berger, T., Meiss, J., & Bradley, E. (2020). Shape-based Feature Engineering for Solar Flare Prediction. *arXiv* e-prints.
5. Sun, Z. (2022). Predicting Solar Flares Using CNN and LSTM on Two Solar Cycles of Active Region Data. *The Astrophysical Journal, 931* (2). doi:10.3847/1538-4357/ac64a6.
6. Deshmukh, V., Berger, T., Meiss, J., & Bradley, E. (2020). Shape-based Feature Engineering for Solar Flare Prediction. *arXiv* e-printsp.
7. Kallunki, J. (2018). Forty Years of Solar Radio Observations at Metsähovi Radio Observatory. *Astronomische Nachrichten, 339* (204), 204–211. doi:10.1002/asna.201813464.
8. Kallunki, J., & Tornikoski, M. (2022). Relationship between Solar Millimeter and Soft X-Ray Emissions. *Latvian Journal of Physics and Technical Sciences, 59*, 39–47. doi:10.2478/lpts-2022-0023.
9. Kallunki, J. (2022). Solar Microwave Emission Associated with Coronal Mass Ejections (CME). *Latvian Journal of Physics and Technical Sciences, 59* (1), 13–20. doi:10.2478/lpts-2022-0002.
10. Barnes, G., Leka, K. D., Schumer, E. A., & Della-Rose, D. J. (2007). Probabilistic Forecasting of Solar Flares from Vector Magnetogram Data. *Space Weather, 5* (9). doi:10.1029/2007SW000317.
11. Kallunki, J., & Tornikoski, M. (2018). Measurements of the Quiet-Sun Level Brightness Temperature at 8 mm. *Solar Physics, 293* (11). doi:10.1007/s11207-018-1380-8.
12. Hanser, F.A., & Sellers, F.B. (1996). Design and Calibration of the GOES-8 Solar X-ray Sensor: The XRS. *GOES-8 and Beyond, 2812*, 344. doi:10.1117/12.254082.

sciendo

LATVIAN JOURNAL OF PHYSICS
AND TECHNICAL SCIENCES
2023, N 2

DOI: 10.2478/lpts-2023-0011

RADIO MEASUREMENTS OF CORONAL MAGNETIC FIELDS IN FAN-SPINE CONFIGURATIONS ON THE SUN

B. Ryabov*, A. Vrublevskis

Engineering Research Institute
"Ventspils International Radio Astronomy Centre",
Ventspils University of Applied Sciences,
101 Inzeniera Str., Ventspils LV-3601, LATVIA
*e-mail: borissr@venta.lv

Recent interest of solar physicists in the analysis of the coronal mass ejections and circular solar flares in fan-spine magnetic configurations (FSCs) necessitates measurements of the corresponding coronal magnetic fields. A dominant sunspot with the circumjacent magnetic flux of opposite polarity produces a specific coronal region of the quasi-transverse (QT-) propagation of microwaves. We make use of the theory of QT-propagation to evaluate the strengths of coronal magnetic fields in the active regions NOAA 11579, 12242, and 12488 while they are non-flaring. Microwave polarization changes were observed with the RATAN-600 radio telescope, the Siberian Solar Radio Telescope, and the Nobeyama Radioheliograph. Changes in the sign of circular radio polarization provide the strengths of coronal fields in a QT-region if the coronal plasma density N_e and the length scale of magnetic field divergence L_d are known. We evaluate the length scale by means of the potential-field source-surface (PFSS) model and the coronal density from the Gaussian inversion of the differential emission measure (from the Solar Dynamics Observatory observational data), obtaining $N_e L_d = (0.46–0.64)\times10^{10}$ m^{-2}. The resulting coronal fields of 1.4×10^{-3} T and 2.34×10^{-3} T are attributed to the heights of 100 Mm and 50.2 Mm. We discuss the validity and consistency of the involved values to draw conclusions on the feasibility of coronal radio magnetography of FSCs.

Keywords*: Solar magnetic field, solar microwave observations, Sun, sunspot.*

1. INTRODUCTION

Coronal magnetic fields are involved in practically all phenomena of solar activity and in shaping the structure of solar corona. Since those magnetographic measurements that employ the Zeeman effect on ion line emission are difficult to apply to faint coronal lines, radio polarization observations are preferred [1]. The detection of polarization changes due to the crossing of magnetic field lines by microwaves at an exactly or a nearly right angle (i.e., quasi-transverse, QT) can supply precise and well-localized radio measurement in the range from a few to one hundred gausses. Such measurements of coronal field in solar active regions (ARs) make use of the theoretical Eq. (1) and employ studies of observed changes of circular polarization due to QT-propagation of microwaves [2].

Here we present the radio measurements of coronal field in three cases of fan-spine magnetic field configurations (FSCs) and the preparatory work for future diagnostics of the QT-propagation of microwaves in the FSCs. In contrast to the elongated in latitude bipolar ARs, the FSCs investigated here represent a dominant sunspot with circumjacent magnetic flux of opposite polarity. The magnetic field structure of such an FSC is characterised by a magnetic null point, a spine line, and a dome-shaped fan surface that is also a separatrix surface [3]. Accordingly, there are two systems of field lines (Figs. 1d, 2e, and 3c): the lower-lying field lines surrounding the inner spine line and the overlying field lines surrounding the outer spine line.

When such ARs are close to the central solar meridian, the region of QT-propagation (QT-region) is dome-shaped for the lower-lying system, while not coincident with the fan dome. This shape determines the time evolution with solar axis rotation of polarization inversion in FSCs.

FSCs are regarded as locations of possible flaring activity and thus are important targets of investigations. Yet some essential characteristics of the coronal magnetic field structure such as field strength, gradients, scales of magnetic divergence, which are key values for energy estimates and modelling, are not measured; hence, coronal radio magnetography is of great potential value.

Since the magnetic fields of FSCs are believed to remain potential fields outside the periods of flaring activity [4], we use the potential-field source-surface model (PFSS) with the HMI synoptic maps of the radial component B_r as the boundary conditions. With the goal to reveal and analyse the non-potential components of the magnetic structure, some authors [5]–[9] have already investigated the sampled FSCs. In contrast, our work concerns the robust potential magnetic structure, which shows modifications of the QT-region in the course of solar axis rotation in accordance with the variations of the propagation angle. A stable potential configuration then reveals polarization changes that are expected in quiet time intervals and thus measured coronal fields are the undisturbed values useful for comparative analyses with the perturbed magnetic field values during the time of flaring.

A general application of Eq. (1) for coronal magnetography requires the knowledge of the degree of circular polarization for the emitted radiation ρ_0 before crossing the QT-region. However, for an FSC a given emission source may remain covered by the dome-shaped QT-region during the whole observation period of several days, thus making the measurement of ρ_0 impossible. The use of zero-polarization observations avoids this complication. Here we present the coronal locations in the QT-regions where radio

polarization turns to zero and thus makes the radio measurements indifferent to the initial microwave polarization.

In this work we use the imaging and the spectral-polarization radio observations of FSCs to perform radio measurements of coronal fields. In particular, we analyse radio scans in Stokes V at a set of observational frequencies taken with the RATAN-600 radio telescope (angular resolution $\Theta = 20''$ at 12.9 GHz [10]) to diagnose the strong dependence of polarization changes on observing frequency. Imaging polarization observations with the Nobeyama Radioheliograph (NoRH; angular resolution $\Theta = 15''$ at 17 GHz [11]) and the Siberian Solar Radio Telescope (SSRT; angular resolution $\Theta = 20''$ at 5.7 GHz [12]) are used to localize the radio measurements in the plane of view. Finally, we note the characteristic features of polarization changes and discuss the results of radio measurements.

2.RADIO MEASUREMENTS OF THE MAGNETIC FIELD

Our radio measurements of coronal magnetic fields are based on the effects of QT-propagation determined by Eq. 1. Let ρ_0 be the degree of the circular polarization of emitted radio waves before crossing a QT-region, where the propagation angle $\alpha = 90°$. The authors [13] gave the following degree of the circular polarization ρ after crossing the QT-region:

$$\rho = \rho_0 \cdot (2 \cdot \exp(-1.15 \times 10^3 B^3 N_e L_d \lambda^4) - 1), \quad (1)$$

where B is the strength of coronal magnetic field, N_e is the electron density, L_d is the scale of coronal field divergence along the wave path, and λ is the known observing wavelength at the corresponding frequency $F = c/\lambda$.

To evaluate both B and the product $N_e L_d$ directly from radio observations one needs a detection of the full Stokes vector of radio intensities with high angular and frequency resolution [14]. There authors deduced $B = (1.28–1.12)\times10^{-3}$ T and $N_e L_d = (1.4–2.1)\times10^{10}$ m^{-2} from the radio observations made by [15].

Otherwise, the most sensitive radio measurements of coronal field correspond to the detection of nearly zero circular polarization. For the case of $\rho = 0$, one can immediately evaluate B, given the product $N_e L_d$. At the observing frequencies of 17 GHz (NoRH) and 5.7 GHz (SSRT) the corresponding fields of about 8.4×10^{-3} T and 2×10^{-3} T are measurable, assuming $N_e L_d = 10^{10}$ m^{-2}.

When attempting coronal radio magnetography of FSCs in the $\rho \neq 0$ cases, a common difficulty is the unknown initial polarization ρ_0, since the observed microwave source might be affected by QT-propagation during the whole observation period. That is why we do not construct 3D coronal magnetograms but evaluate the coronal field only in some locations within the QT-regions.

Regarding the unknown product $N_e L_d$, it should be noted that in some FSCs plasma density varies by two orders of magnitude during a coronal rain [8]. Similarly, the scale of the magnetic field divergence L_d is expected to be a few orders of magnitude smaller near null points. For the time intervals of no flaring in FSCs, we adopt the maps of the differential emission measure (DEM) of the Solar Dynamics Observatory

(SDO) AIA observational data in the Integrated Data & Operation Center (IDOC) database and estimate N_e in the region of radio measurements with the assumed hydrostatic scale length of Z_H = 47 Mm [16]. The column emission measure *EM* is used as a rough estimate of electron density, $Ne = (EM/Z_H)^{0.5}$. The scale length *Ld* of the magnetic field divergence is estimated with the help of the PFSS model (Table 1).

For a given AR for PFSS modelling we use a single synoptic SDO/HMI magnetogram, which spans one Carrington rotation. To reduce some inaccurate results of PFSS modelling, we remesh the magnetogram data onto a uniform grid, which includes both poles [17]. The following case studies are ordered in succession of the complexity of the inversion effect.

2.1. AR 12488 on 26 January 2016: A Single Polarization Inversion

The authors of [8], [9] confirmed null point topology of AR 12488 magnetosphere (at the height of $H_{NP} \approx 112$ Mm) during the next solar rotations of the AR. A long-lasting coronal rain along the spine line (for 59 hours on March 13) and an immediate reappearance of the filament after its eruption on 27 February ware analysed.

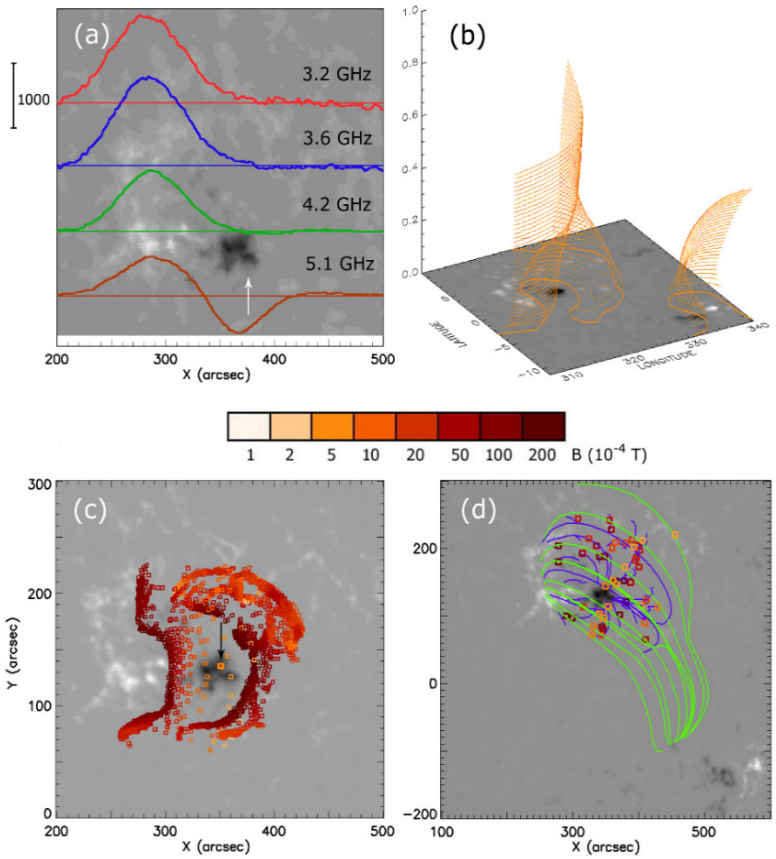

Fig. 1. (a) The RATAN-600 1D radio scans in circular polarization at four frequencies. (b) 3D surfaces of QT-propagation. (c) Colour-coded coronal field strengths at some crossings of the QT-region. (d) Field lines of the FSC surrounding the inner spine line (blue colour) and the outer spine line (green colour).

On 26 January 2016, the sign of circular polarization above the dominant sunspot of negative magnetic polarity inverted at frequencies shorter than 3.6 GHz. During the next two days the inversion extended to frequencies $F < 7.3$ GHz and $F < 10$ GHz, respectively. Earlier, near the eastern solar limb, the RATAN-600 scans showed polarization inversions of the microwave sources of positive magnetic polarity closest to the limb. These characteristics of polarization inversions in microwave are typical for the extended in latitude bipolar ARs [2]. It seems that like the QT-region of this FSC is a tall dome-like surface that at larger heights mimics the QT-region of a typical bipolar AR.

Figure 1 demonstrates the correspondence between the microwave polarization inversion at 3.6 GHz (Fig. 1a) and the coronal field at the site of the modelled region of QT-propagation (Fig. 1c). With $N_e L_d = 4.6\times10^9$ m^{-2} (Table 1), the observing wavelength $\lambda = 8.32\times10^{-2}$ m ($F = 3.6$ GHz), and observed depolarization $\rho = 0$ (vertical marked with the white arrow) one gets by means of Eq. 1 the coronal field $B = 1.4\times10^{-3}$ T. The height of the QT-crossing in the PFSS model is $H = 100$ Mm (this site is marked with the black arrow). This coronal site is located in the outer field line system of the FSC overlying the sunspot-associated microwave source on 26 January 2016. We focus only on a short segment inside the line of depolarization bearing in mind that the knife-like diagram of the RATAN-600 is 70.8 angular second wide at 3.6 GHz. Nevertheless, it is enough to evaluate the possibility of employing radio observations to estimate the coronal magnetic fields in FSCs through the QT-propagation of microwaves.

2.2. AR 11579 on 3 October 2012: Stripes of Inverted Polarization

The authors in [5] analysed the non-potential components of the magnetic structure near the dominant sunspot of AR 11579. The authors revealed the links between the magnetic flux cancellation and the formation of UV bursts on 30 September 2012.

On 1 and 3 October 2012 the SSRT maps of circular polarization at 5.7 GHz started to show the development of stripes of opposite polarity (Figs. 2a and 2b). On 5 October 2012 (not shown), the sign of polarization at 5.7 GHz inverted completely for the sunspot-associated microwave source despite the lack of any considerable changes in the photospheric magnetic field. Such an inversion with the sunspot approaching the solar limb is a clear indication of the effect of QT-propagation of microwaves, while the stripes of the inverted polarity is an unexpected feature. In the case of a bipolar AR elongated in latitude, the QT-region is expected to be a surface with a monotone decrease of magnetic field intensity with height while the original unaffected distribution of circular polarization ρ_0 above a sunspot-associated microwave source would be of a horseshoe shape [18].

We attribute appearance of these stripes in polarization to a fragmentation in the circumjacent sources of opposite magnetic polarity. Figure 2d shows a field line representing one of the fragmentations in the magnetic structure owing to the fragmented sources of circumjacent opposite magnetic polarity. The black arrow points to the coronal site where microwaves cross this field line transversally at $B = 2.34\times10^{-3}$ T (Table 1). The form and size of QT crossings vary during the course of the solar rotation. For an equidistant grid of the starting points in the PFSS model the representative crossings of the QT-region form rings in the volume of the lower-lying field lines and stripes in over-lying field lines (Figs. 2c, 2d).

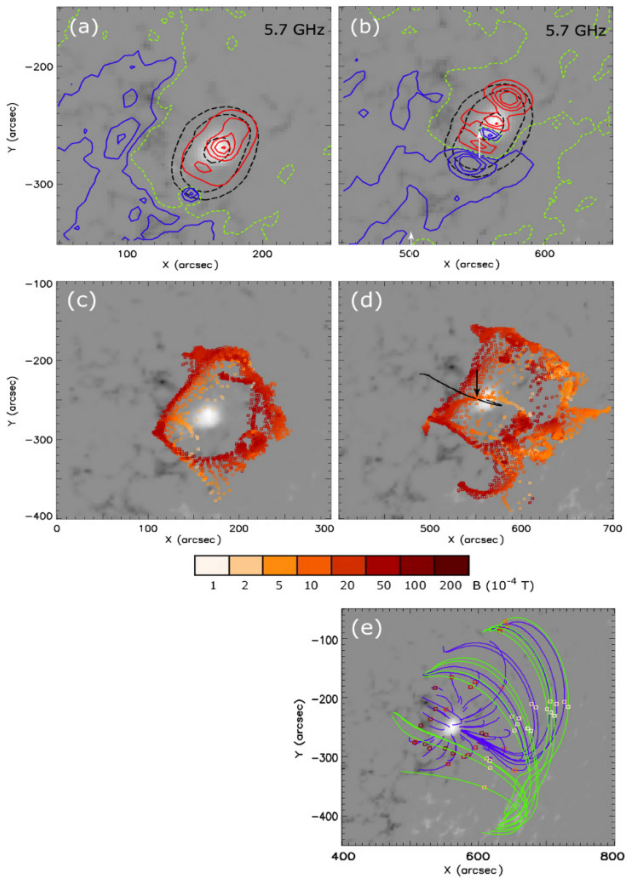

Fig. 2. (a) The SSRT radio map in total intensity (black dashed contours) and circular polarization (red and blue contours) on 1 October and (b) on 3 October 2012. (c) Color-coded coronal field strengths at selected crossings of the QT-region on 1 October and (d) on 3 October 2012. (e) Field lines of the FSC surrounding the inner spine line (blue colour) and the outer spine line (green colour).

With $Ne\,Ld = 6.4\times10^{9}$ m^{-2} (Table 1), the observing wavelength $\lambda = 5.2\times10^{-2}$ m (F = 5.7 GHz), and the observed depolarization $\rho = 0$ (site marked with the white arrow) one gets by means of Eq. 1 coronal field $B = 2.34\times10^{-3}$ T. The height of the QT-crossing in the PFSS model is $H = 50.2$ Mm (the site is marked with the black arrow). Again, the model location of the depolarized 5.7 GHz emission does not precisely correspond to the observed one but is sufficient to evaluate the possibility of using the radio observations for measurements of the coronal fields of FSCs.

2.3. AR 12242 on 18 December 2014: A Double Polarization Inversion

In [4], [6], and [7] the non-potential components of the magnetic structure near the dominant sunspot of AR 12242 on 17 December 2014 were analysed. The findings of [4] were as follows: (a) the potential field extrapolation reproduced a fan-spine topology at the time of no flaring and (b) the circular ribbon flare was caused by the unstable outer loops, which conveyed the spine field line. In [6] the authors studied the circular ribbon flare using NoRH radio observations and found that radio polar-

ization sign reversed in the central region of the positive magnetic polarity, which implied a magnetic breakout-type eruption in the FSC. The authors of [7] concluded from non-linear force-free field extrapolations that the magnetic null pointed at the height of about 36 Mm did not project itself on any part of the sunspot on 17 December. The EUV remote brightening confirmed the closed outer spine line as inferred from the magnetic field extrapolation. The evolving flux rope started eruptive expansion when it reached the height of ≈ 30 Mm.

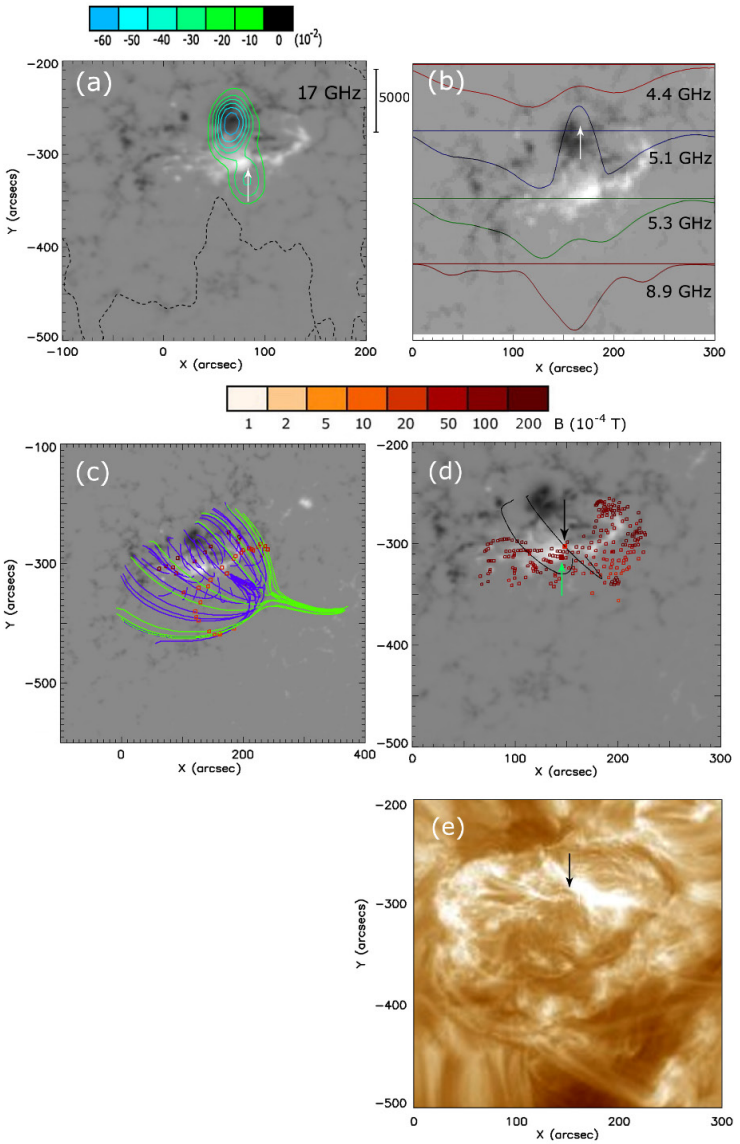

Fig. 3. (a) The NoRH radio map in the degree of circular polarization. (b) The RATAN-600 1D radio scans in circular polarization at four frequencies. (c) Field lines of the FSC surrounding the inner spine line (blue colour) and the outer spine line (green colour). (d) Color-coded coronal field strengths at representative crossings of the QT-region (the green arrow points to radio measurements at $H = 3.45\times10^7$ m; the black arrow points to radio measurements at $H = 6.6\times10^7$ m). (e) The SDO/AIA EUV image in the emission lines of Fe XII, XXIV (the black arrow points to the hot coronal loops).

In this AR, a total of three cases of polarization inversion is observed. First, the southern sunspot of positive magnetic polarity (white colour in Fig. 3) displays reversed from expected sign of circular polarization at 17 GHz at all times during its passage across the solar disc due to solar axis rotation. Such behaviour is different from that observed with elongated in latitude bipolar ARs. As seen in Fig. 3c, the sunspot is enclosed by the low-lying field lines of the FSC and the resulting QT-surface. It remains the case during the whole passage and, as a result, we do not know the initial polarisation ρ_0 for the radiation emitted from this region. The depolarization line at 17 GHz (dashed line in Fig. 3a) is located at a distance from these microwave sources and is not affected by the QT-propagation of 17 GHz emission. Nevertheless, we calculated the minimal strength of coronal field in the QT-region as the prerequisite for the sign inversion of circular polarization at 17 GHz, $B > 37.2\times10^{-4}$ T (green arrow in Fig. 3d) assuming zero polarization for a sunspot of positive magnetic polarity at this site.

Second, polarization inversion above the sunspot of positive magnetic polarity is the inversion recorded by RATAN-600 at about 5.2 GHz (Fig. 3b). According to PFSS modelling and coronal density estimate, the coronal field at the second crossing of the QT-region (black arrow in Fig. 3d) equals 19.9×10^{-4} T at $H = 6.6\times10^{7}$ m.

Third, it can be seen at 4.4 GHz that the polarization assumes the initial sign of circular polarization, which implies an additional inversion. However, we find no model crossings of QT-region corresponding to the observed change of the sign of circular polarization between 5.1 GHz and 4.4 GHz (see the vertical along the white arrow in Fig. 3b).

We suppose that a different mechanism not due to QT-propagation is responsible for the rapid with frequency polarization changes at the short frequencies below 5.1 GHz. It might be due to propagation of microwaves through the hot plasma with negative gradient along the wave path. The above polarization inversion measurements are from a location (black arrow in Fig. 3d) where a flux rope of hot plasma erupted during the impulsive phase of a flare on 17 December 2014 at 04:18 UT [7]. On 18 December 2014 10:05 UT, the central temperature of DEM parametrization, which gives an indication of mean plasma temperature along the line of sight, 7.4×10^{6} K, is still high (black arrow in Fig. 3e). As proposed by [19], some hot coronal loops can produce multiple polarization inversions in relatively narrow frequency bands due to negative gradient of plasma temperature along the wave path.

3. RESULTS AND DISCUSSION

We present radio measurements of coronal magnetic field at the sites where the sign of the observed circular polarization changed due to the QT-propagation of microwaves. Given the plasma density N_e (evaluated from the DEM in six EUV bands) and the scale of field divergence L_d (calculated by means of the PFSS model) we find that the measured strengths of the coronal magnetic fields lie in the range $(1.4–2.34)\times10^{-3}$ T. The heights of the locations where the coronal fields are measured, were calculated with the PFSS model and were found to be in the range of 100–50.2 Mm.

Table 1. Overview of the Three Analysed Fan-Spine Magnetic Configurations

Time	AR number	Telescope	F, GHz	Ne, 10^3 m^{-3}	B, 10^{-4} T	Ld, 10^7 m	H, 10^7m
				Parameters from observations		Parameters from the PFSS model	
2016 Jan 26 09:43 UT	12488	RATAN-600	3.6	1.41	14	0.325	10
2012 Oct 3 05:00 UT	11579	SSRT	5.7	1.74	23.4	0.37	5.02
2014 Dec 18 03:00 UT	12242	NoRH	17	2.6	> 37.2	4.71	3.45

- This work is the first attempt to measure coronal magnetic fields in FSCs using the sites of depolarisation at microwave frequencies in the QT-regions. We have investigated QT-propagation of microwaves only at several locations where the product $Ne\,Ld$ varies in the range of $(0.46–0.64)\times10^{10}$ m^{-2} and have avoided the assumption of constant $NeLd$ as practiced for the elongated in latitude bipolar ARs by specifying the parameters for each FSC.
- The measured coronal fields are consistent with the parameters Ne and Ld in the sense that these independently evaluated parameters provide reasonable values of the measured coronal field B (cf. [20]). We try to avoid the post-eruptive structures for the validity of the above parameters for the potential magnetic structures.
- We regard two systems of field lines in FSCs: the lower-lying field lines underneath the fan surface dome and the overlying field lines. An additional third system is formed by the large overlying loops [21]. Each system produces a specific shape and height of the QT-region and some distinct features of polarization changes in the microwave wavelength range for the first two systems and at decametric wavelengths (not analysed here) for the large overlying loops.

4. CONCLUSIONS

The results of the three case studies do not permit us to arrive at an explicit formulation of diagnostics of QT-propagation in FSCs. There is a set of various polarization and time evolution features, which are different from those of the elongated in latitude bipolar ARs [2]. In particular, we observe the stripes of inverted polarization (the case of AR 11579) and polarization inversion of a sunspot-associated source persistent with solar rotation (the case of AR 12242). The main conclusion we draw is the confirmation of the possibility to augment radio measurements with PFSS modelling for FSCs in quiet non-flaring state. A broader range of samples is required to formulate the general diagnostics for the recognition of the QT-propagation in FSCs.

ACKNOWLEDGEMENTS

We acknowledge data use from the Special Astrophysical Observatory and the Radio-Astrophysical Observatory of the Russian AS, as well as the National Astronomical Observatory of Japan and the ME-DOC data and operations center.

REFERENCES

1. Alissandrakis, C.E., & Gary, D.E. (2021). Radio Measurements of the Magnetic Field in the Solar Chromosphere and the Corona. *Frontiers in Astronomy and Space Sciences, 7*, 591075, 1–24. doi: 10.3389/fspas.2020.591075.
2. Ryabov, B. in (2004). In *Solar and Space Weather Radiophysics.* Dordrecht: Kluwer Academic., (pp.135–152). doi: 10.1007/1-4020-2814-8.
3. Pontin, D.I., Priest, E.R., & Galsgaard, K. (2013). On the Nature of Reconnection at a Solar Coronal Null Point above a Separatrix Dome. *The Astrophysical Journal*, *774*, 154. doi:10.1088/0004-637X/774/2/154.
4. Liu, C., Lee, J.,& Wang, H. (2019). The Eruption of Outer Spine-like Loops Leading to Double-stage Circular-ribbon Flare. *The Astrophysical Journal*, *883*, 47. doi:10.3847/1538-4357/ab3923.
5. Nelson, C.J., Doyle, J.G., & Erdélyi, R. (2016). On the Relationship between Magnetic Cancellation and UV Burst Formation. *MNRAS*, *463* (2), 2190–2201. doi:10.1093/mnras/stw2034.
6. Lee, J., White, S.M., Chen, X., Chen, Y., Ning, H., Li, B., & Masuda, S. (2020). Microwave Study of a Solar Circular Ribbon Flare. *The Astrophysical Journal*, *901*, L10. doi:10.3847/2041-8213/abb4dd.
7. Joshi, N.C., Joshi, B., & Mitra, P. (2021). Evolutionary Stages and Triggering Process of a Complex Eruptive Flare with Circular and Parallel Ribbons. *MNRAS*, *501* (4), 4703–4721. doi: 10.1093/mnras/staa3480.
8. Mason, E.I., Antiochos, S.K., & Viall, N.M. (2019). Observations of Solar Coronal Rain Point Topologies. *The Astrophysical Journal Letters*, *874*, L33. doi: 10.3847/2041-8213/ab0c5d.
9. Mason, E.I., Antiochos, S.K., & Vourlidas, A. (2021). An Observational Study of a "Rosetta Stone" Solar Eruption. *The Astrophysical Journal Letters*, *914*, L8. doi: 10.3847/2041-8213/ac0259.
10. Bogod, V.M., Stupishin, A.G., & Yasnov, L.V. (2012). On Magnetic Fields of Active Regions at Coronal Heights. *Solar Physics*, *276*, 61–73. doi: 10.1007/s11207-011-9850-2
11. Nakajima, H., Enome, S. et.al. (1994). In *New Look at the Sun with Emphasis on Advanced Observations of Coronal Dynamics and Flare*, Proceedings of Kofu Symposium, NRO report 360, 19.
12. Grechnev, V.V., Lesovoi, S.V., Smolkov, G.Ya., Krissinel, B.B., Zandanov, V.G., Altyntsev, A.T., … & Lubyshev, B.I. (2003). The Siberian Solar Radio Telescope: The Current State of the Instrument, Observations, and Data. *Solar Physics*, *216*, 239–272. doi:10.1023/A:1026153410061
13. Zheleznyakov, V.V., & Zlotnik, E.Ya. (1964). Polarization of Radio Waves Passing through a Transverse Magnetic field Region in the Solar Corona. *Soviet Astronomy*, *7*, 485.
14. Segre, S.E., & Zanza, V. (2001). Evolution of Polarization for Radiation Crossing a Plasma Layer of Quasi-transverse Propagation and the interpretation of Radioastronomical measurements. *The Astrophysical Journal*, *554*, 408-415. doi: 10.1086/321352.

15. Alissandrakis, C.E., & Chiuderi Drago, F. (1994). Detection of Linear Polarization in the Microwave Emission of Solar Active Region. *The Astrophysical Journal*, *428*, L73-L76. doi: 10.1086/187396.
16. Aschwanden, M.J., & Nitta, N. (2000). The Effect of Hydrostatic Weighting on the Vertical Temperature Structure of the Solar Corona. *The Astrophysical Journal Letters, 535,* L59-L62. doi: 10.1086/312695.
17. Tóth, G., van der Holst, B., & Huang, Z. (2011). Obtaining Potential Field Solutions with Spherical Harmonics and Finite Differences. *The Astrophysical Journal*, *732*, 102. doi:10.1088/0004-637X/732/2/102.
18. Gelfreikh, G.B., & Lubyshev, B.I. (1979). Structure of Local Sources of the S Component of Solar Radio Emission. *Soviet Astronomy*, *56*, 562–573.
19. Kaltman, T.I., Sheiner, O.A., & Zlotnik, E.Ya. (2008) Reversal of the Polarization of Cyclotron Radiation in a Hot Coronal Loop. *Astrophysical Bulletin*, *63* (2), 156-168. doi: 10.1134/S1990341308020065.
20. Ryabov, B.I., Maksimov, V.P., Lesovoi, S.V., Shibasaki, K., Nindos, A., & Pevtsov, A. (2005). Coronal Magnetography of Solar Active Region 8365 with the SSRT and NoRH Radio Heliographs. *Solar Physics*, *226*, 223–237. doi: 10.1007/s11207-005-2691-0.
21. Chen, X., Yan, Y., Tan, B., Huang, J., Wang, W., Chen, L., … & Masuda, S. (2019). Quasi-periodic Pulsations before and during a Solar Flare in AR 12242. *The Astrophysical Journal Letters, 878*, 78. doi:10.3847/1538-4357/ab1d64.

sciendo

LATVIAN JOURNAL OF PHYSICS
AND TECHNICAL SCIENCES
2023, N 2

DOI: 10.2478/lpts-2023-0012

AIR FLOW ANALYSIS FOR PROTECTIVE CLOTHING VENTILATION ELEMENTS WITH AND WITHOUT CONSTANT CROSS-SECTION AREA OPENING

A. Janushevskis[1], S. Rajni Vejanand[1], A. Gulevskis[2]

[1] Institute of Mechanics and Mechanical Engineering
Riga Technical University, 6b, Ķipsalas Str., LV-1048, LATVIA
[2] Ekasol Ltd. 15, Jauna Str., Ropazi, LV-2135, LATVIA
*e-mail: Sanjay.Vejanand@rtu.lv

In this paper a ventilation element is designed with the constant cross-sectional area of 3.14 mm^2 with the outer ring, to study the efficiency of ventilation at three different inlet air velocities (2, 5 and 8 m/s). There are five different cases analysed in the study, in which four cases are with different coordinate values of outer ring and core while the fifth case is studied with ventilation element without outer ring. The results of all five cases are analysed and compared to see the efficiency of ventilation element design. These ventilation elements are attached at ventilation hole at the inner part of the protective jacket. The attached ventilation element increases mechanical strength of the clothing by covering ventilation hole and restricting direct access of insects to the body. Moreover, ventilation elements permit smooth flow of air inside jacket. The objective is to determine which element's geometrical configuration results in the minimum flow energy losses in the cell flow channel from the inlet to the outlet, which are represented by the pressure difference. Flow energy losses increase with increasing pressure difference (ΔP), and the body cooling reduces if the flow is weakened or there is of lost energy. SolidWorks Flow Simulation is used to calculate the pressure, temperature, and heat flux for the simplified elliptical model of the human body with a protective jacket. The obtained results are compared and analysed to study the concept of constant cross-sectional area in the design of ventilation elements with and without outer ring. The pressure and temperature difference for each case are calculated for the comparison and the obtained results show that the element design without outer ring provides better overall results and less flow energy loss in the cell flow channel than that of element design with outer ring.

Keywords: *Flow simulation, heat transfer, protective clothing, ventilation element.*

1. INTRODUCTION

The effects of fabric ventilation and cooling are essential to human comfort in the clothing design. When people are subjected to extremely high temperatures, their ability to regulate their body temperature may be affected, leading to symptoms including heat exhaustion and heat stroke [1]. Various occupations frequently demand their employees to do tasks in warm environments where they are subjected to significant heat stress, which lowers job performance and productivity [2]. Heat stress is a major factor in industrial accidents and injuries and affects people's ability of mental awareness, attention, and coordination of their movements [3]. In all of these circumstances, personal cooling (PC) systems are a practical and economical approach to reduce the microclimate of users. Personal cooling clothing, for instance, can simply be helpful in instances when protective clothing is necessary to manage the micro-climate of people for heat-stress regulation [4]. Multi-layer structure is often used in thermal protective clothing, such as firefighters' gear, winter outdoor clothing, and ballistic protection apparel, where each layer has a certain function [1], [2]. The internal layer (typically a 3D fabric layer) allows the movement of moisture and air between the system and its surroundings, while the external layer safeguards it from the environment, and the intermediary thermo-insulating layer protects against extreme heat loss. The air space between the skin and the inner layer is referred as the "microclimate" that could affect heat and mass transfer from or to the body, for e.g., protective gear, where the micro-climate is often thicker, decreasing the probability of natural convection [3]. In order to characterise the thermal comfort of clothing when worn, research and development of a multi-layer textile package need knowledge of relevant fluid flow and heat transfer mechanisms. Important comfort characteristics of clothing include the fabrics capacity for thermal insulation, which includes thermal resistance, water-vapour resistance, and air permeability. The commonly used breathable clothing offers enough vapour permeability, but frequently fall weak when it comes to body ventilation and mechanical protection, for instance, against some insect species, primarily mosquitoes, which are known to transmit harmful diseases like dengue and malaria. Conversely, wearing clothing composed of thick fabrics that effectively safeguards against insects, greatly raises the danger of overheating of body. Mechanical protection and air permeability are essentially opposite needs. Development of composite materials for use in protective gear that offer mechanical protection to the body and enhance airflow between the body and the clothing is the primary demand [5].

This work mainly focuses on protective clothing which is especially intended for use in warm and hot climatic conditions used in travelling, expeditions, hunting, fishing, forestry, agriculture, military and other areas, where maximum body ventilation and cooling is required. The outer layer of clothing may not have enough air permeability to adequately guard the human body from external environmental factors like rain, dust, direct sunlight, insect access, and insect bites. As a result, warm, moist air may build up on the body, causing discomfort or even increasing the risk of overheating. To enhance air exchange, numerous clos-

able vents and open areas of clothing have been developed [6]. However, this only partially improves air exchange, leaving the issue unresolved. The key benefit of the established approach is that it effectively protects the human body from the effects of different external climatic conditions, ensuring the necessary air circulation and under-clothing ventilation, and lowering the risk of overheating the body [7]. To achieve the goal, a complex task, such as form optimization of the ventilation elements, is performed. A ventilation element is used to cover the ventilation hole which helps to provide mechanical strength to clothing as well direct inlet air to the rest part of the system. In this study we have designed a ventilation element with constant arc length with outer ring to investigate its efficiency. Moreover, different coordinate values are used in design of element and results are compared and analysed to propose optimum design. There is a demand on the market for more effective technical solutions and materials to be employed in the outer layer of protective gear, while also providing the essential ventilation even in hot weather circumstances and during heavy physical load conditions [8].

2. MODEL DESIGN AND BOUNDARY CONDITIONS

Simple elliptical models of the jacket and body are built and assembled together in this study to reduce complexity. The assembly is such that the body is in middle, and the jacket is placed over it with a uniform gap of 2.2 mm. The schematic drawing of the model is shown in Fig. 1. There is a single inlet ventilation hole of 2 mm diameter in the front side comprising of a ventilation element and ten outlet holes of 4 mm diameter at the back side of the jacket without elements.

There are four ventilation element design with outer ring named E0-30, E0-45, E0-60 and E0-90, while the fifth case consists of core without outer ring which is named E1. Figure 2 represents design of element E0-90 with core and outer ring. The coordinate values used in all cases of ventilation element design are mentioned in Table 1. All mentioned dimensions are in millimetres.

In Table 1 below, α represents reference coordinate angle 0 to 90°, X1 & Y1 represent coordinate values for the ring, while X2 & Y2 – for the core. S represents the constant cross-section area of air gap of element. This means that the cross-sectional area of at all mentioned angles between the core and outer ring is the same. The detail of element design is visible in Fig. 2.

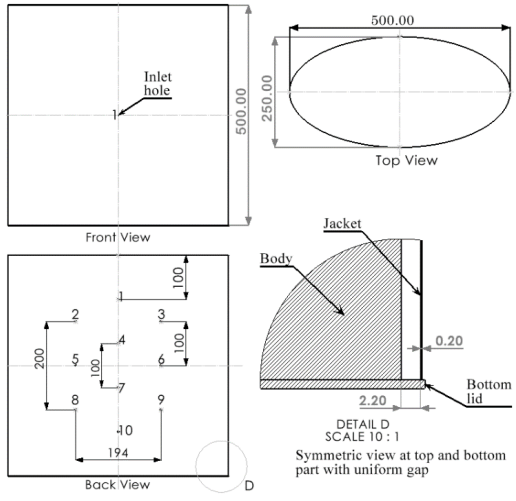

Fig. 1. Elliptical model design [9].

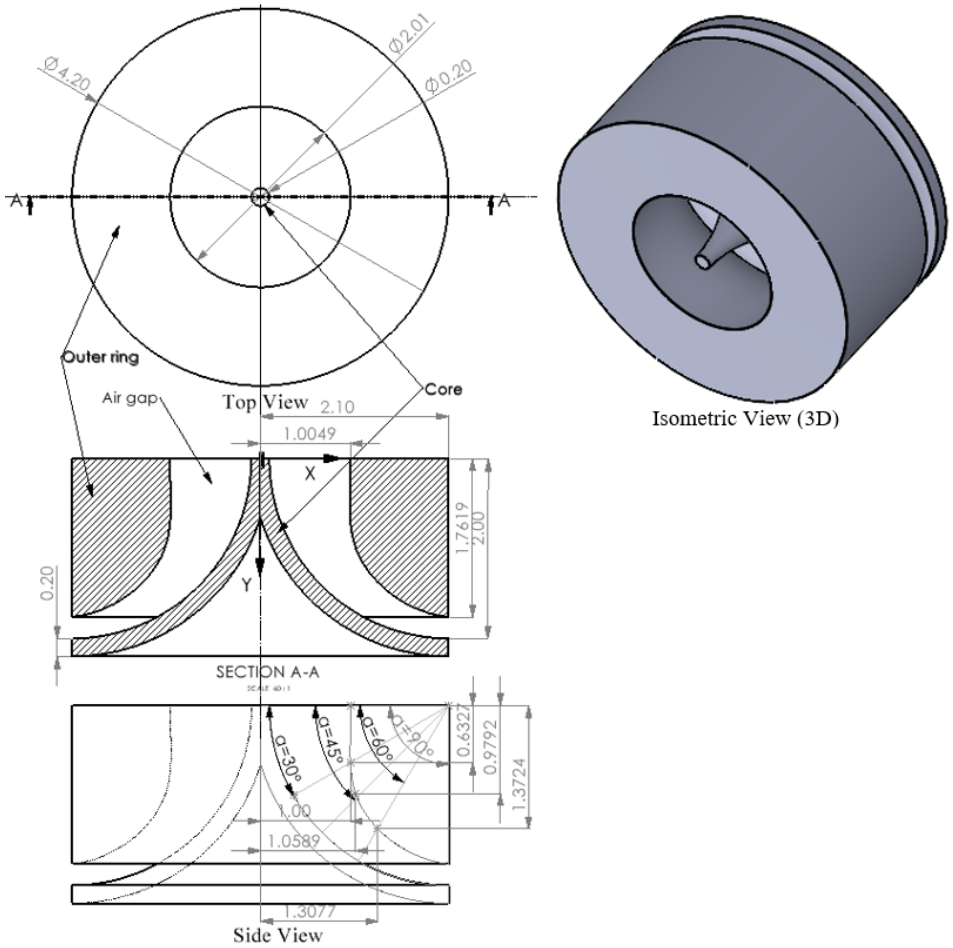

Fig. 2. Design of element E0-90.

Table 1. Coordinate Values of Element Design

α	X1	Y1	X2	Y2	S
0	1.0049	0	0.1	0	3.14
30	1	0.6327	0.3679	1	
45	1.0589	0.9792	0.6857	1.4140	
60	1.3077	1.3724	1.1	1.7320	
90	2.10	1.7619	2.1	2	

In the flow simulation analysis, the initial air temperature of 20 °C and the atmospheric pressure of 101325 Pa are used as standard values. The study is made at two different inlet air velocities of 2 and 5 m/s. The study materials of specific material properties are assigned to the jacket and body at the initial stage of simulation which are mentioned in Table 2 below. For the ventilation element and jacket, the same material properties are considered. The average human body temperature is taken as 36.5 °C and the heat generation rate of the body at normal walking condition as 200 W [10].

Table 2. Assigned Material Properties

Material properties	**Human body**	**Jacket**
Average density [kg.m^{-3}]	985	1420
Specific heat [J.kg^{-1} K^{-1}]	3600 [11]	1140
Thermal conductivity [W.m^{-1}.K^{-1}]	0.21 [12]	0.261

Assumptions taken in the flow simulation study:

- The top and bottom part of the jacket are considered closed to study the effectiveness of the ventilation.
- Radiation is not considered the heat loss by the radiation will be approximately the same in all the cases.
- Heat transfer through conduction and convection from the body to the jacket and to outer environment is taken into account.

3. RESULTS AND DISCUSSION

The presented results are calculated when inlet air enters perpendicular to the front side of inlet ventilation. The results of simulation analysis are shown for a physical time of 5 seconds with all the elements having the same set of boundary conditions and the values as those described in the previous section. Longer physical time in the analysis will require longer computations time to get the results because this is a transient phenomenon. This means time will have influence on the results but since it is comparison the change will be approximately similar for all the cases. Hence, a smaller physical time of 5 seconds is chosen for the study in order to save computation time because the differences in the results would be nearly identical at any given time. The results are obtained in terms of pressure and surface temperature of the body. These results are discussed and presented below.

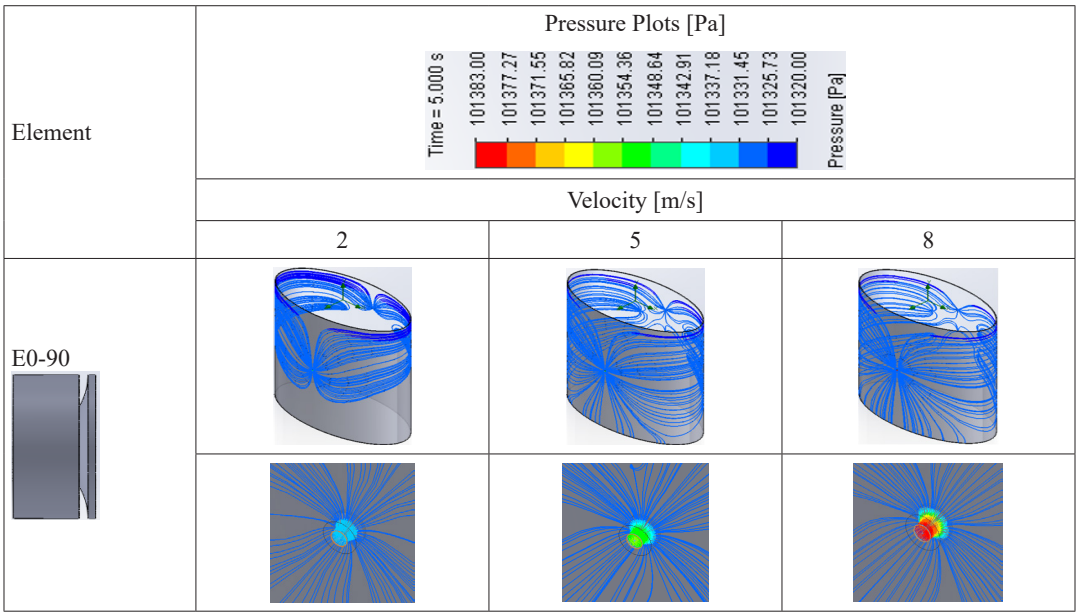

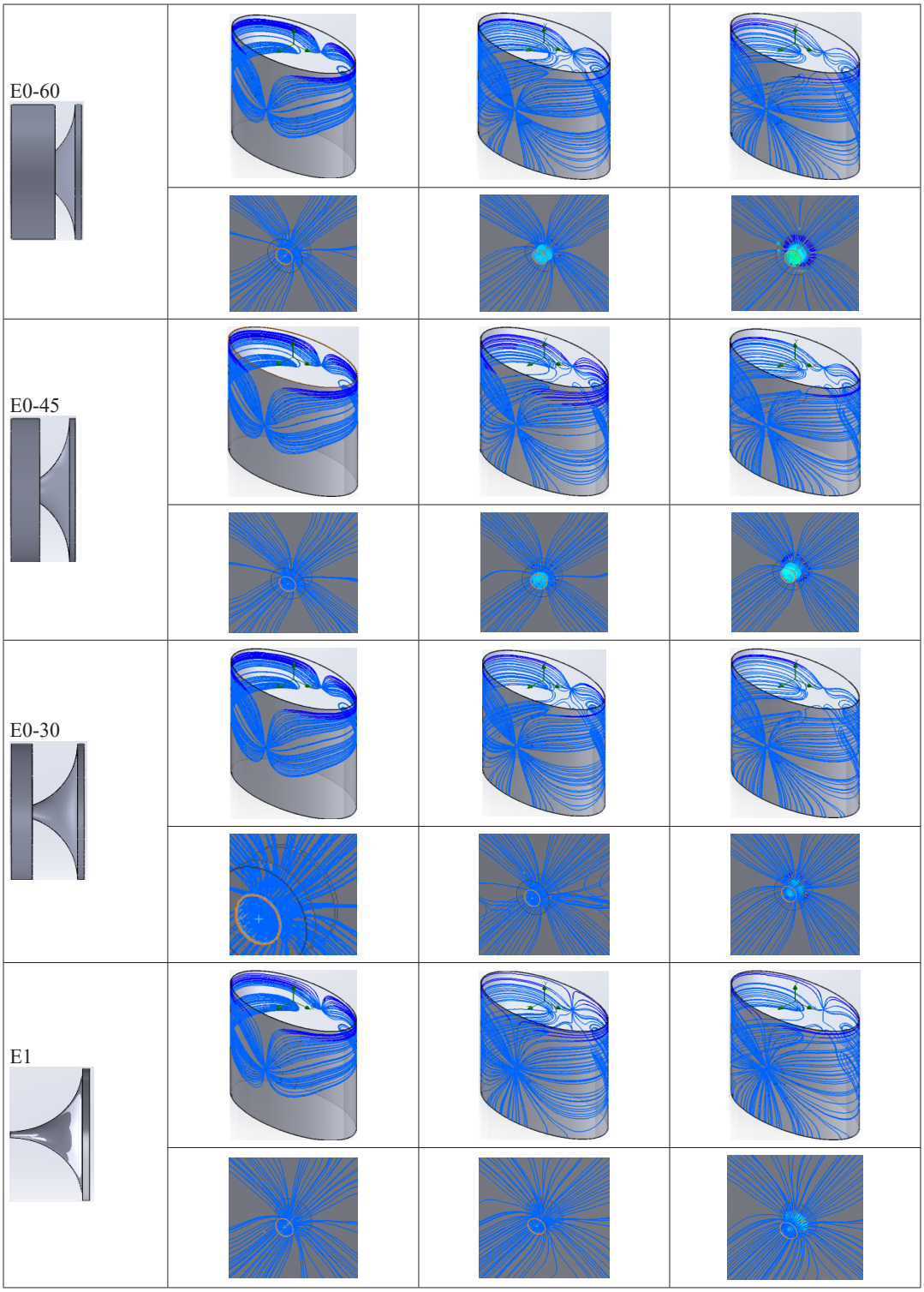

Fig. 3. Pressure stream-lines.

The flow trajectories indicating pressure distribution for each case at various inflow velocities are shown in Fig. 3. An isometric representation of the pressure distribution across the entire model is shown in the first raw of images for each case, with the same scale for easy comparison. An enlarged view near the ventilation hole is shown in the second raw of images for each case to illustrate how ventilation components affect the flow path and pressure distribution at varying air velocities. The dark blue lines near the ventilation in right column images indicate flow energy losses. In each pressure plot, an equal scale is used to compare the pressure distribution for each situation stated, and the corresponding values of the results are presented in Table 3. It is clearly visible from the plots that most of the variations occur at the inlet in the flow channel of ventilation element. Also, results show that these variations in the pressure increase with the increase in air velocities. Moreover, results also depict that as the area of ring becomes smaller, pressure variations decrease.

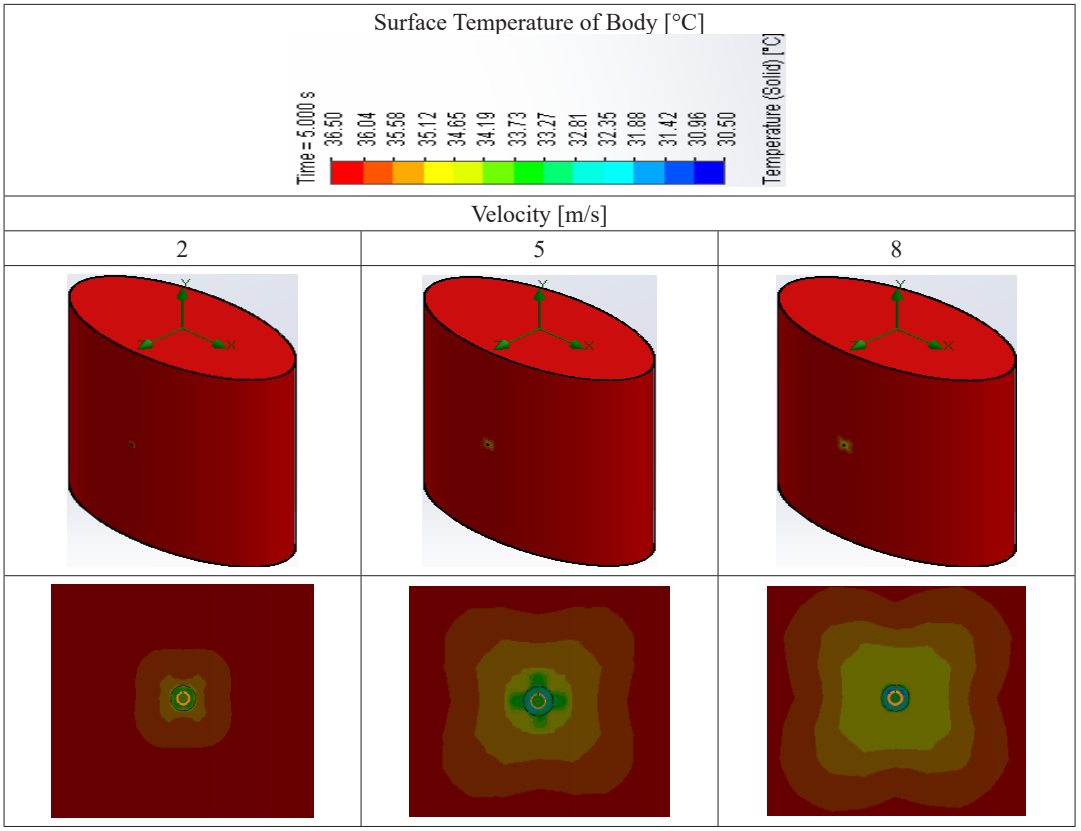

Fig. 4. Surface temperature of body in case of element E0-90.

Surface temperature of the body in case of E0-90 is presented in Fig. 4. In the plots above, top raw shows surface temperature over entire model, while bottom raw shows temperature distribution near the ventilation with enlarged view. Similarly, temperature plots for other ventilation cases are studied, and the values of the acquired results are provided in Table 3. The cooling coverage area expands in closer proximity to the ventilation hole when inflow velocity rises from 2 to 8 m/s, as seen from the temperature

plots. This makes sense because it is very obvious that with higher air velocity, heat transfer will be higher, which increases cooling capacity. The same is also true for other cases (ventilation elements).

Table 3 displays the obtained values of results, and from these values the pressure difference and temperature difference are calculated for each case. These measured pressure and temperature differences are used to compare the efficiency of mentioned ventilation element designs and to suggest the most efficient element design. The comparison is illustrated in Figs. 5 and 6.

Table 3. Obtained Values of Simulation Results

Element	Inlet velocity [m/s]	Values	Pressure [Pa]	ΔP	Surface temperature of body	ΔT
E0-90	2	Max	101335.71	10.41	36.50	3.39
		Min	101325.30		33.11	
	5	Max	101354.00	28.60	36.50	4.75
		Min	101325.40		31.75	
	8	Max	101382.94	57.53	36.50	5.03
		Min	101325.41		31.47	
E0-60	2	Max	101331.06	5.69	36.50	3.53
		Min	101325.37		32.97	
	5	Max	101337.41	12.54	36.50	4.94
		Min	101324.87		31.56	
	8	Max	101345.44	25.44	36.50	5.31
		Min	101320.00		31.19	
E0-45	2	Max	101329.67	4.41	36.50	2.9
		Min	101325.26		33.60	
	5	Max	101334.64	9.96	36.50	5.39
		Min	101324.68		31.11	
	8	Max	101343.53	20.34	36.50	5.84
		Min	101323.19		30.66	
E0-30	2	Max	101329.12	3.79	36.50	3.07
		Min	101325.33		33.43	
	5	Max	101331.64	6.16	36.50	5.29
		Min	101325.48		31.19	
	8	Max	101336.87	13.53	36.50	5.73
		Min	101323.34		30.77	
E1	2	Max	101329.30	4.01	36.50	3.34
		Min	101325.29		33.16	
	5	Max	101331.82	6.6	36.50	5.14
		Min	101325.22		31.36	
	8	Max	101337.87	13.01	36.50	5.88
		Min	101324.86		30.62	

Comparison of pressure difference for five different cases is illustrated in Fig. 5 at three different air velocities. It is clearly visible that E0-90 gives the highest pressure difference, which can also be seen in pressure plots. The elements E0-30 and E1 show the lowest pressure difference with negligible difference in pressure between them. An interesting point to notice is that as an angle **(α)** decreases from 90° to 30° in outer ring design, pressure difference also reduces. When pressure difference is lower, the flow energy losses also reduce, which leads to better cooling of the system.

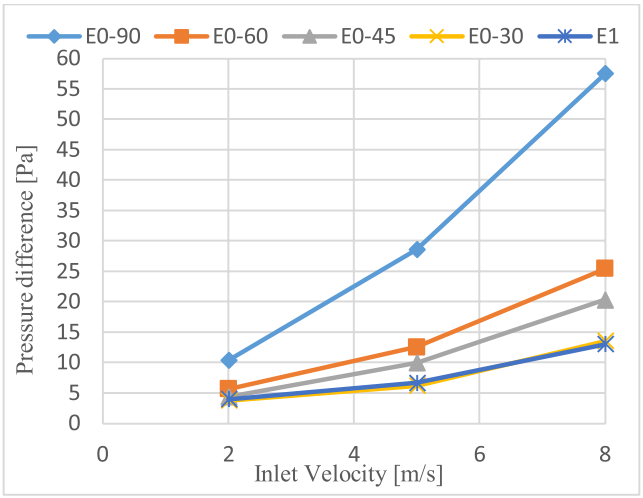

Fig. 5. Pressure difference at different air velocities.

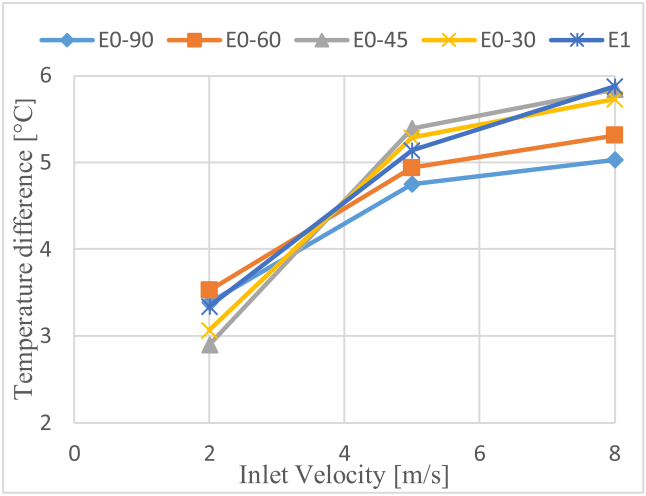

Fig. 6. Temperature difference at different air velocities.

Figure 6 shows a comparison of all mentioned cases in terms of temperature difference. Unlike pressure difference, higher temperature difference indicates better cooling. From Fig. 6, it is visible that at 2 m/s, elements E0-60 and E0-90 show the highest temperature difference but at 5 and 8 m/s both of them show the lowest temperature difference. This means that E0-60 and E0-90 may provide better cooling at lower

air velocity but are less efficient at higher inlet velocities. This is because the energy losses and pressure difference increase in these elements at higher velocities as it is visible from pressure plots. When it comes to elements E0-45 and E0-30, both of them show the lowest temperature difference at 2 m/s, but the highest one – at 5 m/s, which means they might not be very efficient at a lower speed but can provide better performance at higher air velocities. The element E1 is the one whose performance is stable and better at both lower and higher inlet velocities. This is because E1 has the smallest energy losses in the flow channel at all velocities.

4. CONCLUSIONS

In this paper, we have studied five different cases of ventilation element, whose design is based on the concept of constant cross-sectional area. As discussed above, some elements may work well at lower air velocity but can be less efficient at higher velocities and vice versa. This is a crucial point to note because certain elements could operate very well at lower velocities but have poor performance at higher velocities, making it crucial to select the appropriate element in accordance with operating parameters. Moreover, results depict that flow energy losses decrease with a decreasing reference coordinate angle in design of elements from 90° to 30°, specifically at higher air velocities. This means with a decreasing angle in design of outer ring, the results improve gradually.

It can be concluded that element E1 provides better results both at lower and higher air velocities. Moreover, E1 has the smallest energy losses in the element flow channel and shows lower fluctuations in pressure and temperature difference with the change in air velocity than the other elements. This makes element E1 more suitable over the other elements, which could provide better cooling at different inlet air velocity. Although choosing the right design can be challenging, it can be done with careful optimization and simulation analysis. CAD design and CFD software can be very important tools for such a purpose as they save a lot of time and reduce costs of manufacturing and real life experiments. In addition, the created models can be used to compare ventilation efficiency analysis, enabling further studies, such as improving the position of various ventilation elements on protective garments.

ACKNOWLEDGEMENTS

This publication has been written with the support of the Doctoral Grant Programme of Riga Technical University, project No. 2-00338.

REFERENCES

1. Udayraj, Talukdar, P., Das, A., & Alagirusamy, R. (2016). Heat and Mass Transfer through Thermal Protective Clothing – A Review. *International Journal of Thermal Sciences*, *106*, 32–56.

2. Hancock, P.A., & Vasmatzidis, I. (2003). Effects of Heat Stress on Cognitive Performance: the Current State of Knowledge. *Int. J. Hyperthermia, 19*, 355–372.
3. McMorris, T., Swain, J., Smith, M., Corbett, J., Delves, S., Sale, C., … & Otter, J. (2006). Heat Stress, Plasma Concentrations of Adrenaline, Noradrenaline, 5-Hydroxytryptamine and Cortisol, Mood State and Cognitive Performance. *International Journal of Psychophysiology*, *61* (2), 204–215.
4. Cheung, S.S. (2008). Neuromuscular Response to Exercise Heat Stress. *Med. Sport. Sci., 53*, 39–60.
5. Barauskas, R., Baltusnikaite, J., Abraitiene, A. & Grineviciute, D. (2012). Experimental Investigations and Finite Element Model of Heat and Moisture Transfer in Multilayer Textile Packages. *Fibres & Textiles in Eastern Europe., 6A* (95), 112–118.
6. Yang, A.-S., Shih, Y.-C., Lee, C.-L., & Lee, M.-C. (2013). Investigation of Flow and Heat Transfer around Internal Channels of an Air Ventilation Vest. *Textile Research Journal, 84* (4), 399–410.
7. Pourghayoomi, H., Dehghan, H., & Tarrahi, M.J. (2020). The Effect of Optimized Vest for Controlling the Women's Thermal Strain in the Hot Laboratory Conditions. *Health Scope International Quarterly Journal*, *9* (2), e94739. doi: 10.5812/jhealthscope.94739
8. Zhao, M., Gao, C., Wang, F., Kuklane, K., & Holmer, I. (2013). A study on Local Cooling of Garments with Ventilation Fans and Openings Placed at Different Torso Sites. *International Journal of Industrial Ergonomics*, 232–237.
9. Janushevskis, A., Vejanand, S., & Gulevskis, A. (2022). Analysis of Different Shape Ventilation Elements for Protective Clothing. *WSEAS Transactions on Fluid Mechanics*, 140–146. doi: 10.3794/232013.2022.17.14.
10. Kumar, R., Aggarwal, R.K., Sharma, J.D., & Pathania, S. (2012). Predicting Energy Requirement for Cooling the Building Using Artificial Network. *Journal of Technology Innovations in Renewable Energy*, *1*, 113–121.
11. Giering, K., Lamprecht, I., & Minet, O. (1996). Specific Heat Capacities of Human and Animal Tissues. *Proceedings of SPIE – The International Society for Optical Engineering*, *2624*, 188–197.
12. Rugh, J.P., & Bharathan, D. (2005). Predicting human thermal comfort in automobiles. In: *Vehicle Thermal Management Systems Conference and Exhibition*, May 2005, Toronto, Canada.

sciendo

LATVIAN JOURNAL OF PHYSICS
AND TECHNICAL SCIENCES
2023, N 2

DOI: 10.2478/lpts-2023-0013

CHEAP AND MASS-PRODUCIBLE ELECTROCHEMICAL SENSOR OF HYDROGEN PEROXIDE

V. Mizers, V. Gerbreders*, M. Krasovska, I. Mihailova,
A. Bulanovs, E. Sledevskis

Daugavpils University, Institute of Life Sciences and Technology,
1a Parades Str., Daugavpils, LV-5401, LATVIA
*e-mail: vjaceslavs.gerbreders@du.lv

Hydrogen peroxide is present naturally in any living cell. Although hydrogen peroxide concentration in cell is strictly regulated during normal metabolism, several human diseases lead to increased hydrogen peroxide concentration in body fluids. It is beneficial to monitor hydrogen peroxide levels in human body for early disease diagnostics. This can be done by creation of electronic device, which will use electrochemical sensor in order to perform automated hydrogen peroxide concentration measurement in a sample. The aim of the research is to use printed circuit board (PCB) technology in order to create a replaceable electrochemical hydrogen peroxide sensor that could be cheaply mass-produced to enable further development of automated health diagnostics device.

Keywords: *Electrochemical sensor, healthcare, hydrogen peroxide, mass production, printed circuit board.*

1. INTRODUCTION

Hydrogen peroxide (H_2O_2) is a breathing process by-product naturally present in every living cell [1], including every part of the human body [2]. Living cells have built hydrogen peroxide regulation mechanisms; thus, in small amounts hydrogen peroxide is harmless. Due to some diseases, hydrogen peroxide regulation may fail and its concentration may increase, leading to various forms of damage. Various studies have linked high hydrogen peroxide concentrations in body fluids to Parkinson's and Alzheimer's diseases [3], DNA corruption and premature cell death [4]–[6], cancer and cancer metastasis [7], and brain injuries [8]. Thus, it would be beneficial to develop a cheap and rapid method of hydrogen peroxide detection in body fluids for primary

health assessment. Up to now, hydrogen peroxide has mainly been detected by fluorescence analysis [1], [9]–[11], which requires a specially trained operator and laboratory equipment. Thus, it is an actual task to develop a hydrogen peroxide sensor that could be mass-produced cheaply and further integrated into autonomous analysis devices.

A possible way to make hydrogen peroxide analysis more accessible would be electrochemical analysis automated by computer. Recent studies have shown that electrochemical detection of hydrogen peroxide is possible in electrochemical cell with regular electrodes [12], as well as with various nanostructured electrodes [13]–[19]. It has also been demonstrated that electrochemical sensors could be integrated into small, simple and portable devices [20] that use small sample sizes for analysis. In order to create cheap and accessible hydrogen peroxide detectors, it would be beneficial to develop a cheap method of mass production of electrochemical sensors for use in such portable devices. Printed circuit boards (PCBs) could be used to achieve such goals, as they are widely used in electronics manufacture, thus making them easily available for large-scale production. This approach is very flexible, as PCBs could be designed with arbitrarily shaped, sized and positioned electrodes, as well as with gold coatings, thus making them chemically neutral. Every PCB is produced to exact dimensions, thus offering good repeatability of electrochemical measurements. It is also possible to make nanostructured PCB electrodes by using electrodeposition methods, as reported in [15]. The possibility of using PCB chips as electrochemical hydrogen peroxide sensors will be evaluated in the article. It is commonly known that hydrogen peroxide actively oxidises ferrous ions, Fe^{2+}, in solution. The reaction between H_2O_2 and Fe^{2+} is a multi-step mechanism that was previously described in [21] and can be seen in equations (1)–(4):

$$Fe^{2+} + H_2O_2 \rightarrow Fe^{3+} + OH^- + HO\cdot \quad (1)$$

$$HO\cdot + H_2O_2 \rightarrow H_2O + HO_2\cdot \quad (2)$$

$$HO_2\cdot + H_2O_2 \rightarrow O_2 + H_2O + HO\cdot \quad (3)$$

$$HO\cdot + Fe^{2+} \rightarrow Fe^{3+} + OH^-. \quad (4)$$

It can be seen that hydrogen peroxide oxidises Fe^{2+} ions to Fe^{3+}, as well as producing large numbers of free radicals. Thus, it is possible to sense the presence of hydrogen peroxide electrochemically in solution by the addition of Fe^{2+} ions and monitoring the Fe^{2+} to Fe^{3+} oxidation peak. It should be noted that it is possible to further enhance the sensitivity of electrochemical sensors by coating its electrodes with free-radical-susceptible materials, as previous studies have shown that coating electrodes with nanostructures greatly improve such sensitivity [17], [22]–[26].

2. EXPERIMENTAL

2.1. Reagents and Materials

This research used $FeCl_2$*$4H_2O$, 97 % ethanol and 30 % H_2O_2 aqueous solution purchased from Sigma-Aldrich. All solutions used were freshly prepared using distilled water.

2.2. Optical Detection of H_2O_2 in $FeCl_2$ Solution

The solution transmissivity spectrum was analysed to prove the possibility of hydrogen peroxide detection by its reaction with $FeCl_2$ in solution. The $FeCl_2$ solutions of target concentration were prepared and divided into two samples, one of which was used as a control. Hydrogen peroxide aqueous solution was added to a flask containing the other sample of $FeCl_2$ solution, thoroughly mixed and both samples placed in the dark for 15 minutes. Their transmissivity spectrum was then evaluated by Shimadzu UV-2550 spectrophotometer. The transmissivity spectra were evaluated by transmissivity change compared to the control $FeCl_2$ solution in the range of 900–300 nm.

2.3. Electrochemical Cell with PCB Electrodes

This research used a custom three-electrode electrochemical cell consisting of a PCB chip, a Ag/AgCl reference electrode (RE), and a sample solution container. Both working electrode (WE) and counter electrode (CE) were placed on a replaceable PCB chip, with the Ag/AgCl RE placed separately from the PCB. The on-chip WE and CE were produced as copper pads coated with gold by an industry-standard ENIG process. The PCB chip was designed to fit into a quick-change connector in the electrochemical cell, making it easily and quickly replaceable. PCB chips containing the WE and RE were prepared as described elsewhere [27] and replaced before each measurement.

2.4. Electrochemical Detection of H_2O_2 in $FeCl_2$ Solution

Cyclic voltammetry (CV) was used to detect the presence of hydrogen peroxide in the $FeCl_2$ solution. Two parts of freshly prepared $FeCl_2$ aqueous solution were mixed with one part of hydrogen peroxide aqueous solution and mixed thoroughly. The resulting solution consisted of 1 mM $FeCl_2$ and a target concentration of hydrogen peroxide and was placed into the sample container of the electrochemical cell and CV measurements performed after 15 minutes by sweeping the potential from –0.6 to +0.3 V vs Ag/AgCl at a sweeping rate of 50 mV/s, with starting potential of 0 V vs Ag/AgCl.

3. RESULTS AND DISCUSSION

3.1. Optical Detection of H_2O_2 in $FeCl_2$ Solution

The possibility of detection of hydrogen peroxide by reaction with $FeCl_2$ was evaluated by addition of various concentrations of aqueous hydrogen peroxide solution into 1 mM $FeCl_2$ solution.

As shown in Fig. 1, the addition of hydrogen peroxide greatly reduced transmissivity of the $FeCl_2$ solution in the range of 300–350 nm, which is a clear indication of chemical reaction between hydrogen peroxide and Fe^{2+} ions. Either this reaction itself or the reaction products can further be detected by electrochemical analysis. Experimental data suggests that hydrogen

peroxide concentrations as low as 5 μM can be detected, as they produce notable transmissivity change (–10 %).

The effect of $FeCl_2$ concentration on measurement result was evaluated by addition of 10 μM H_2O_2 into $FeCl_2$ solutions of various concentrations.

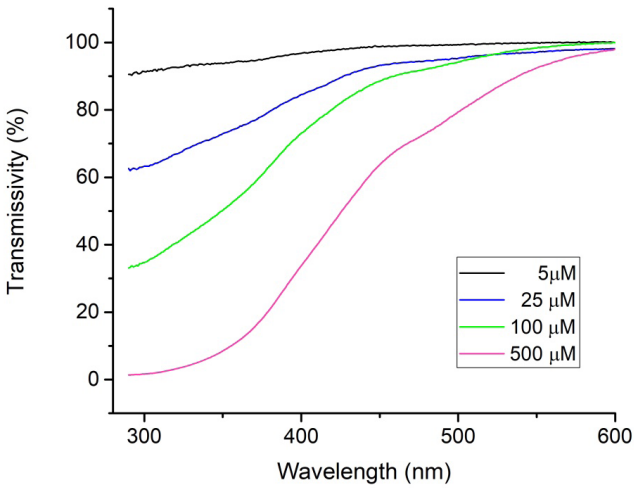

Fig. 1. 1 mM $FeCl_2$ solution transmissivity spectrum with added H_2O_2.

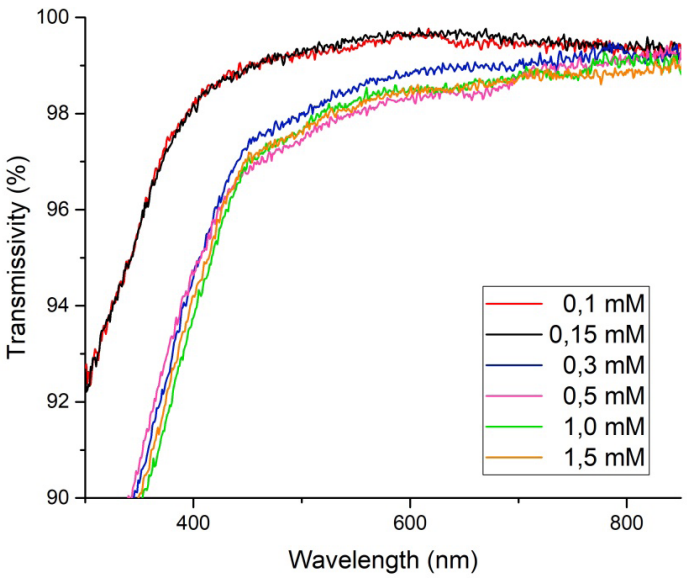

Fig. 2. Various concentrations of $FeCl_2$ solution transmissivity after 10 μM H_2O_2 addition.

As can be seen in Fig. 2, the reaction of hydrogen peroxide with $FeCl_2$ at concentrations of 0.1–0.15 mM produced small changes in transmissivity. An increase in $FeCl_2$ concentration to 0.3 mM contributes to the appearance of more significant

changes in transmission compared to 0.1–0.15 mM concentration (Fig. 2). However, a further increase in concentration above 0.5 mM does not cause significant changes and the transmission spectra coincide. It can be concluded that in order to achieve maximal detection sensitivity at small hydrogen peroxide concentrations, $FeCl_2$ should be present in a concentration at least 30-fold higher than the target hydrogen peroxide concentration. To avoid depletion of the solution, the indicated minimum value for $FeCl_2$ should be several times higher than H_2O_2 (for example, concentration of 1 mM, which is 100-fold higher than the target concentration of H_2O_2 is used).

3.2. Electrochemical Detection of H_2O_2 in $FeCl_2$ Solution

Cyclic voltammetry measurements of hydrogen peroxide in 1 mM $FeCl_2$ solution were performed as described in the previous section.

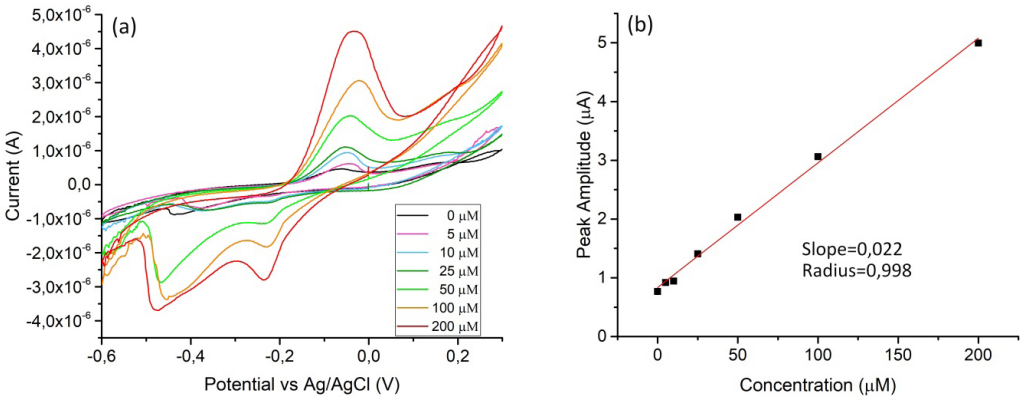

Fig. 3. Cyclic voltammetry result of H_2O_2 in 1 mM $FeCl_2$ solution (a) and –0.05 V vs Ag/AgCl peak amplitude versus hydrogen peroxide concentration (b).

As can be seen in Fig. 3a, addition of hydrogen peroxide to $FeCl_2$ solution causes an irreversible electrochemical reaction with the presence of one oxidation peak at -0.05V and two reduction peaks at -0.2V and -0.4V. It should be noted that the presence of hydrogen peroxide in solution creates a peak at –0.2 V that is not present in the voltammogram of pure $FeCl_2$. Thus, the peak at –0.2 V could be used to detect the presence of hydrogen peroxide qualitatively, and combined analysis of all peak amplitudes could be used to determine hydrogen peroxide concentration. For the quantitative determination of peroxide, the oxidation peak -0.05V is used, which corresponds to the oxidation of Fe^{2+} to Fe^{3+}. The calibration curve of the concentration dependence on the current peak amplitude is shown in Fig. 3b. Taking into account the slope of the calibration curve, the sensitivity of this sensor is 22 μA/mM. The calculated limit of detection (LOD) is 7.14 μM assuming signal-to-noise ratio = 3.

In the future, the sensitivity of this sensor can be increased by using nanostructured coatings containing iron. The use of such coatings will significantly increase the active surface area of the sensor.

Comparison of the analytical performance of the proposed electrochemical sensor with other Fe-containing H_2O_2 sensors reported previously is presented in Table 1.

Table 1. Comparison of the Analytical Performance of the Proposed Electrochemical Sensor with Other Fe-Containing H_2O_2 Sensors

Electrode		Linear range	Sensitivity	LOD	Source
Fe_2O_3/GC		10–150 μM	2.5 μA/μM	7 μM	[28]
3D micro-snowflake structured α-Fe_2O_3		0.1–5.5 mM	7.16 μA/mM	10 μM	[29]
MA-α-Fe_2O_3 nanoflakes		0.05–3.145 mM	422.5 μA/mM	22 μM	[30]
Vertical α-FeOOH		0–6.5 mM	194.0 μA/mM	18 μM	[31]
γ -Fe_2O_3/Fe_3O_4		0.0002–8 mM	N/A	0.05 μM	[32]
Fe_3O_4/3D G NCs	N/A	274.15mA/mM	0.078 μM	[33]	
PCB chip in $FeCl_2$ solution	0-200 μM	22 μA/mM	7.14 μM	This work	

4. CONCLUSION

Custom-made PCB chips could be used as electrochemical cell electrodes in order to create cheap mass-produced portative electrochemical sensors for rapid and easy detection of excess concentrations of H_2O_2 without involving complex laboratory equipment and specially trained operator. $FeCl_2$ buffer solution is a viable option for hydrogen peroxide detection by both electrochemical and optical analysis methods. The suggested buffer could be used to detect hydrogen peroxide concentrations as low as 5 μM by both transmissivity spectrum analysis and CV. In order to achieve maximal sensitivity at low hydrogen peroxide concentrations, $FeCl_2$ should be present in a concentration at least 30-fold higher than the target hydrogen peroxide concentration.

ACKNOWLEDGEMENTS

The research has been supported by Daugavpils University Project No. 14-95/2021/11 “Development of the Electrochemical Sensor for Oxidant Concentrations, Bigger than Cell Structure Physiological Norm, Measurement”.

REFERENCES

1. Grisham, M. B. (2013). Methods to Detect Hydrogen Peroxide in Living Cells: Possibilities and Pitfalls. *Comparative Biochemistry and Physiology Part A: Molecular & Integrative Physiology*, *165* (4), 429–438. doi:10.1016/j.cbpa.2013.02.003
2. Halliwell, B., Clement, M.V., & Long, L. H. (2000). Hydrogen Peroxide in the Human Body. *FEBS Letters, 486* (1), 10–13. doi:10.1016/S0014-5793(00)02197-9
3. Dev, S., Kumari S., Singh, N., Bal, S. K., Seth P., & Mukhopadhyay, C. K. (2015). Role of Extracellular Hydrogen Peroxide in Regulation of Iron Homeostasis Genes in Neuronal Cells: Implication in Iron Accumulation. *Free Radical Biology and Medicine, 86*, 78–89. doi:10.1016/j.freeradbiomed.2015.05.025
4. Driessens, N., Versteyhe, S., Ghaddhab, C., Burniat, A., Deken, X. D., Sande, J. V., … & Corvilain, B. (2009). Hydrogen Peroxide Induces DNA Single- and Double-Strand Breaks in Thyroid Cells and is Therefore a Potential Mutagen for this Organ. *Endocrine-Related Cancer,* 16, 845–856. doi:10.1677/ERC-09-0020

5. Zunino, A., Degan, P., Vigo, T., & Abbondandolo, A. (2001). Hydrogen Peroxide: Effects on DNA, Chromosomes, Cell Cycle and Apoptosis Induction in Fanconi's Anemia Cell Lines. *Mutagenesis, 16* (3), 283–288. doi:10.1093/mutage/16.3.283
6. Amri, F., Ghouili, I., Amri, M., Carrier, A., & Masmoudi-Kouki, O. (2017). Neuroglobin Protects Astroglial Cells from Hydrogen Peroxide-Induced Oxidative Stress and Apoptotic Cell Death. *Journal of Neurochemistry,140* (1), 151–169. doi:10.1111/jnc.13876
7. Lisanti, M., Martinez-Outschoorn, U., Lin, Z., Pavlides, S., Whitaker-Menezes, D., Pestell, R., … & Sotgia, F. (2011). Hydrogen Peroxide Fuels Aging, Inflammation, Cancer Metabolism and Metastasis: The Seed and Soil also Needs "Fertilizer". *Cell Cycle, 10* (15), 2440–2449. doi:10.4161/cc.10.15.16870
8. Guesmi, F., Bellamine, H., & Landoulsi, A. (2018). Hydrogen Peroxide-Induced Oxidative Stress, Acetylcholinesterase Inhibition, and Mediated Brain Injury Attenuated by Thymus Algeriensis. *Appl Physiol Nutr Metab, 43* (12), 1275–1281. doi: 10.1139/apnm-2018-0107
9. Gaikwad, R., Thangaraj, P. R., & Sen, A. K. (2021). Direct and Rapid Measurement of Hydrogen Peroxide in Human Blood Using a Microfluidic Device. *Scientifc Reports, 11*, 2960. doi: 10.1038/s41598-021-82623-4
10. Rhee, S.G., Chang, T.-S., Jeong, W., & Kang, D. (2010). Methods for Detection and Measurement of Hydrogen Peroxide Inside and Outside of Cells. *Molecules and Cells, 29* (6), 539–49. doi: 10.1007/s10059-010-0082-3.
11. Zheng, X., Lian, Q., Zhou, L., Jiang, Y., & Gao, J. (2021). Peroxidase Mimicking of Binary Polyacrylonitrile-CuO Nanoflowers and the Application in Colorimetric Detection of H_2O_2 and Ascorbic Acid. *ACS Sustainable Chem. Eng, 9*, 7030−7043. doi: 10.1021/acssuschemeng.1c00723
12. González-Sánchez, M. I., González-Macia, L., Pérez-Prior, M. T., Valero, E., Hancock, J., & Killard, A.J. (2013). Electrochemical Detection of Extracellular Hydrogen Peroxide in Arabidopsis Thaliana: A Real-Time Marker of Oxidative Stress. *Plant, Cell & Environment, 36* (4), 869–78. doi: 10.1111/pce.12023.
13. Rahman, M. M., Adeosun, W. A., & Asiri, A. M. (2020). Fabrication of Selective and Sensitive Chemical Sensor Development Based on Flower-Flake La_2ZnO_4 Nanocomposite for Effective Non-Enzymatic Sensing of Hydrogen Peroxide by Electrochemical Method. *Microchemical Journal, 159*, 105536. doi: 10.1016/j.microc.2020.105536.
14. Yin, H., Shi, Y., Dong, Y., & Chu, X. (2021). Synthesis of Spinel-Type $CuGa_2O_4$ Nanoparticles as a Sensitive Non-Enzymatic Electrochemical Sensor for Hydrogen Peroxide and Glucose Detection. *Journal of Electroanalytical Chemistry, 885*, 115100. doi: 10.1016/j.jelechem.2021.115100.
15. Sinha, G. N., Subramanyam, P., Sivaramakrishna, V., & Subrahmanyam, C. (2021). Electrodeposited Copper Bismuth Oxide as a Low-Cost, Non-Enzymatic Electrochemical Sensor for Sensitive Detection of Uric Acid and Hydrogen Peroxide. *Inorganic Chemistry Communications, 129*, 108627. doi: 10.1016/j.inoche.2021.108627
16. Atacan, K., & Özacar, M. (2021). Construction of a Non-Enzymatic Electrochemical Sensor Based on CuO/g-C_3N_4 Composite for Selective Detection of Hydrogen Peroxide. *Materials Chemistry and Physics, 266*, 124527. doi: 10.1016/j.matchemphys.2021.124527
17. Kamyabi, M.A., & Hajari, N. (2017). Low Potential and Non-Enzymatic Hydrogen Peroxide Sensor Based on Copper Oxide Nanoparticle on Activated Pencil Graphite Electrode. *J. Braz. Chem. Soc., 28* (5), 808–818. doi: 10.21577/0103-5053.20160232
18. Huang, J., Zhu, Y., Zhong, H., Yang, X., & Li, C. (2014). Dispersed CuO nanoparticles on a silicon nanowire for improved performance of nonenzymatic H_2O_2 detection. *ACS Applied Materials Interfaces, 6* (10), 7055–7062. doi: 10.1021/am501799w

19. Kumar, J. S., Ghosh, S., Murmu, N. C., Mandal, N. & Kuila, T. (2019). Electrochemical Detection of H_2O_2 Using Copper Oxide-Reduced Graphene Oxide Heterostructure. *Journal of Nanoscience and Nanotechnology,* 19, 5295–5302. doi: 10.1166/jnn.2019.16834.

20. Gerbreders, V., Krasovska, M., Mihailova, I., Ogurcovs, A., Sledevskis, E., Gerbreders, A., … & Plaksenkova, I. (2019). ZnO Nanostructure-Based Electrochemical Biosensor for Trichinella DNA Detection. *Sensing and Bio-Sensing Research, 23*, 100276. doi: 10.1016/j.sbsr.2019.100276

21. Kolthoff, I. M., & Medalia, A. I. (1949). The Reaction between Ferrous Iron and Peroxides. I. Reaction with Hydrogen Peroxide in the Absence of Oxygen. *Journal of the American Chemical Society, 71* (11), 3777–3783. doi: 10.1021/ja01179a057

22. Gerbreders, V., Krasovska, M., Sledevskis, E., Gerbreders, A., Mihailova, I., & Ogurcovs, A. (2020). Hydrothermal Synthesis of ZnO Nanostructures with Controllable Morphology Change. *CrystEngComm, 22*, 1346–1358. doi:10.1039/C9CE01556F

23. Liu, M., Liu, R., & Chen, W. (2013). Graphene Wrapped Cu_2O nanocubes: Non-Enzymatic Electrochemical Sensors for the Detection of Glucose and Hydrogen Peroxide with Enhanced Stability. *Biosens. Bioelectron, 45*, 206–212. doi: 10.1016/j.bios.2013.02.010

24. Gao, P., & Liu, D. (2015). Facile Synthesis of Copper Oxide Nanostructures and their Applicationin Non-Enzymatic Hydrogen Peroxide Sensing. *Sensors and Actuators B, 208*, 346–354. doi: 10.1016/j.snb.2014.11.051

25. Gao, P., & Liu, D. (2015). Petal-Like CuO Nanostructures Prepared by a Simple Wet Chemical Method, and their Application to Non-Enzymatic Amperometric Determination of Hydrogen Peroxide. *Microchim Acta, 182* (7–8), 1231–1239. doi: 10.1007/s00604-015-1476-x

26. Zhang, W., Fan, G., Yi, H., Jia, G., Li, Z., Yuan, C., … & Fu, D. (2018). Interfacial Engineering of Hierarchical Transition Metal Oxide Heterostructures for Highly Sensitive Sensing of Hydrogen Peroxide. *Small, 14* (19), 1703713. doi: 10.1002/smll.201703713

27. Mizers, V., Gerbreders, V., Sledevskis, E., Kokina, I., Tamanis, E., Krasovska, M., … & Bulanovs, A. (2020). Electrochemical Detection of Small Volumes of Glyphosate with Mass-Produced Non-Modified Gold Chips. *Latvian Journal of Physics and Technical Sciences, 57* (3), 32–39. doi: 10.2478/lpts-2020-0013

28. Dutta, A., Maji, S., Srivastava, D., Mondal, A., Biswas, P., Paul, P., & Adhikary, B. (2021). Peroxidase-Like Activity and Amperometric Sensing of Hydrogen Peroxide by Fe_2O_3 and Prussian Blue-Modified Fe_2O_3 Nanoparticles. *J. Mol. Cat. A: Chem.*, *360*, 71– 77. doi: 10.1016/j.molcata.2012.04.011

29. Majumder, S., Saha, B., Dey, S., Mondal, R., & Banerjee, S. (2016). A Highly Sensitive Non-Enzymatic Hydrogen Peroxide and Hydrazine Electrochemical Sensor Based on 3D Micro-Snowflake Architectures of α-Fe_2O_3. *RSC Adv*. 6, 59907–59918. doi: 10.1039/C6RA10470C

30. Cai, J., Ding, S., Chen, G., Sun, Y., & Xie, Q. (2018). In Situ Electrodeposition of Mesoporous Aligned α-Fe_2O_3 Nanoflakes for Highly Sensitive Nonenzymatic H_2O_2 Sensor. *Applied Surface Science, 456*, 302–306. doi: 10.1016/j.apsusc.2018.06.108

31. Du, S., Ren, Z., Wu, J., Xi, W., & Fu, H. (2016). Vertical α-FeOOH Nanowires Grown on the Carbon Fiber Paper as a Free-Standing Electrode for Sensitive H_2O_2 Detection. *Nano Res*., *9*, 2260–2269. doi: 10.1007/s12274-016-1113-y

32. Molodtsova, T., Gorshenkov, M., Saliev, A., Vanyushin, V., Goncharov, I., & Smirnova, N. (2021). One-Step Synthesis of γ-Fe_2O_3/Fe_3O_4 Nanocomposite for Sensitive Electrochemical Detection of Hydrogen Peroxide. *Electrochimica Acta, 370*, 137723. doi: 10.1016/j.electacta.2021.137723

33. Zhao, Y., Huo, D., Bao, J., Yang, M., Chen, M., Hou, J., … & Hou, C. (2017). Biosensor Based on 3D Graphene-Supported Fe_3O_4 Quantum Dots as Biomimetic Enzyme for In Situ Detection of H_2O_2 Released from Living Cells. *Sens. Actuators B Chem, 244*, 1037–1044. doi:10.1016/j.snb.2017.01.029